ABSTRACT

Title of dissertation: TOPOLOGICAL RARE EARTH HALF-HEUSLER HoPtBi

Connor Roncaioli
Doctor of Philosophy, 2019

Dissertation directed by: Professor Johnpierre Paglione
Department of Physics

Magnetic HoPtBi is created and characterized as a new half-Heusler Weyl-candidate. By analogy with the well-studied GdPtBi system we undertake measurements intended to understand the normal state of this material, before extending our study to search for characteristics of Weyl behavior. We find a material with semiconducting properties as well as a low temperature antiferromagnetic transition below 1.25K and a Curie-Weiss paramagnetic system above. Analysis of the magnetoresistance in HoPtBi finds multiple Weyl-like characteristics, including potential chiral anomaly and anomalous Hall angle components. Finally we found significant anisotropic magnetoresistance in HoPtBi dependent on field alignment relative to the crystalline axes of the material, which is unexpected for a paramagnetic compound. We will show that these behaviors indicate a material with a Fermi surface readily tuned by application of magnetic field.

TOPOLOGICAL BEHAVIOR IN RARE EARTH HALF-HEUSLER HoPtBi

by

Connor Roncaioli

Dissertation submitted to the Faculty of the Graduate School of the
University of Maryland, College Park in partial fulfillment
of the requirements for the degree of
Doctor of Philosophy
2019

Advisory Committee:
Professor Johnpierre Paglione, Chair/Advisor
Professor Richard Greene
Professor Christopher Lobb
Adjunct Associate Professor Nicholas Butch
Professor Ichiro Takeuchi, Dean's Representative

Foreword

The following works have been the result of my graduate studies:

- C. Roncaioli, T. Drye, S.R. Saha, J. Paglione, "Influence of growth flux solvent on anneal-tuning of ground states in CaFe2As2". *Phys Rev Mater.*, 2, 044801 (2018).

- Z. Xing, T. Huffman, P. Xu, A. AHollingshad, D. Brooker, N. Penthorn, M. Qazilbash, S. Saha, T. Drye, C. Roncaioli, J. Paglione, "Role of electron-electron interactions in the charge dynamics of rare-earth doped CaFe2As2". *Phys Rev B.* 94, 064514 (2016).

- X. Wang, C. Roncaioli, C. Eckberg, H. Kim, J. Yong, Y. Nakajima, S. Saha, P. Zavalij, J. Paglione, "Tunable electonic anisotropy in single-crystal A2Cr3As3 (A=K,Rb) quasi-one-dimensional superconductors". *Phys Rev B.* 92. 020508 (2015).

- D.J. Campbell, Z.E. Brubaker, C. Roncaioli, P. Saraf, Y. Xiao, P. Chow, C. Kenney-Benson, D. Popov, R.J. Zieve, J.R. Jeffries, J. Paglione, "High Pressure Kondo Insulator-Semimetal Transition in Ce3Bi4Pt3". *arXiv* (2019).

Dedication

To Jason my eternal sunshine, and Pike my loyal shadow. I love you both.

Acknowledgments

I am eternally grateful for all the people who have made this research possible and who helped me develop into the researcher I am today.

First and foremost I'd like to thank my advisor, Professor Johnpierre Paglione for inviting me into his team and allowing me to make fascinating new discoveries under his tutelage. He has provided insightful advice and invaluable support in a long and sometimes difficult journey. The opportunities and skills he has provided shape an irreplaceable part of who I am today.

I would like to thank all of the research scientists and post-doctoral researchers who have helped teach me countless valuable lessons. Special thanks to Yun Suk Eo, Hyunsoo Kim, and Limin Wang for the numerous theoretical insights into the systems discussed within this dissertation and to Shanta Saha and Josh Higgins for the unflagging help they provided with the MPMS and PPMS systems. I also wish to reserve particular thanks for Halyna Hodovanets who has committed far too many hours to helping me practice careful and methodical research. Her sharp mind and meticulous attention to detail elevate the work of everyone around her.

I would like to thank my fellow and former graduate students Chris Eckberg, Daniel Campbell, I-Lin Liu, Prathum Saraf, John Collini, Wen-Chen Lin, Tyler Drye, Paul Syers, and others for the knowledge and camaraderie we shared. Many late nights were made a little more enjoyable by a friendly discussion.

Thank you to the Air Force Office of Scientific Research and the Gordan and Betty Moore foundation for the funding that allowed this project to exist, and to

your commitment to the sciences at large.

To my family I owe an incomprehensible debt. To my mother and father, Karen and Craig, who have cultivated in me a thriving curiosity and a measured sense of responsibility, and to my brother and sister, Casey and Kyle with whom I shared an endless sibling love and rivalry in equal measure.

I want to thank my countless friends who have supported me and provided me many a safe place to let my burdens down. Without you I wouldn't have the energy to tackle the tasks and duties in front of me.

I want to thank Pike, who is a font of unconditional love, for keeping me grounded in happiness. Coming home to you wagging your tail is the unfailing highlight of my each and every day.

Most of all though I want to thank my adoring and unflagging partner in everything, Jason Hustedt. You are the light that casts my shadow, my number two in every crime, my soul. I do not exist without you, and I'd have it no other way.

Thank you all from the bottom of my heart!

Table of Contents

List of Figures

List of Abbreviations

AFM	Antiferromagnetic
AHA	Anomalous Hall Angle
AHE	Anomalous Hall Effect
AMR	Anisotropic Magnetoresistance
ARPES	Angle-Resolved Photo-Emission Spectroscopy
BZ	Brillouin Zone
CA	Chiral Anomaly
CM	Condensed Matter
CMR	Colossal Magnetoresistance
CW	Curie-Weiss Paramagnetism
DFT	Density Functional Theory
DHvA	De Haas-van Alphen
DoS	Density of States
DSM	Dirac Semimetal
EDS/EDX	Energy Dispersive X-ray Spectroscopy
GMR	Giant Magnetoresistance
HA	Hall Angle
FFT	Fast Fourier Transform
FM	Ferromagnetic
FS	Fermi Surface
MPMS	Magnetic Property Measurement Systems
MR	Magnetoresistance
MSM	Magnetic Semimetal
NCNR	NIST Center for Neutron Research
NHMFL	National High Magnetic Field Lab
NIST	National Institute of Standards and Technology
NMR	Negative Magnetoresistance
PHE	Planar Hall Effect
PM	Paramagnetic

PPMS	Physical Properties Measurement System
QO	Quantum Oscillations
RE	Rare Earth
RPtBi	(Rare earth) Platinum Bismuthide compound
RPdBi	(Rare earth) Palladium Bismuthide compound
SC	Single Crystal
SdH	Shubnikov-de Haas
SOC	Spin Orbit Coupling
SS	Solid State
TI	Topological Insulator
TMR	Tunneling Magnetoresistance
VSM	Vibrating Sample Magnetometer
WSM	Weyl Semimetal
XRD	X-ray Diffraction

Chapter 1: Background

The condensed matter (CM) field of physics is often concerned with the investigation of novel Hamiltonians. In many ways the creation of unique energetic landscapes and the ability to manipulate them in a low-energy, accessible scale is what connects CM to our high-energy and particle physics contemporaries and sets the field apart in its capacities. Bose-Einstein condensates, superfluids, Majorana Fermions, massless Dirac particles and countless other theoretical systems have been or are predicted to be realizable in materials that we can engineer in small, user-accessible labs. Adding to this ever-expanding repertoire many CM physicists have taken a recent interest in Weyl semimetals, materials that reflect the generalization of the Dirac Hamiltonian proposed by Hermann Weyl in 1929. [1]

The prediction for the Weyl Hamiltonian and the search for corresponding Weyl Fermions is closely tied to the more widely used Dirac equations. The Dirac equations are familiar to any physicist as the basis for relativistic quantum mechanics. More specifically the Dirac equations integrates the necessary spin degree of freedom which makes our understanding of Fermi-Dirac statistics consistent with the 2-electron orbital occupancy. Dirac semimetals, in particular Graphne, have been a fertile ground for the study of relativistic quasiparticles and their associated

physics. [2] Weyl semimetals are a particular class of materials in which the Fermi surface has distinct regions of well-defined spin character that host massless Dirac quasiparticles. The discovery of Weyl semimetal compounds has lead to an entirely new subfield of condensed matter physics focused on the novel behavior, and proper classification, of these compounds.

1.1 Topological Materials

For the conventional solid state physicist it might not be immediately clear what makes a material topological. Topology is generally concerned with global properties, ie properties of that can only be described by looking at global structure and not just evaluated at a point. The classic example of a topological invariant is the comparison between a toroid and a sphere. A toroid could be continuously deformed into many shapes, such as a coffee cup or donut, without ever disturbing the continuity of the surface. However it is only by 'cutting' or 'pinching' that a toroid could be transformed into a sphere. The Chern-Gauss-Bonnet theorem formalizes this understanding of closed physical surfaces. [3]

The language of topology may seem an odd fit for a field which has historically a large connection to nanophysics. For instance the p-n junction, arguably the single most important technological development of the 20th century, depends explicitly on connecting two regions of different microscopic character within a singular device. [4] Nonetheless careful inspection finds that the fundamental tools of condensed matter physics are well adapted to topological analysis.

1.1.1 Chern Number as a Topological Invariant

Bloch's theorem is one of the fundamental keystones of solid-state physics. The single particle Bloch wavefunction that inhabits a mathematically ideal, infinitely periodic lattice makes an exceptionally good approximation for the real study of particles in near-infinite lattices of $N \approx 10^{26}$ atoms. A Bloch wave function $|u_n(k)>$ in momentum-space is a function of crystalline momentum k and is uniquely labeled by the band from which it originates n. $|u_n(k)>$ defined on the first Brillouin zone completely defines the available states for the system, since all higher Brillouin zones are images of the first Brillouin zone related by a reciprocal lattice vector.

In a 3D crystalline system we can also calculate the Berry connection

$$A(k) =< u_n(k)|i\delta_k u_n(k) > \tag{1.1}$$

which is related to the Berry curvature

$$\Omega(k) = \nabla A. \tag{1.2}$$

Berry connection and Berry curvature represent the gauge evolution through available quantum states, and is a useful concept not just for crystalline systems satisfying Bloch's theorem's constraints, but any adiabatic path through a quantum mechanical system. [3] Integrating the Berry curvature over a closed surface gives a discrete quantity known as the Chern number [3]

$$C_i = \frac{1}{2\pi} \int_S \Omega dS. \tag{1.3}$$

The Chern number is quantized, and in a real crystalline system we have the useful property that the Chern number is necessarily zero when calculated over the full first Brillouin Zone. [3] (figure 1.1) Due to the lattice symmetries of the system, sweeping the Chern number integral over the full 3D Brillouin zone means that the Chern number must sum to zero. [5] [6] [7]

Although the Chern number for the entire Brillouin zone is necessarily zero, it is possible to divide up the BZ into sub-manifolds such that the Chern number of the sub-manifolds are non-zero. By necessity then each region of the Brillouin zone with non-zero Chern number C_i must have a complementary region with non-zero Chern number $C_j = -C_i$ (figure 1.1)

Thus pockets of non-zero Chern number always occur in pairs of opposite character. Furthermore, minor perturbations to the system which would adjust the band structure cannot alter the Chern number of a region except by pairwise annihilation of two pockets of opposite Chern number. This latter property is commonly referred to as *topological protection* and has profound implications when it comes to transport. In particular, if a material has topologically non-trivial bandstructure then the pairwise annihilation is mandated on the surface in order to continuously transition to the topologically trivial vacuum, which leads to the creation of topologically protected *surface states*. [7] [5]

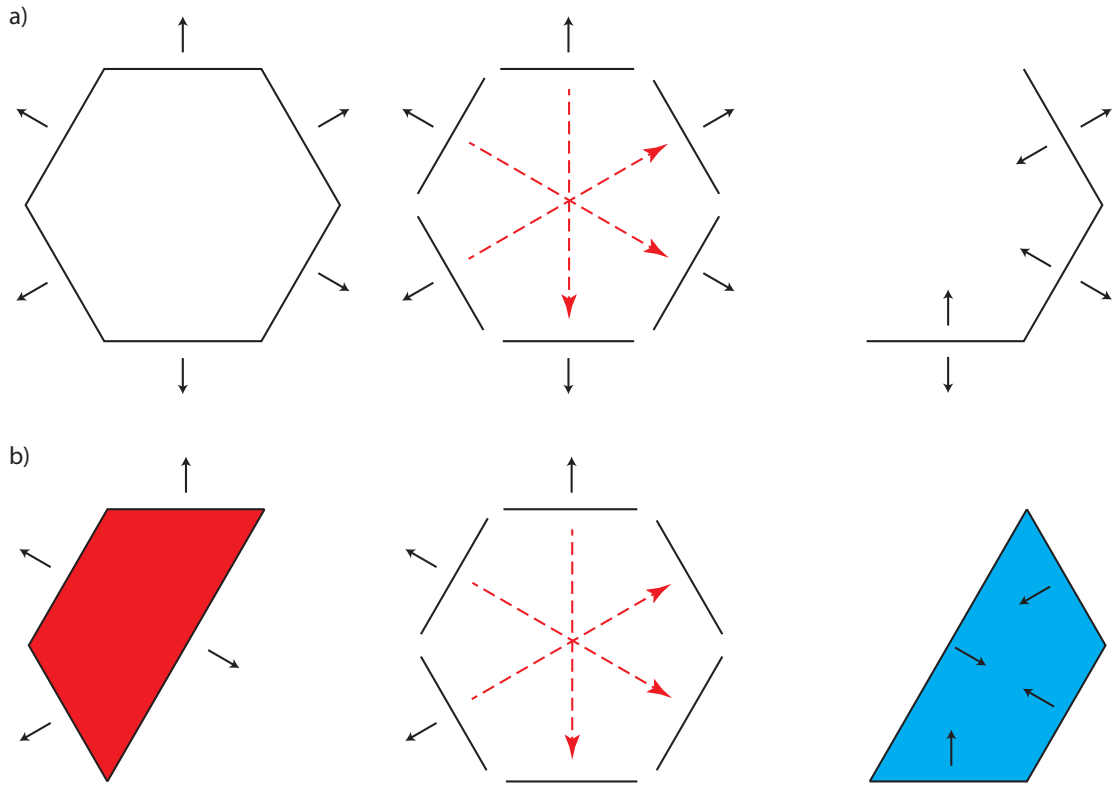

Figure 1.1: 2D cross-section of the Chern number being evaluated within the first Brillouin zone of a hexagonal system. a) The integral is expanded over the whole first Brilloin zone, using Stokes' theorem combined with the reciprocal lattice vectors (dashed, red) the integral volume can be collapsed to a zero-volume, which necessitates a zero Chern number. b) The integral over a sub-manifold of the first BZ cannot be fully collapsed. A non-zero Chern number may be evaluated in this regime (stylized red) however the complementary region of the BZ must be of equal and opposite value (stylized blue). This matches the expected condition imposed by the full BZ integral and can readily be extended to 3D. [3]

1.1.2 Dirac and Weyl Semimetals

While the properties of Chern numbers are useful, it is not clear from the theoretical formulation what types of materials might host non-trivial topological states. The study of topological materials has exploded in the last decade. Topological insulators [8] [9], Dirac semimetals [2], Weyl semimetals [10] [11], and magnetic half-Heuslers [12] have all been studied as part of the greater research of topological materials.

Dirac and Weyl semimetals, as well as the magnetic half-Heuslers, are of particular interest because in addition to satisfying some of the requirements to have regions of non-zero Chern number, they also have non-zero density of states near the Fermi surface. As a result there are accessible conduction states in the bulk of the material with unique properties, subject to topological protection.

The Dirac equations in covariant form are written

$$i\hbar\gamma^{\mu}\delta_{\mu}\phi - mc\phi = 0, \tag{1.4}$$

where γ^{μ} are matrices that form the basis of a Clifford algebra. This formulation was designed to provide a metric which accurately represented space-time while evading some unphysical degeneracies while predicting intrinsic spin. [7] Weyl semimetals represent a specific solution of the Dirac equation in the relativistic regime ($m = 0$). The massless spin-dependent Weyl Hamiltonian is

$$\mathcal{H}_W = \kappa c\vec{k} \cdot \vec{\sigma} \tag{1.5}$$

with $\kappa = \pm 1$ reflecting the chirality of the Hamiltonian, $\vec{\sigma}$ a vector composed of the Pauli matrices, and $\vec{k}$ the momentum of the quasiparticle. An ideal Weyl semimetal would have a massless linear dispersion and no band gap, however some materials such as the HoPtBi investigated in this dissertation may have a quadratic dispersion near the Weyl crossing. [12] [13]

A key characteristic of the Weyl Hamiltonian is that its solutions are momentum locked, i.e. knowing the momentum, $\vec{p}$ at a given energy also fixes the spin of the quasiparticle. This is notable for many reasons, not the least of which is that spin-locked Hamiltonians are robust against non-magnetic backscattering. Any scattering effect which reverses the momentum of the particle must also reverse its spin (ie, interact magnetically) or else there will be no available states to scatter into. This means that the conduction channels associated with the Weyl point should be robust against conventional sources of backscattering, such as disorder. [14]

Furthermore, κ can be mapped to the Chern number quantizing the sum of the Berry curvature around the Weyl point, as discussed in section 1.1.1. For type I Weyl points, in which the massless Dirac cone is relativistic (figure 1.2) the Chern number is mapped to the integral of the Berry curvature at fixed energy around the Weyl point. Due to the limitations imposed by periodic materials, the Berry curvature must disappear when integrated over the whole first Brillouin zone, therefore Weyl points must be matched throughout the first Brillouin zone by Weyl

points of opposite parity such that the summation of all Weyl points is Chern number $\Sigma C_i = 0$.

It is worth noting that (equation 1.5) only represents the Hamiltonian in the vicinity of a single Weyl point. More in-depth calculations of Weyl systems must necessarily take into account the net zero Chern number considerations enforced by the Brillouin zone. In particular, since Weyl points are always matched with a point of equal but opposite Chern number, there must also be a protected Lifshitz transition somewhere in the vicinity of the Weyl crossing which corresponds to the merger, and resulting annihilation, of the Weyl pocket pair. [15] [16] [17] Since Weyl points exist due to band inversion it is a reasonable concern to expect the Lifshitz transition to be not far energetically from the Weyl point.

In addition to the necessary condition that all Weyl points must be matched by an equal Weyl point of opposite character, symmetry considerations can inform us about the relative location of Fermi surface features in a given material. [18] Because Weyl semimetals are by definition spin-split materials, they must break either time reversal symmetry T, or inversion symmetry $\mathcal{P}$. In the case of systems that break T but preserve $\mathcal{P}$ the Brillouin zone must be symmetric when $\vec{k} \Rightarrow -\vec{k}$, therefore the Chern number of the Weyl points related by this transformation must be equivalent. As a result for these systems the total number of Weyl points must be $4N$ to respect not only the Brillouin sum rule, but also the symmetry relations between Weyl points. In systems that break $\mathcal{P}$ but not T, Weyl points on opposite sides of the Brillouin zone are of opposite character, meaning that only $2N$ Weyl points must exist as Weyl points symmetrically located in the BZ already obey the

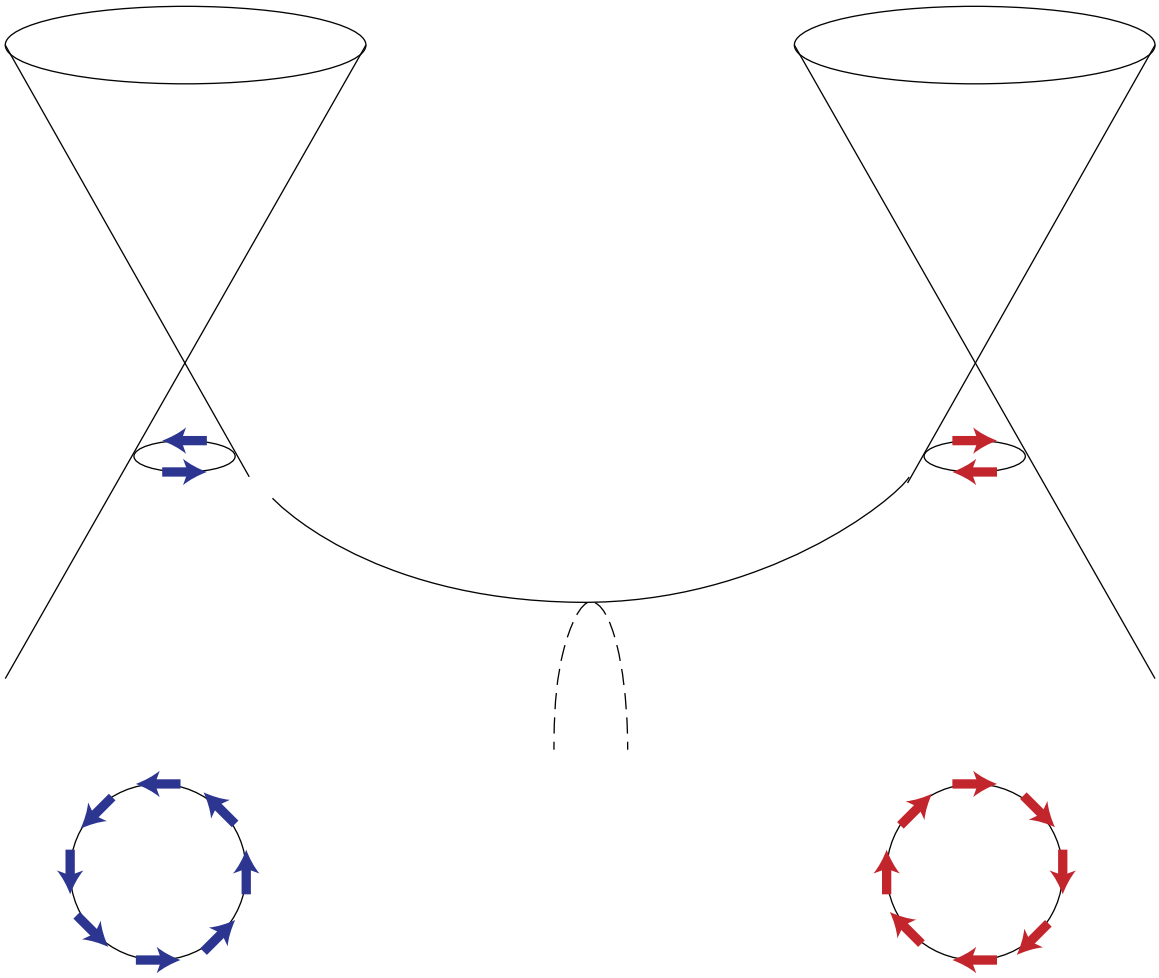

Figure 1.2: Schematic overview of the simplest Weyl prototype. Near the crossing point the dispersion is relativistic, with spin locked to momentum along the iso-energetic surface (blue arrows). A second Weyl point of opposite character is necessitated by the topological arguments covered in section 1.1.1 (red arrows). Away from the crossing point the bands must become quadratic and merge, creating a Lifshitz transition (dashed line).

zero Chern sum condition.

By their non-zero Chern number Weyl semimetals are explicitly tied to the phenomenon of topology in CM systems. Like the simpler topological insulators, Weyl semimetals have a distinct protected surface state that bridges the topological bulk state and the trivial state outside of a Weyl material. Unlike topological insulators, Weyl semimetals have bulk conduction states near the Fermi surface. Band inversion creates distinctive changes to the band structure of these conducting states, twisting the curvature of the inverted bands to create a non-zero chern number evaluated at the FS. This leads to a bevy of distinctive behaviors in Weyl materials, in particular a number of magnetoconductivity effects that are strong, although not necessarily unique, indicators of Weyl behavior.

1.1.3 Chiral Anomaly

The most prominent transport effect on the bulk state of Weyl semimetals is the presence of the Chiral anomaly which represents a negative magnetoresistance contribution when applied magnetic field is co-aligned with the electric field in the material. [19] [5]

The result of this effect is the biasing of carriers in the Weyl point associated with electric field and away from the symmetry-paired Weyl point that is anti-aligned. As a result a 'spontaneous current' develops between these Weyl points, increasing conductivity in this configuration.

Measurements have been carried out for Chiral anomaly on a number of mate-

rials including TaAs [20] and HoPtBi's sister compound, GdPtBi [21] and others [22]. Unfortunately negative magnetoresistance in semimetals, and magnetic semimetals in particular is not incontrovertible evidence for a Weyl semimetal state. Semimetals with high carrier mobility under high magnetic fields are often subject to the extrinsic effect known as current jetting which can create a negative magnetoresistance signal in the longitudinal $\vec{E} \parallel \vec{B}$ configuration which overlaps with the chiral anomaly. [23] While current jetting is not a problem for the theoretical case of ideal lead placement and uniform current distribution within materials, it is practically speaking a significant extrinsic cause of negative magnetoresistance.

1.1.4 Anomalous Hall effect

The next significant indicator of potential Weyl-like behavior is the anomalous Hall effect. The conventional Hall effect is best understood by first considering the general conductivity tensor

$$J_i = \sigma_{ij} E_j \tag{1.6}$$

and its inverse

$$E_i = \rho_{ij} J_j \tag{1.7}$$

which can be decomposed into

$$\rho_{ij} = \sigma_{ij}^{-1} = \rho_{ij}^{symm} + \rho_{ij}^{asymm}. \tag{1.8}$$

The conductivity tensor σ is a rank two tensor with some well-established properties. Onsager's reciprocal relations, which generally apply to any flux of a system initially at equilibrium, dictates that $\sigma_{ij}(B) = \sigma_{ji}(-B)$. In zero field σ is diagonal. Furthermore any rank-two tensor can be broken down into symmetric and antisymmetric components. The classical Hall effect is an expression of the Lorentz force, given by

$$F_i = e\epsilon_{ijk}(v_j B_k) \tag{1.9}$$

where ϵ_{ijk} is the Levi-Cevita term. Scattering may interfere with the degree of Hall deflection, but does not by itself break any further symmetries. Therefore the conventional Hall effect is described by the antisymmetric off-diagonal elements of the conductivity tensor. [24]

The conventional Hall effect relates to the deflection of charged carriers by the classical Lorentz force. While the model was originally derived by the classical Drude model, it conveniently applies to quantum mechanical formulations based on quasiparticles in the electronic band structure of periodic lattices, though the derivation of this generalization is quite involved. [24] Anomalous Hall effect is a broad term describing off-diagonal conductivity tensor terms that do not correspond to the Lorentz force charge-deflection picture.

There are several potential causes for the anomalous Hall effect in materials at large, including extrinsic effects such as side jump or scew scattering terms from impurities in ferromagnetic systems and intrinsic effects from Berry curvature. [6] Since Weyl points introduce a quantized Berry curvature, an anomalous Hall effect is expected to intrinsically arise in these systems. [16]

Investigation of Berry curvature's effects on Hall transport are ongoing and depend on the details of the system. There have been arguments for a universal relationship between Weyl points and anomalous Hall effect in simple models however this depends on the idea that the Weyl points are well separated and the Fermi energy is close to the Weyl crossing. [16]

When analyzing the anomalous Hall effect, which contributes to the off diagonal component of the conductivity tensor σ_{xy}, it is helpful to consider the Hall angle

$$\Theta_H = arctan(\frac{\sigma_{xy}}{\sigma_{xx}}). \tag{1.10}$$

The Hall angle measures the net deflection of charge due to a magnetic field. In single carrier metals at high $\vec{B}$ the longitudinal conductivity diminishes while the transverse conductivity grows indefinitely, as a result the Hall Angle asymptotes to $\frac{\pi}{2}$. In the case of compensated semimetals, positive and negative carriers will be deflected in the same direction such that the net charge is not deflected laterally, and the Hall angle generally asymptotes to a near-zero value. In both of these classical materials the Hall angle varies continuously with applied magnetic field as σ_{xx} and

σ_{xy} continuously change. If the material undergoes a transition that affects the electronic transport properties, in particular a Lifshitz transition, we may expect to see a field-localized change in Hall Angle.

1.1.5 Planar Hall effect

Distinct from the anomalous Hall effect is the planar Hall effect. The Hall effect as covered in section 1.1.4 corresponds to the cross product of applied current and applied field, i.e. conductivity elements that are normal to both current and magnetic field contribution. By contrast the planar Hall effect occurs when the magnetic field is in the plane of conduction, rotated in the plane of the contacts (and by extension, current). Since the Lorentz force deflects carriers perpendicular to field direction it cannot account for the planar Hall effect. However, several groups have suggested that the intrinsic Berry curvature of Weyl semimetals can create a planar Hall effect. [25]

1.2 Select Weyl Candidates

1.2.1 TaAs

TaAs was one of the first materials to be reported as a Weyl semimetal. Initial reports focused on observation of the bulk and surface band structure by means of ARPES measurement. [11] [26] ARPES directly probes band structure density, however it is indiscriminate when it comes to the chiral nature of observed density of states (DoS), and it does not directly differentiate between bulk and surface states.

More complex spin-polarized ARPES measurements were used to determine that certain observed bands had spin character, further reinforcing the Weyl picture [27]

TaAs is a non-magnetic body-centered tetragonal I41md structure. Therefore, TaAs (and related compounds TaP, NbAs, NbP) is non-centrosymmetric, and DFT calculations confirm that this structure combined with the strong spin orbit coupling (SOC) effect is sufficient to create momentum-resolved Weyl points in this material. Therefore TaAs and its related compounds are predicted to be Weyl semimetals of the T-breaking type. [10] As discussed in section 1.1.2 Weyl semimetals that violate centrosymmetry but obey TRS must have Weyl points of identical character that are related by inversion in the Brillouin zone. By looking at band structure calculations in TaAs we can see an example of such symmetry-related Weyl points. In TaAs this resolves into 24 discrete Weyl nodes, each matching the condition that nodes of like-Chern number are related by inversion symmetry in the Brillouin zone.

In calculations done for TaAs band structure without spin orbit coupling the spin-degenerate state of the system has numerous Dirac points. i.e. the crossing is relativistic before spin orbit coupling is considered, and spin orbit coupling acts to split the spin-degenerate Dirac point into two, spin-textured Weyl points. TaAs then in a sense evolves directly from Dirac semi-metallic materials, which is distinct from the case of Weyl semimetals derived from the magnetic half-Heusler compounds.

1.2.2 GdPtBi

GdPtBi is a compound derived from the same series of RPtBi as HoPtBi studied in this dissertation. GdPtBi, however, has been richly studied in the past few years due to its predicted Weyl semimetal state and accessible paramagnetism. One of the crucial predictions for GdPtBi is that the WSM state is accessed only through application of field. GdPtBi (and associated RPtBi half-Heuslers, including HoPtBi) are of symmetry group $F\bar{4}3m$ and are non-centrosymmetric, however even with SOC included in DFT calculations GdPtBi is a quadratic semimetal in zero field down to low temperatures. This suggests that despite T being broken in GdPtBi the asymmetry is insufficient to create Weyl points.

Below $T_N = 9.2K$ GdPtBi enters an AFM state with ordering along the (111) direction. When moderate field is applied, the Gd moments are coerced out of AFM ordering and align paramagnetically, creating a reported interaction that spin-splits the Fermi surface, creating Weyl points. [12] [28] Therefore the primary broken symmetry that drives Weyl behavior in GdPtBi (and is suspected for related magnetic half-Heuslers) is $\mathcal{P}$ due to the internal field of the localized f-moments. This is supported by DFT calculations, which indicate Weyl points of opposite character related by inversion in the first BZ. [12] As a thoroughly studied high-J RPtBi compound, GdPtBi is the best magnetic analogue for HoPtBi and comparisons will be drawn between these compounds throughout subsequent chapters.

1.3 Half-Heusler Compounds

In order to expand the study of Weyl semimetals, we decided to focus on the family of half-Heusler compounds that GdPtBi is part of. RPtBi and RPdBi compounds have high potential for f-electron magnetism, and the heavy Bi element introduces significant SOC inverted bands near the Γ high-symmetry point. [30] [31]

Significant work was done on the RPdBi compounds, since Pt and Pd are very similar platinum-group metals this allowed me to extrapolate good candidates for RPtBi compounds to study. [13] Lanthanide contraction was determined by band structure calculations to be a significant tunable parameter for band inversion in RPdBi. (figure 1.3) Additionally Ho and Er were determined to be high-J candidate compounds with very low AFM ordering temperatures and large paramagnetic moments. (figure 1.4) Since we wished to investigate Weyl behavior in the paramagnetic state the RPtBi counterparts were identified as ideal candidates for topological investigation. Both compounds were grown, however in-depth investigation into HoPtBi occupied the focus of this research.

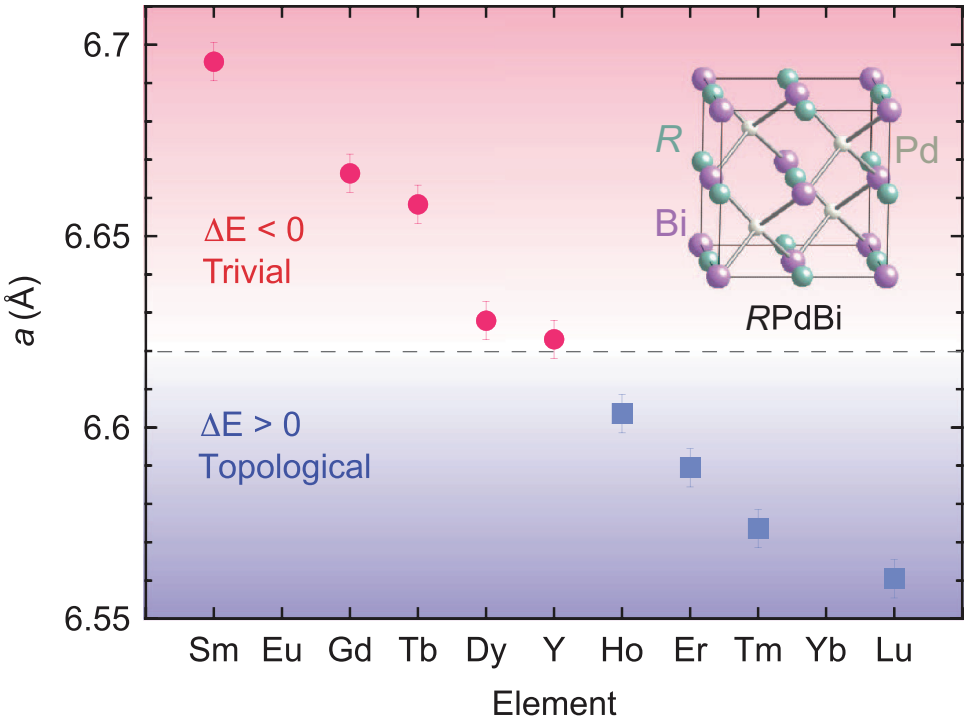

Figure 1.3: Lattice constant reduction in RPdBi as you traverse the 4f elements showing the lanthanide contraction effect. Band inversion strength $\Delta E = E_{\Gamma 8} - E_{\Gamma 6}$ decreases as lattice constant reduces, Ho and Er PdBi compounds are good candidates for band-inverted behavior. Figure is taken with permission from [13]

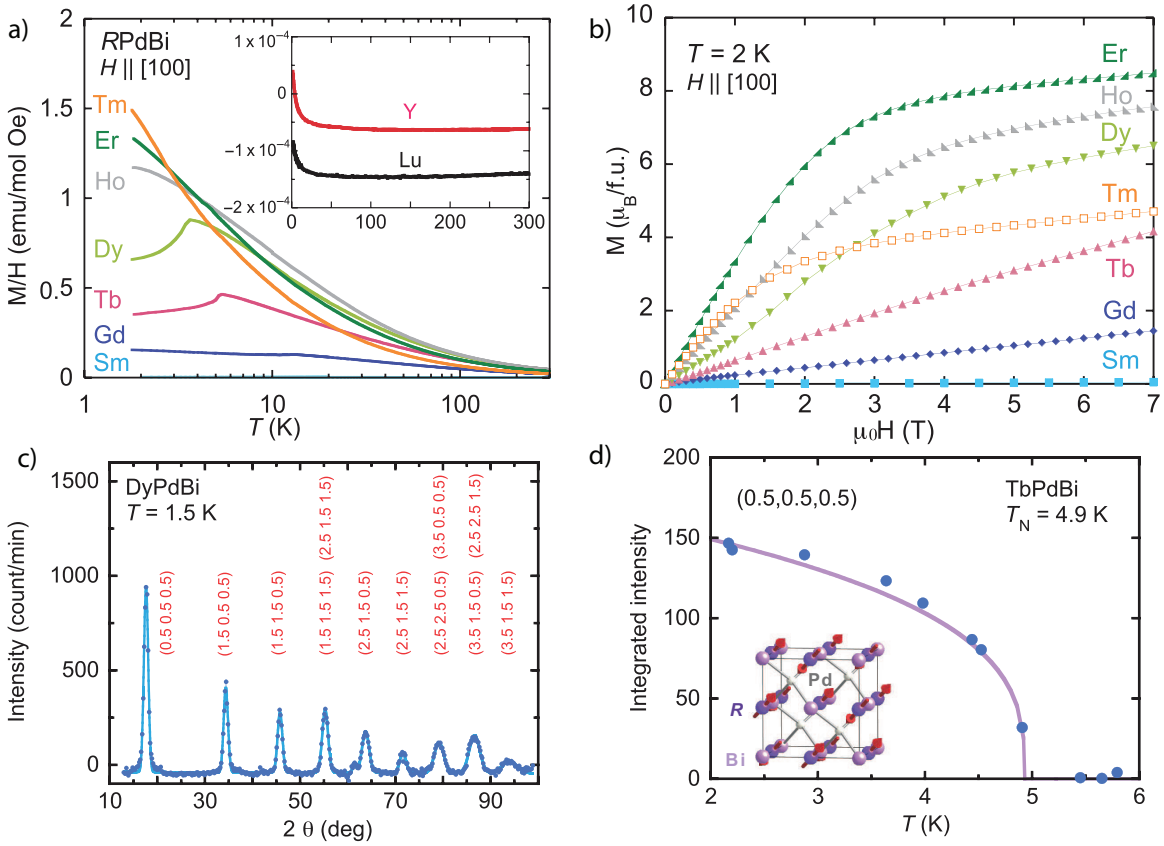

Figure 1.4: Various measurements of magnetism in the RPdBi series. a) Susceptibility as a function of temperature, showing AFM transitions for Dy, Tb, Gd, Sm, but no transitions for Ho or Er. b) Magnetization as a function of field showing Ho and Er with greatest magnetization. c) Neutron diffraction peaks in DyPdBi indicating $q = (0.5, 0.5, 0.5)$ magnetic ordering. d) Neutron diffraction in TdPdBi showing the low-field low-temperature AFM phase common to the RPdBi and RPtBi lanthanide family. Figures are taken with permission from [13]

Chapter 2: Experimental Methods

In this chapter we will cover the techniques required to go from elemental compounds provided by a manufacturer, to the measurement of the transport properties of a novel single crystal material. This section will begin by discussing the flux method by which we produce single crystal compounds. Then we will discuss how we characterize these materials to ensure that the material we have grown is the compound we desire. Then we will discuss the systems used to establish conditions of temperature and magnetic field vector relevant to these measurements. Finally we will explain the techniques involved in transport measurements and how these results can be used to determine interesting properties of the associated systems.

2.1 Single Crystal Growth

Before studying samples of a desired compound first it is necessary to produce crystals that are of proper stoichiometry, structure, and size. We produce samples by flux method, in which a molten metal flux is used as a solvent and the desired component materials are the solute. By heating the solvent metal well above its melting point the solute materials can completely dissolve in solution. The solution is then cooled until it is supersaturated, at which point a single nucleation site will

begin the process of crystal growth. By adjusting parameters such as flux solvent material, relative concentration of solutes and solvent, dwelling temperature, and rates of heating and cooling you can idealize the conditions to produce a given crystal, with the goal of producing single crystals of at least a millimeter in two dimensions, suitable for transport measurement.

In the case of Heusler compounds Bismuth, with a melting temperature of 271C, is our preferred flux. This method of using a solvent as a component in the goal precipitate is known as the 'self-flux' method, and is useful if the solvent metal has a low melting temperature and doesn't create super stable binary compounds with the solute components of the growth.

Growths of HoPtBi were grown using a ratio of 1:1:20 of Ho:Pt:Bi. This ratio produces truncated cubic crystals between 1-2mm per side which was sufficient for most transport measurements.

Component materials were assembled in a 2.5mL alumina crucible. Alumina is a stable oxide that melts at 2,000°C and is non-reactive with many metallic elements and as such makes a good choice for containing the growth solution (however, care should be taken for growths in which Aluminum is a potential dopant). A second crucible was filled with quartz wool, the quartz wool acts as a sieve when attempting to remove any precipitate from the remaining solution during the spin-out phase of the growth. This second crucible is placed inverted atop the first crucible and is known as the 'catch crucible'. This assembly is then placed inside a quartz tube, with additional quartz wool above and below to cushion the contact point between crucibles and tube. Then, the diameter of the region above the quartz tubes is

reduced using a Hydrogen-Oxygen torch in a process known as 'necking'. Note that during necking the inner diameter is not completely collapsed to allow inert gas exchange.

The necked assembly is then attached to a dry vacuum pump by means of a manifold of airtight tubes colloquially referred to as a pumping station. Reactive atmosphere is removed from the crucible, flushed with high-purity Argon, and then purged again. This cycle is repeated a total of three times, then the tube is filled with high-purity Argon to 1/5atm at room temperature (300K). The low pressure is chosen such that even at the maximum temperature allowed by the quartz tube (1500K) the pressure inside the tube would be no more than 1atm (assuming basic PV=nRT relation for ideal gasses, which Argon approximates rather well) so that the quartz tube assembly is never under pressure, which could cause an explosion risk. Finally the neck of the assembly is thinned and pinched using the H-O torch and the materials are ready to be put into a furnace for the growth procedure. An example of the final product of this procedure can be seen in figure 2.1.

The temperature schedule for the growth can be varied in numerous ways, and the exact schedule used can be crucial in determining the type and quality of product. HoPtBi has a fortuitously simple temperature profile: samples were heated from room temperature (20°C) to 1050°C at a rate of 50°C/hour then held at that temperature for 5 hours to ensure that the solute were fully dissolved. The aggregate was then cooled at 3°C/hour until 520°C. At this point the assembly is placed in a centrifuge and spun to mechanically separate the precipitated HoPtBi from the still molten Bismuth. The quartz sieve holds onto the precipitated material, and the

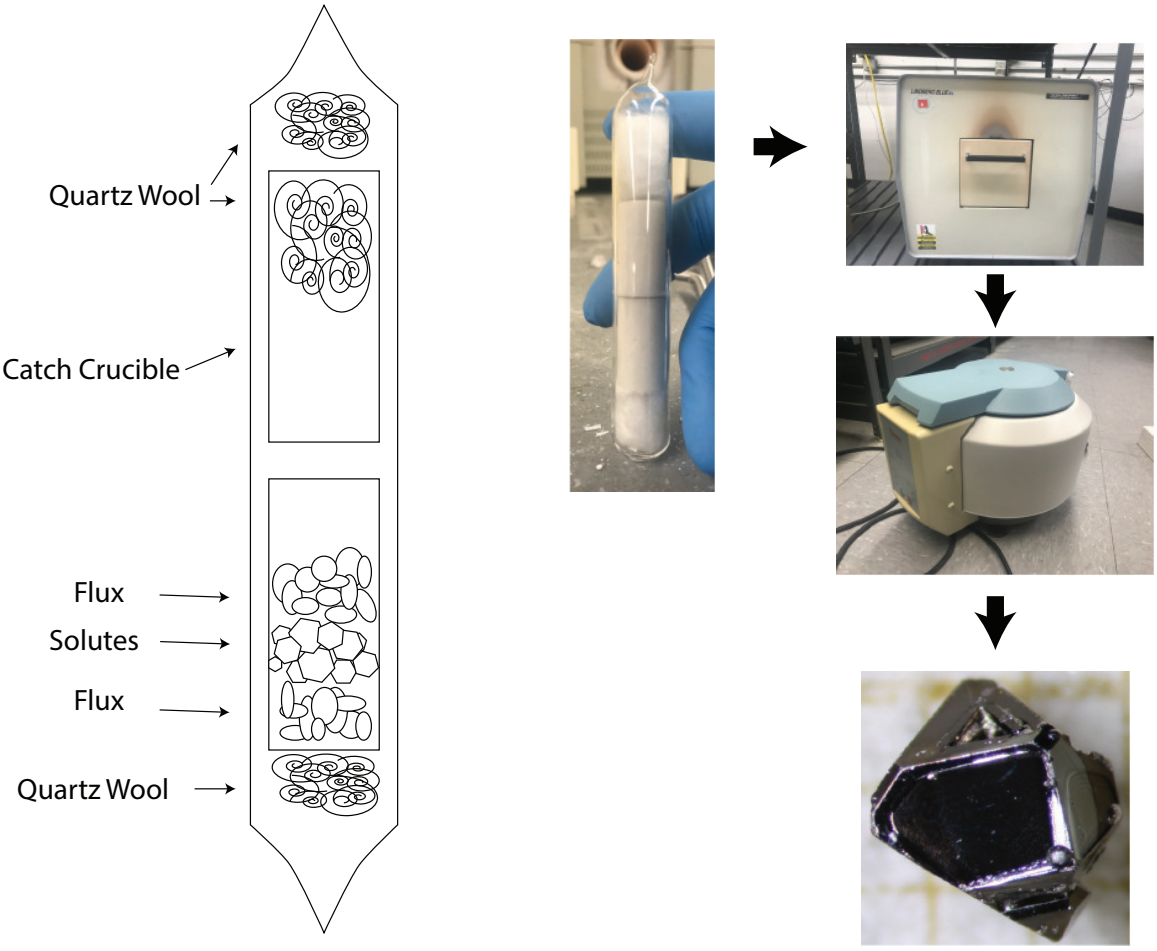

Figure 2.1: Diagram of sample crucibles and growth process. Components are assembled into a sealed quartz tube with inert Argon gas inside at $\frac{1}{5}atm$. The assembly is inserted into a furnace where it undergoes a growth sequence. After the sequence terminates the assembly is centrifuged to separate flux from growth product. An example crystal showing one well formed octagonal [100] and three triangular [111] faces. Small rectangular [110] faces are also visible.

remaining molten flux is passed through the sieve and caught at the bottom of the catch crucible, where it then solidifies. This process removes the greatest amount of flux, but subjects the crystal to a fair amount of physical strain when the material is still at high temperature. Therefore it is not recommended for fragile samples or materials close to a structural transition.

2.2 Sample Characterization

After decanting a new batch of crystals it becomes necessary to do two things: identify the crystal composition matches our intended product (or evaluate the structure and composition of a novel product) and shape the sample to an intended measurement geometry.

2.2.1 Determining Sample Orientation

Many of the experiments within will depend on the relative orientation not just of the Electric and Magnetic fields but of these fields with respect to the underlying crystalline symmetries. As such it is important to understand not just the structure of the material we are studying, but also how the microscopic structure relates to macroscopic properties of the crystal. The microscopic structures are crucial for understanding the physics involved, however it is the macroscopic sample which we manipulate and shape for measurement.

Understanding the full process by which atoms suspended in solution nucleate and form complete crystals is beyond the scope of this dissertation, however it is

still insightful to have a basic understanding of the energetics involved and how this affects the creation of crystalline product. For instance it is often the case that fully formed crystals will have an apparent geometry that matches the microscopic symmetries of the material. In the case of cubic $RPtBi$ the crystals will form in a shape similar to a cantellated cube, in which the edges and vertices are beveled with their own perpendicular surfaces, which has the Octahedral symmetry representation. This is useful for identifying the primary crystalline faces as the [100] and [111] planes are mapped directly to the prominent octagonal and triangular faces. The similarities are not complete however, as the crystal will often grow in a distorted or with certain sides misshapen by any of a myriad of causes, and in addition there are rectangular faces that correspond to the [110] direction (although these faces are quite small and easily discerned). In the face of these irregularities it is best to look for a face with an easily recognizable C_4 or C_3 symmetry, then by comparing the angle between that face and it's nearest neighbor you can reasonably discern the orientation of the crystals major axes. These findings can be confirmed through the use of bench-top x-ray diffraction, as will be covered in section 2.2.2.

An astute observer will note that $RPtBi$ materials have the $f\bar{4}3m$ group, which has the point symmetry group of T_d, the chiral tetrahedral symmetry, and not the Octohedral symmetry apparent in the macroscopic sample. In order to understand why certain broken symmetries are lost in moving from the microscopic regime to the macroscopic we should look a little deeper into the energetics that dominate flux solvent growth, and the Wulff construction of crystallization.

The creation of a crystal in solvent is energetically akin to the creation of a

water droplet or the meniscus of water in a glass that is just slightly too full. There is some amount of energy involved in laying a surface of material, we can therefore expect a quantity γ which represents the reversible work dW done to remove a layer of material of infintesimal width dA

$$\gamma = dW/dA \tag{2.1}$$

We wish to minimize $\oint_{A_0} \gamma dA$, the energy involved in creating the surface. In a spherically symmetric system γ is a constant so this is done by minimizing the total area A, which results in a spherical droplet. Liquids are in general spherically symmetric, however solids are not. Nonetheless in a crystal we can reasonably expect γ to be an extrema, and in particular a minimum, along the high-symmetry directions of the crystal.

This is known as the Wulff construction, in which the balancing of the minimum γ is weighted against choosing a minimum surface area A_0. The specifics of this calculation are non-trivial and there are terms (such as edge and corner energy terms) which also need to be considered, however simply by understanding this construction we can know to search for high-symmetry planes along sample facets. [32] It is worth noting that γ only inherits values pertinent to the surface of the material, therefore glide and screw symmetries parallel to the plane do not change the value for γ. It is for this reason that the macroscopic crystal ignores certain broken point symmetries of the underlying crystal which are transformed into one another through glide or screw transformations, and O_h symmetry is recovered.

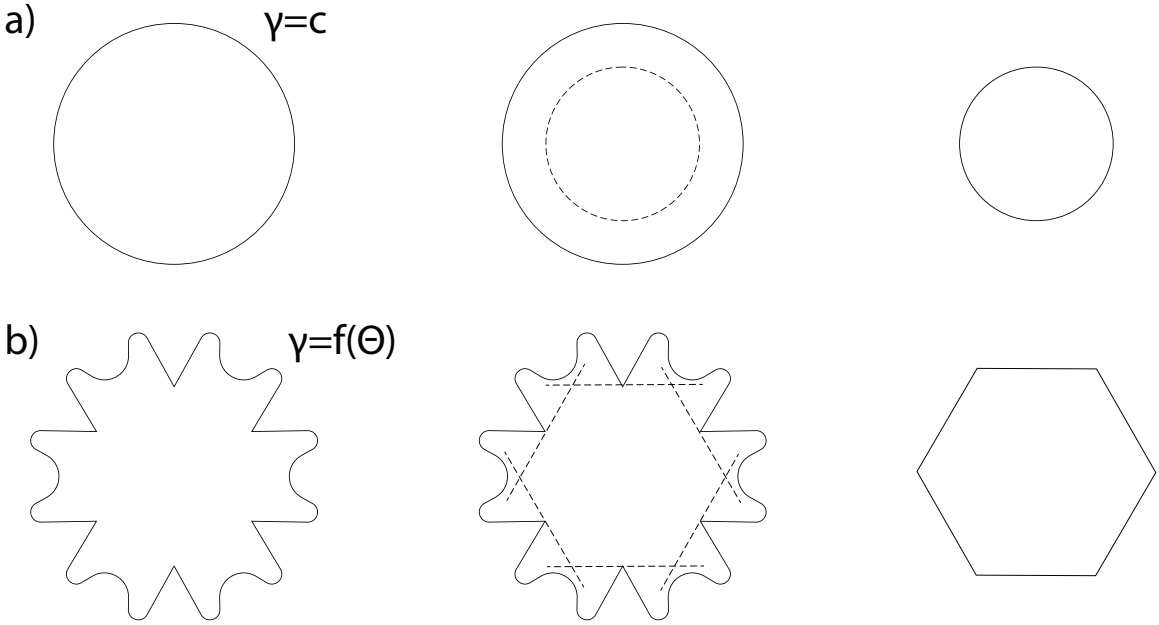

Figure 2.2: Wulff's construction relates the microscopic energetics of a system to its final macroscopic shape. a) Fluids are isotropic, with no long-range orientation dependence. Absent additional forces, positive surface tension will cause a free-flowing fluid to adopt a spherical shape. b) Crystals have a surface tension function with orientation dependence, typically with crystallographic high-symmetry directions being the lowest energy surfaces. A complicated sixfold-symmetric system readily produces a hexagonal precipitate.

2.2.2 X-Ray

Once we have a reasonable guess for a sample's orientation through observation of surface features, we can confirm our results using x-ray diffractometry. By using Bragg's diffraction law and knowing the wavelength and expected value of 2Θ for a given orientation, the orientation of the underlying crystalline axes can be quickly confirmed.

Samples were measured in one of two X-ray diffraction systems. Powder X-ray was conducted using a Rigaku miniflex benchtop system. Powder X-ray was conducted on batch samples prior to measurement in order to establish the creation of intended HoPtBi product and confirm the documented $F\bar{4}3m$ cubic structure. Since the process of powder XRD is destructive it was not used to confirm the structure of samples, but is reserved for identification of growth product.

Single crystal X-ray was conducted using a D8 Bruker double-axis XRD on pre-shaped and polished samples. Samples going in to SC XRD already had a 'good guess' on the proper orientation using the macroscopic features of the sample using the techniques in section 2.2.1. SC XRD was used to confirm that the face of the sample was the expected orientation.

The mechanical process of polishing a well-aligned face is subject to significant error given the size of samples and the presence of fractures or volumous flux deposits on the surface, and many samples had to be discarded due to misalignment of 2° or more. SC XRD is sensitive enough to alignment that even fairly well aligned samples would not necessarily produce a peak without some amount of searching

within the nearby alignment parameters. Samples with misalignment greater than 2° could rarely be identified by SC XRD and were discarded as poorly-aligned. An example of a [100] oriented SC XRD measurement is presented in figure 3.2.

2.2.3 Energy Dispersive X-Ray Spectroscopy

Energy Dispersive X-ray Spectroscopy (EDS/EDX) was conducted using the Hitachi S-3400 Variable Pressure SEM at the UMD Fablab facilities. EDX is an atomic analysis tool which uses electron bombardment and the resulting X-ray emission spectra to identify atomic components of a material to within a few percent (accuracy of roughly 5%). This technique was used to identify the 1:1:1 ratio of Ho:Pt:Bi in fabricated samples. Samples are adhered to a glass plate by electrically conductive carbon tape, which acts as a ground for excess electrons introduced from the e^- beam. Once mounted and placed within the measurement chamber the entire apparatus is sealed and evacuated of any atmosphere. The e^- beam is turned on, tuned to $15keV$ and $50mA$. $15keV$ is chosen because the EDX emission spectra of most heavy elements is well below $10keV$ which allows us to resolve all components of the growth. Finally the spectra can be measured and analyzed for atomic contribution percentage using the ESPIRIT software package, and these numbers can be compared against the atomic formula of the goal material.

2.3 Sample Preparation

2.3.1 Shaping and Polishing

There are a myriad of potential geometries for measuring the properties of materials from the classic linear bar, to the cylindrically symmetric Corbino disk geometry, [8] to the Van der Pauw method and more. Each of which come with individual benefits, draw backs, and particular observables that they are designed to measure. Many measurement geometries require specific fabrication techniques in order to ensure that the measurements are accurate enough within tolerance, for example measurements which search for quantized resistance or negative longitudinal magnetoresistance effects are particularly sensitive and benefit from knowing the exact dimensions of the sample.

Once the relationship between the macroscopic geometry and the microscopic crystalline orientation is established it is time to adapt the form of the crystal to a shape appropriate for measurement.

- Samples decanted from flux must have their apparent surfaces cleaned of any remaining flux material before attempting to use that surface for alignment purposes.

- Once a clean surface is identified a sample is processed via x-ray diffraction to establish the prominent crystallographic direction associated with that surface.

- If large enough a sample can be rough-cut using either the wire-saw or spark-

cutting methods. Wire-saw cutting is good for very large samples and will generate an deep and wide cut about 0.5 mm thick. Spark-cutting can be done down to roughly .2mm in thickness and creates a flatter face however the high voltages involved can cause pitting and chemical changes to the surface of your material, so care must be taken to polish any spark-cut surface. Neither of these methods will guarantee a well-oriented surface so care must be taken to maintain an oriented surface while cutting.

- Next the sample is adhered by the appropriate face to a polishing platform using crystal bond. The platform is designed to be as close to exactly parallel to the polishing material as possible, therefore establishing that the polished surface will represent the same orientation as the identified face from x-ray diffraction

- Samples are rough polished using 1000 grit Aluminum-Oxide in order to remove the majority of the material and bring the sample within a few dozen μm of the intended thickness. During this step the sample should be routinely checked for inclusions. Ideally inclusions will present as a different reflectivity or overall color, however it is up to the human eye to pick out any details that signal inclusions. If an inclusion is at the edge of the sample and leads can be placed on pure sample surface then it can be tolerated, however inclusions that run into the length between two leads (in particular the voltage leads) will short the sample and provide an anomalous contribution to resistivity.

- Using a 90degree angled step the edges of the sample are polished away and the

intended bar shape is created. In-plane geometry of the sample is determined at this point so knowledge of the samples orientation and the shape of the planar cut made in the previous steps should be used to determine which direction is preferred for the contact orientation.

- After the sample is polished according to its intended final geometry the final step is to use finer polishing pads to increase the quality of the surface. As a general rule the sample surface will have scratches and microscopic cracks roughly the size of the particles used to polish. Therefore for an arbitrarily good surface, incremental polishing with finer and finer particles is the best method to create a clean surface.

In this dissertation samples were finely polished using a pad of $.5\mu m$ Aluminum Oxide particles which was sufficient to create a light reflective surface. Samples of HoPtBi would retain their clean reflective surface over long exposure times to air, but to cut down on potential oxidation samples were kept in a glove box with $< 0.5ppm\ O_2$ when not being actively manipulated or measured.

2.3.2 Transport Configuration

Once a sample has been shaped to the appropriate geometry the next step is to attach electrical contacts to measure intended observables. The contacts usually serve one of two primary purposes: applying a fixed current $\vec{J}$ to the system, or measuring a potential difference between two points $\vec{V}$. In essence two current leads and two voltage leads will help determine an element in the Resistance tensor of the

material:

$$V_i = R_{ij} J_j \tag{2.2}$$

knowledge of the sample geometry (established by good sample preparation in section 1.3.1) helps reduce this to knowledge of the more general electric field and resistivity tensor:

$$E_i = \rho_{ij} J_j \tag{2.3}$$

For this dissertation the primary geometries are the conventional four-wire longitudinal and the four-wire transverse (aka Hall) measurements. It is however possible to compound these measurements into a six-wire measurement which is capable of measuring both the longitudinal and transverse components, and alternatively it is possible to do a longitudinal measurement with a two-wire technique. Each technique has its own distinct set of advantages and disadvantages covered below.

Four Wire Longitudinal: In this technique the current and contact leads are applied sequentially along the length of the material, ideally with each lead forming a uniform contact across the width of the sample. Since J_j and the measured electric field response E_i are collinear in this geometry it is used to analyze diagonal components of the resistivity tensor ρ_{ii} which are the conventional resistivity values

typically associated with e.g. a length of conventional conducting wire in typical (i.e. no applied magnetic field) conditions.

Four Wire Transverse: the transverse geometry is similar, with the exception that the voltage contacts are now located on opposite edges of the sample, opposite one another, and are affixed to the material through a point-like contact. This geometry measures the off-diagonal components of the resistivity tensor ρ_{ij} and is associated with the Hall effect in conventional metals.

Six Wire: The six wire measurement is quite simply the use of a single pair of current leads to simultaneously measure both the longitudinal and transverse components by having voltage contacts for both geometries on a single sample during a single measurement.(figure 2.3) This geometry has the convenience of measuring both set of resistivity values for a fixed $\vec{J}$ without worrying about varying sample integrity from handling or oxidation. Furthermore since a single, unchanged sample is used for both measurements simultaneously the thickness value is fixed for both geometries, which simplifies a number of important calculations that take the ratio of longitudinal to transverse resistivity, such as Hall angle, and cancels out one degree of uncertainty in these measurements.

On the other hand six wire measurements have three primary drawbacks. First it makes contact creation exponentially more difficult as more wires have to be accurately placed within a fixed volume without touching. This is a trivial concern for large samples but can be very limiting for $< 1mm$ samples. Second for highly resistive samples the presence of additional highly conductive leads can short the measurement to a limited degree, introducing a different source of error into your

measurements. In effect your transverse contacts will reduce the resistivity value of a longitudinal measurement and vice versa. Finally this type of measurement is not the default for resistance measurements in the PPMS or Dynacool systems and will take up two channels, reducing the number of samples that can be concurrently measured.

Two Wire: In the event of exceptionally small samples a two wire measurement can be attempted. In a two wire configuration voltage and current leads of a given polarity share a single point of contact, therefore a two wire measurement is only feasible for measuring the longitudinal component of resistivity. Furthermore since the current and voltage leads share a single point of contact the voltage difference as measured by the voltage leads will include some amount of contribution from the leads and contacts. As a result this measurement is unreliable for samples with very small resistances comparable to the gold wire and silver contacts, and in particular this measurement is a very poor choice for measuring any superconducting behavior such as T_C or H_{C2}. In these cases the intrinsic signal of the sample is dwarfed by the contribution from the leads, no matter how small.

2.3.3 Leads and Contacts

Once a decision is made on how to position and affix leads the final step is to choose an appropriate method of creating electrical contact. This, in essence, involves making the decision between several different types of electrical wires and several different types of electrical contacts.

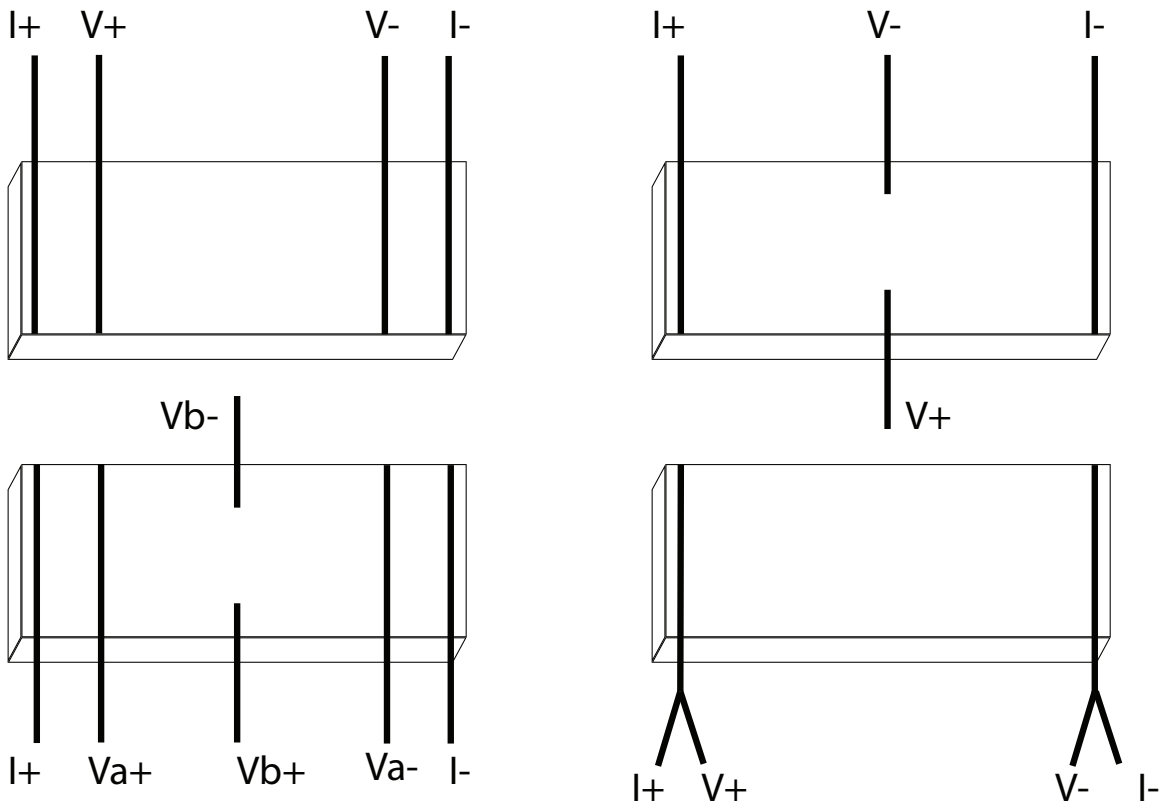

Figure 2.3: Clockwise from top left: Four-wire longitudinal, four-wire transverse (Hall), two-wire, and six-wire lead configurations. In case of four-wire transverse and six-wire measurements the Hall contacts are labeled as to give a positive value if charge carriers are positive (hole-like).

The primary decision for choosing an electrical wire is material (typically gold or silver) and thickness. Wire thickness is usually predicated on the size of the sample involved, with thicker wires more likely to create large and diffuse contacts while smaller wires create more confined contacts, but are more difficult to create in a spatially homogenous way. Additionally larger wires are more difficult to fit into a small space, but offer increased durability relative to their smaller counterparts. Gold wire is the standard used in our lab, however silver wire is not uncommon and is more rigid at the expense of being more brittle. Specialty wires, such as manganin, can be used in cryogenic measurements but are usually reserved for special measurements such as in pressure cells.

For the contact that fixes the leads to the sample there are three primary options: silver paint, silver apoxy and soldered contacts. In our lab we use

Silver paint: this is the least durable option but the easiest to use, most flexible and has a middle-range contact resistance $\approx 1\Omega$. Silver paint comes in solution which contains colloidal silver particles and is typically mixed in a 1:1 ratio with $2-Butoxyethylacetate$ which acts as a quick-drying flux. Once created contacts are quite fragile and can easily be ripped off of a sample if carelessly handled, however such weak contacts pose no threat to anything but the most fragile or micaceous of materials. Silver paint is also very easily removed through the use of acetone and mild sonication, and as such are usually the first-choice for making contacts due to their ease of removal and resetting.

Silver Epo-Tek: the next most durable option is silver apoxy. Apoxy forms the least desireable contact with contact resistance in the $2-10\Omega$ range. The silver

apoxy we use in our lab is *Epo-Tek H20E* which comes in a two part solution (type A and type B) which are stored separately. Right before creating contacts these two solutions are mixed which creates a homogenous silver fluid that will not dry in room temperature conditions over time scales applicable to lab work. Once leads are placed with silver apoxy on the sample, the sample needs to be heated for some period of time (2hrs at $150°C$ is typically sufficient) in order to cure the contacts. Prior to curing samples can be washed with acetone to remove any apoxy if an error is made in applying contacts, however after contacts are cured the process becomes more complicated. If you wish to remove cured apoxy leads the sample will need to be bathed in dichloromethane (CH_2Cl_2) for 5min-1hr if necessary. This softens up contacts such that they can be mechanically removed (typically with a razor) after which sonication in acetone should remove any remaining residual contact. Alternatively if the sample is thick enough the apoxy and contacts can be removed by polishing the surface away. Apoxy contacts which have not been treated with dichloromethane are durable and will typically outlast the wire to which they are affixed.

Soldered contacts: finally soldered contacts are by far the most durable contacts available for benchtop sample preparation. Contact resistances for soldered contacts are tiny at $\approx 0.1\Omega$ however once attached soldered contacts are essentially permanent and cannot be removed or replaced, this makes them a technique typically of last resort. Soldered contacts are created by dipping the lead in solder flux, and bringing it together with a small droplet of solder located on a fine-tipped solder iron together at your intended point of contact. The need to maintain control over

not just the contact wire, the solder, and the sample, but all three mutual elements together means this is an advanced technique best practiced before use on difficult to replace samples.

In this dissertation contacts were primarily made using silver paint or silver apoxy, as the high relative resistance of semiconducting materials and the lack of superconducting order as our focus meant these contacts were more than sufficient for our purposes.

2.3.3.1 Miller Index Convention

In this dissertation numerous measurements will involve comparing or manipulating the orientation of magnetic fields or electrical contacts. For practical reasons electrical contacts will be fixed during a single measurement, but may vary between measurements. Magnetic field can be dynamically adjusted in-situ through use of a rotator. For this reason Miller indices will be used in a consistent manner in order to minimize confusion.

Rotation measurements will specify the plane of magnetic field rotation using Miller index notation, $\{hkl\}$. In measurements that involve electrical transport labeled as '[100]', contacts will be applied such that $\vec{E}$ is oriented along the [001] axis. These measurements are generally concerned with the C_4 symmetry projection of the cubic system. In electrical transport measurements labeled as '[111]' the contacts will be applied such that electric field is along the $[1\bar{1}0]$ axis. These conventions were chosen such that electric and magnetic fields could be applied at 90° while

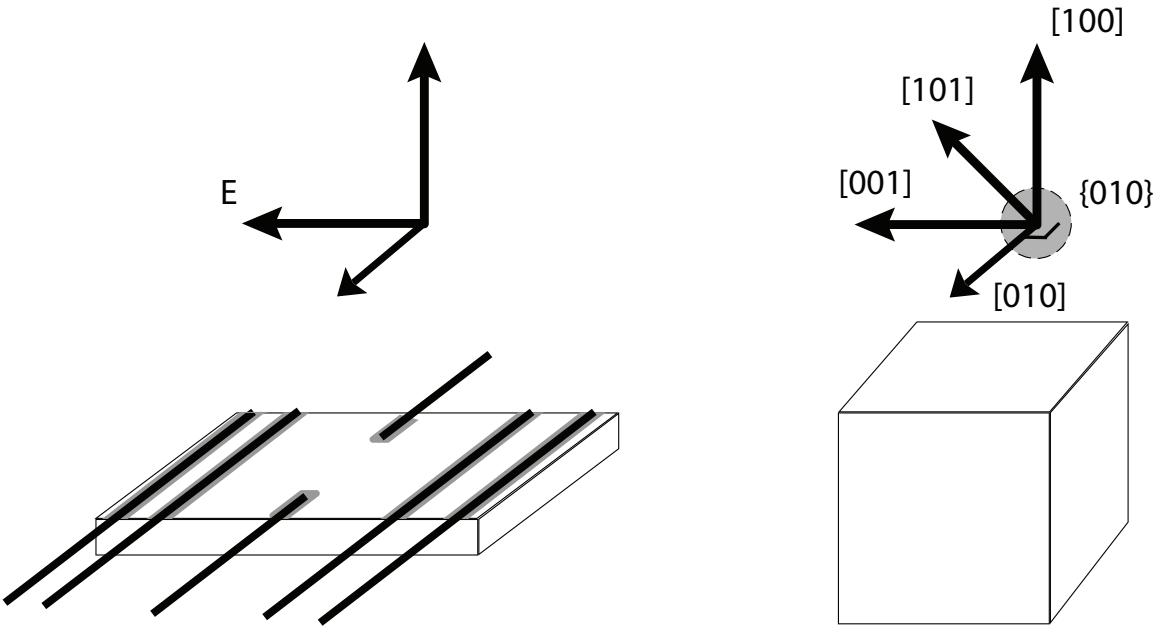

Figure 2.4: Miller indices conventions used in this dissertation. A sample with a possible six-wire lead configuration is shown. A corresponding set of Miller directions are labeled, as well as an example plane. In most transport measurements $\vec{E}$ is fixed along the [001] direction or [011] in the case of [111] measurements. When specifying a rotational plane the Miller plane index will be used to indicate the chosen rotation plane.

retaining good in-plane orientations. Rotation measurements are labeled by the plane in which the field is rotated, e.g. {001}.

2.4 Measurement Systems

Transport measurements below 14T and above 1.8K were conducted in either a Dynacool 14T PPMS or a Quantum Design 14T PPMS system. Susceptibility measurements were conducted in a 7T MPMS or the Dynacool 14T system using the VSM (Vibrating-Sample Magnetometer) option.

2.4.1 Temperature and Magnetic Field Control

Temperature control is similar between these listed systems and is achieved through evaporative cooling on a pool of liquid He. The equilibrium boiling temperature for He is 4.2K which is too high for our purposes, so conventional cooling by liquid He is insufficient. To achieve temperatures below 4.2K the gaseous He is pumped out of the system, as a result the equilibrium point between evaporation processes and condensation of the gaseous He drops and the liquid cools further in temperature. In order to adjust temperature to a desired fixed point this cooling process is balanced against an electric heating element. By combining heating and cooling methods with a temperature sensor located very close to the sample a stable temperature can be achieved anywhere from 1.8K to 310K with ease.

A magnetic field is created by passing an electrical current through a longitudinal coil of superconducting material. The sample platform resides within the interior of the solenoid of superconducting material, creating a uniform uniaxial magnetic field profile. Using this method stable fields can be reached up to 14T (140,000 Oe).

2.4.2 Sample Orientation

In addition to the previous control methods samples can be rotated relative to the sample space using a simple mechanical rotator attachment for the Dynacool or PPMS systems. While application of current across a sample is necessarily fixed to the contacts during a measurement, by use of a rotator it is possible to change

the orientation of the magnetic field relative to the sample. The rotator only has one axis around which it has a 380° range of motion, so axis of rotation must be carefully chosen prior to measuring the sample.

Rotation measurements typically are chosen in one of three primary configurations.

Transverse: in this configuration the axis of rotation is in the {001} plane, and consequently the magnetic field is always transverse to current. In the case of a cubic system (such as GdPtBi and HoPtBi) if the current is along the [001] direction then the magnetic field consequently sweeps out a C4 symmetric plane through the [010] and [100] directions, also traversing the [110] and $[1\bar{1}0]$ orientations by necessity. Since magnetic field and current retain a 90° relative orientation throughout this type of rotation measurement should only be sensitive to either geometric factors or the crystalline symmetries of the compound.

Longitudinal: in this configuration the axis of rotation is {010}, along the edge of the bar sample. Therefore the field rotates from perpendicular to the sample (out of plane) to in the plane of the sample, along the electric field. This rotation is sensitive to the orientation between electric and magnetic field, in addition to the geometric and crystalline considerations of the transverse case.

Planar: finally the last configuration has the plane of rotation {100}, ie in the plane of the material. Intrinsically this shouldn't be different from the longitudinal case for two, or four-wire longitudinal measurements outside of geometric considerations. However if this rotation is done for a Hall measurement then the magnetic field is in plane of both the contacts and the current. For semi-classical Hall effect

this should be a zero signal, however in the case of materials exhibiting the Planar Hall Effect a sinusoidal signal should arise from this configuration.

2.5 Measurements

In this dissertation the focus will be on bulk transport phenomenon with some support from magnetization effects.

2.5.1 Electrical Transport

Electrical transport refers to the collective behavior of the resistivity tensor discussed in section 1.1.4 and 2.3.2 under various conditions of temperature and magnetic field, as well as other conditions not considered in this dissertation. Samples were wired up according to geometries discussed in section and attached to a measurement puck by their leads. Low-temperature N grease was used to create a thermal contact between sample and puck, then the puck was inserted into a PPMS or Dynacool system as described in section 2.4. From there control over the sample environment was used to evaluate resistivity as a function of temperature and magnetic field.

2.5.2 Magnetoresistance

Magnetoresistance is a deeply complicated topic that bridges a number of phenomenologically similar, but causally distinct experimental results. The simplest magnetoresistance phenomenon is attributed to increased scattering from magnetic

path deflection, however in many ordered compounds the application of magnetic field can have a significant effect on magnetic scattering rates, or can change the type of ordering inducing a change in MR character. [24] In this dissertation we will focus on a material which has novel MR character dependent on magnetic field orientation, which we do not expect for a paramagnetic material. In addition at high fields the material undergoes a specific form of MR response known as Shubnikov de Haas oscillations, which will be a useful diagnostic of the Fermi surface.

2.5.2.1 Shubnikov de Haas

Shubnikov de Haas oscillations are a specific form of high-field MR signal that is oscillatory in increasing field. SdH is a form of quantum oscillations (QO), in which the Landau quantization condition begins to strongly influence the transport properties of the system. As field increases the Landau phase quantization is convolved with the Fermi surface area as projected along the applied field axis. DoS will increase sharply when the Landau phase condition as determined by field matches the Fermi surface area extrema, and will decrease sharply between satisfied Landau phase conditions. The result is an oscillatory signal in observables that depend strongly on DoS, such as the longitudinal conductivity. [33]

The cross section of the allowed Landau levels in k-space is

$$A_k = (n + \gamma)2\pi\alpha \tag{2.4}$$

where γ is a non-zero correction term that depends on the details of the Hamiltonian,

and $\alpha = \frac{eB}{\hbar}$. For a given, non-field dependent Fermi surface the maximal intersection occurs at a fixed projected area extrema, and oscillations occur as the Landau levels corresponding to each successive level satisfying the fixed-area condition. By looking at oscillations in the $1/B$ basis a clear oscillatory period can be extracted [34]

$$\Delta(\frac{1}{B}) = \frac{2\pi e}{\hbar}\frac{1}{A_{k,ext}}. \tag{2.5}$$

In HoPtBi oscillations onset around 10T and are of quite low frequency. For this reason conventional magnetoresistance measurements in the 14T PPMS or Dynacool systems was insufficient to reach the necessary fields required to appropriately characterize the system. Samples were taken to the National High Magnetic Field Lab (NHMFL) in Tallahasee, Florida where field sweeps up to 35T were achievable. Leads were attached by silver paint in the four-wire longitudinal configuration and attached to a custom rotator by low-temperature N-grease.

The {010} plane was chosen for the plane of rotation for applied field $\vec{B}$ i.e. the field would be rotated from the conventional $\vec{B} \perp \vec{E}$ configuration, with $\vec{B}$ oriented perpendicular to the sample, through the longitudinal $\vec{B} \parallel \vec{E}$ configuration. This allowed the field to sweep through the [100], [001], and [101] crystalline high symmetry directions.

Shubnikov de Haas results are discussed in section 5.2 and a closer inspection of the techniques used to extract the frequency information from low-frequency SdH data is covered in Appendix A.

2.5.2.2 Hall Effect

A brief discussion of the definition and sources of Hall Effect are covered in chapter 1 of this dissertation, in this section we will discuss how Hall effect measurements were conducted. Samples were shaped into a longitudinal bar shape in transverse four wire configuration using silver paint for contacts with minimal ($\approx 1\Omega$) contact resistance. In the case of certain repeated measurements where the sample had to be manipulated between measurements without losing leads silver apoxy was used instead of silver paint in order to create more durable contacts.

Hall Effect measurements are asymmetrized in field in order to minimize contribution from geometric imperfections in the sample or from lead misalignment. In the case of field sweeps data was collected for the full range and data points of opposite field were asymmetrized. In the case of fixed field temperature sweeps two measurements of opposite field would be conducted under the same initial conditions. Where feasible measurements were conducted under zero-field cooled conditions, however this was done out of an abundance of caution as repeated magnetization and neutron diffraction measurements found no magnetic order in the range of most measurements conducted.

2.5.2.3 Hall Angle

Hall angle measurements are a composite of Hall Effect and longitudinal conductivity.

$$\Theta_H = \frac{\sigma_{xy}}{\sigma_{xx}} \tag{2.6}$$

Note however that we do not measure conductivity of materials directly, instead resistance (which can be directly converted to resistivity, if the geometric factors are known) is measured and conductivity must be calculated.

$$\sigma_{xx} = \rho_{xx}^{-1} \tag{2.7}$$

$$\sigma_{xy} = \frac{\rho_{yx}}{\rho_{xx}^2 + \rho_{yx}^2} \tag{2.8}$$

Due to the ratio of conductivities errors from sample geometry and lead placement was reduced by maintaining the same sample between measurements.

2.5.3 Magnetization

Magnetization is acquired through the use of a Vibrating Sample Magnetometer option of the Dynacool PPMS system. A sample is first adhered to a quartz rod using GE varnish. The varnish acts as a physical contact between sample and rod, preventing movement or rotation. A pickup coil is inserted into the sample chamber. The quartz rod and sample are mounted to a linear motor and then inserted into the sample chamber.

A small field is applied in order to center the sample. The centering process is handled automatically, but consists of the sample and rod being lowered in the

pickup coil and dynamically measured as a function of vertical displacement. The response curve is used to determine the ideal placement of the sample. Since HoPtBi is a large moment paramagnet this centering measurement could be done at room temperature.

Once the sample is centered the field is then set to $0Oe$ using the oscillate approach (which produces the most accurate final field) and temperature is lowered to base temperature of $1.8K$. From there the measurement of either field sweep or temperature sweep is conducted in sequence. Knowledge of the sample mass and molar mass is used to determine the magnetic field response per Ho atom, which is used in subsequent calculations of Curie constant and effective bohr magneton response.

2.5.4 Torque Magnetometry

The final measurement technique was torque magnetometry, a technique which is not sensitive to the total magnetic response of the material but measures the difference between the microscopic moment and the applied field direction. Due to the large magnetic response of HoPtBi and the delicate nature of the sample platform an extremely small sample ($\approx 0.1mg$) sample was used to prevent the possibility of breaking the lever mount through excessive magnetic torque.

A magnetic field is applied and the sample platform is vibrated. The response of the platform to this vibration is used to determine the force applied by torque from the sample, $\tau = \vec{m} \times \vec{B}$ where $\vec{m}$ is the magnetic moment of the material. In an

isotropic paramagnet $\vec{m}$ and $\vec{B}$ are coalligned and torque is zero. If the microscopic moment is pinned to some easy axis however, either through interactions or through magnetic ordering there will be some non-coalligned response which will induce a measureable torque.

Chapter 3: HoPtBi Characterization

3.1 HoPtBi Growth

HoPtBi was grown by conventional flux method. About $5g$ of Ho:Pt:Bi were combined in a 2.5mL crucible in a 1:1:20 ratio. Growths with a ratio of 1:1:10 were attempted however it was found that a surplus of Bi flux was ideal for creating a smaller number of larger crystals.

Samples were placed in a 1200° C box furnace. Samples followed a regular heating schedule beginning at 20° C, heated at a rate of 50° C to 1050° C. Samples dwelled at 1050° C for 5hr to guarantee thorough dissolution of materials into flux. The furnace was then slowly cooled at 3° C/hr to facilitate SC crystal growth, and were finally spun out using a centrifuge at $520°C$

HoPtBi crystals were about $1-1.5mm^3$ in size and formed in an approximation of a cantellated cube (figure 3.1). [100] and [111] faces were prominent and easy to identify except in cases of severe malformation of the sample surface. [110] faces were exceptionally small and often would not grow at all, though there were exceptions. These surface features were used to orient samples for shaping and polishing before confirming orientation through XRD.

3.2 HoPtBi Structure

Before we can understand the specific intricacies of HoPtBi it is necessary to establish its fundamental behaviors and, to the extent possible, describe them with conventional models. In this chapter we will provide the basic tools for characterizing HoPtBi

In studying new solid state materials it is fundamental to understand the structure of the system and characterize their properties. This is particular true in RPtBi Weyl semimetals candidates where magnetism and lattice constant are important potential controlling parameters for the band-inverted state. [13]

3.2.1 EDX

I performed EDX measurements on well-formed crystals of HoPtBi growth to identify intended product. An example spectrum is presented in fig. 3.1. Spectrum weight analysis using ESPIRIT package always identified Ho, Pt, and Bi compounds in the $31 - 34\%$ atomic contribution range, corresponding to 1:1:1 elemental components to within the accuracy of the EDX system. After several consistent EDX measurements I determined that the cubic crystal could be easily identified visually, and EDX was forgone in favor of SC XRD as an identification confirmation method for individual samples.

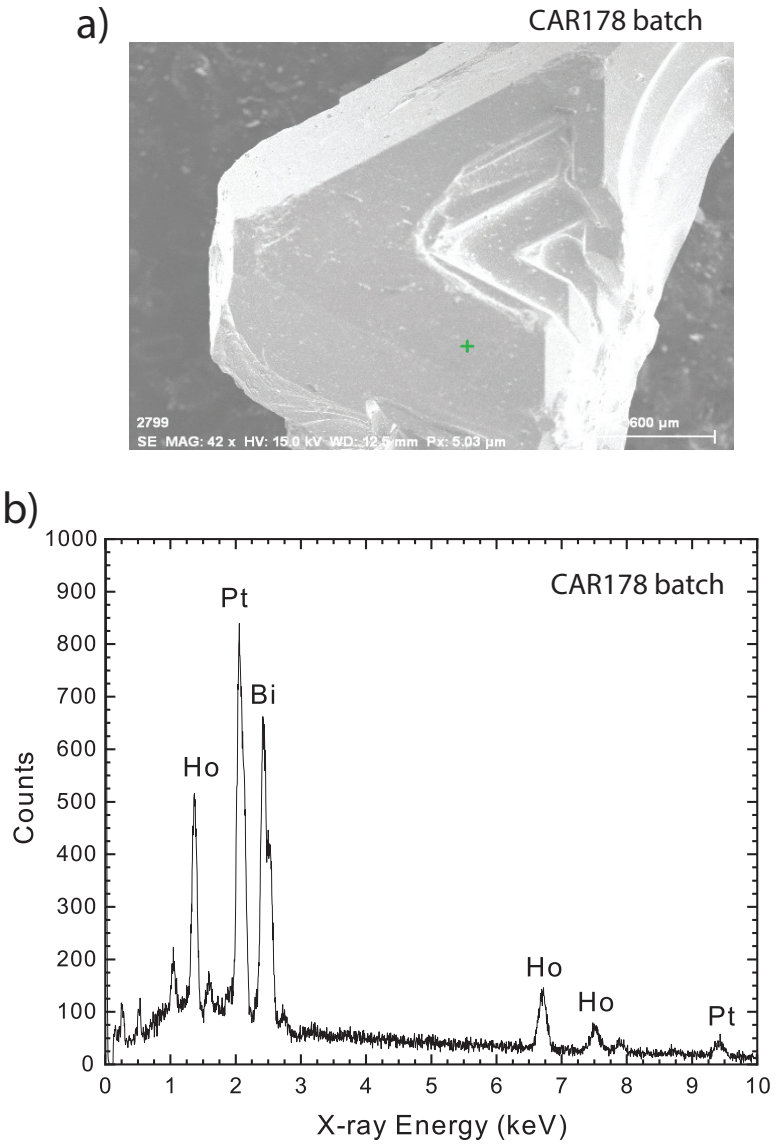

Figure 3.1: An e^- beam image of HoPtBi showing the triangular [111] oriented facet. Some minor growth defects (cavities) are visible, as well as leftover flux on the surface. An associated EDX spectrum showing prominent Ho, Pt, and Bi peaks indicating a 1:1:1 contribution of components as expected.

3.2.2 XRD

I used powder and single crystal X-ray diffraction to confirm the cubic $F\bar{4}3m$ structure of HoPtBi. Powder diffraction was done using a Rigaku Miniflex benchtop XRD system and was analyzed using PDXL.

Single crystal XRD was used to confirm sample alignment and establish expected lattice parameters before proceeding with measurements. Example SC data sets are provided in 3.2. SC XRD was performed using a D8 bruker double axis XRD using a Cu $K\alpha$ source. SC sample alignment by double-axis XRD is a precision process, unlike powder XRD which uses a mosaic of microscopic particles to span the $[hkl]$ space for particular diffraction peaks, SC XRD samples must be pre-aligned to the appropriate facet to within fractions of a degree. As a result SC XRD is an excellent tool for guaranteeing proper sample alignment. In the event of a minor misalignment control over the axes of the XRD allowed a limited search for the appropriate $[hkl]$ alignment, however this was never successful for misalignments greater than 2° and numerous samples which could not be effectively aligned had to be discarded.

3.3 Magnetic Order in HoPtBi

In order to understand how AMR in HoPtBi arises it is crucial to first understand the magnetic state. We studied the magnetization response of HoPtBi using the Vibrating Sample Magnetometer option on a Quantum Design Dynacool PPMS system (VSM). Additionally the magnetic order of the material was directly probed

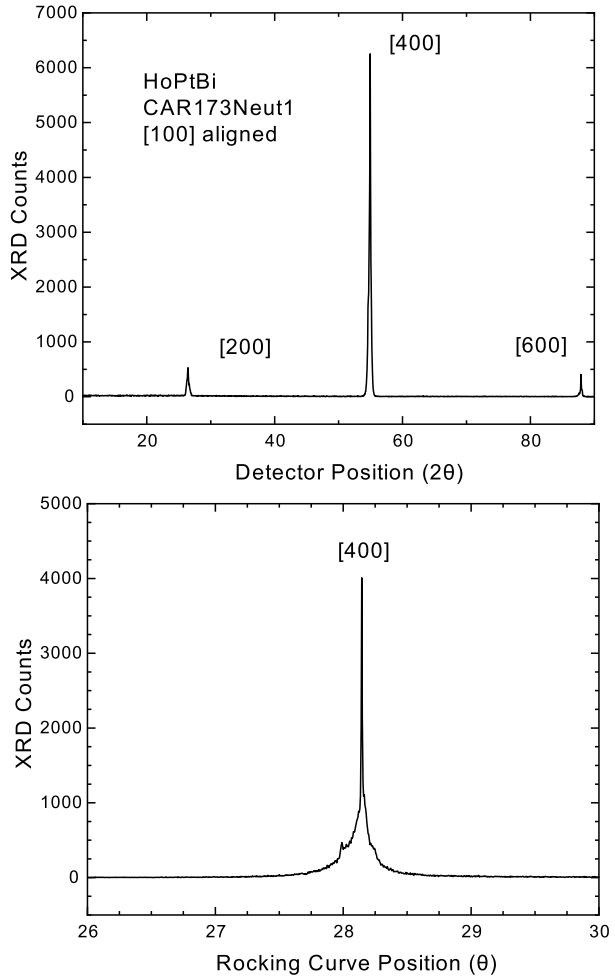

Figure 3.2: An example of SC X-ray diffraction analysis. 2θ detector sweep is presented for a crystal aligned to the [100] orientation, showing the [$2l$00] peaks present for the $F\bar{4}3m$ structure (odd diffraction peaks destructively interfere and have zero counts). A rocking curve is presented for the same spectrum centered on the [400] peak, showing a highly localized diffraction peak (FWHM$\approx .01^{\circ}$) indicating good sample quality.

by Neutron beam diffraction on the BT-7 beam line at the NIST Center for Neutron Research (NCNR) in collaboration with Lekh Poudel and Jeffrey Lynn using a triple-axis spectrometer.

3.3.1 Neutron Diffraction

Triple-axis Neutron diffraction showed a magnetic ordering temperature T_N of $1.25K$ with a scattering wave vector of $q = (0.5, 0.5, 0.5)$ which corresponds to (1,1,1) oriented antiferromagnetic ordering. [35] For base temperature $100mK$ the peak is robust, by applying a field along the (110) crystallographic axis the T_N is completely suppressed with a moderate $H_C = 2.5T$. As temperature increases, especially above $1K$ the peak intensity and suppressing field begin to decrease due to destabilization of the AFM state. Above $1.25K$ the peak is fully suppressed and the system is in an unordered state regardless of field. Due to low magnetization anisotropy below 4T we expect similar suppression field H_C for magnetic fields applied along other arbitrary directions. This matches the paramagnetic and AFM order usually found in Rare Earth platinum and palladium-bismuthides [36] [37] [12]

3.3.2 Susceptibility

The vast majority of our resistive measurements were conducted above $T_N = 1.25K$ in the magnetically disordered state. We conducted magnetization measurements of HoPtBi in this regime to establish the nature of the magnetic response. Given that the 4f-electron states in HoPtBi are strongly localized and there is an ex-

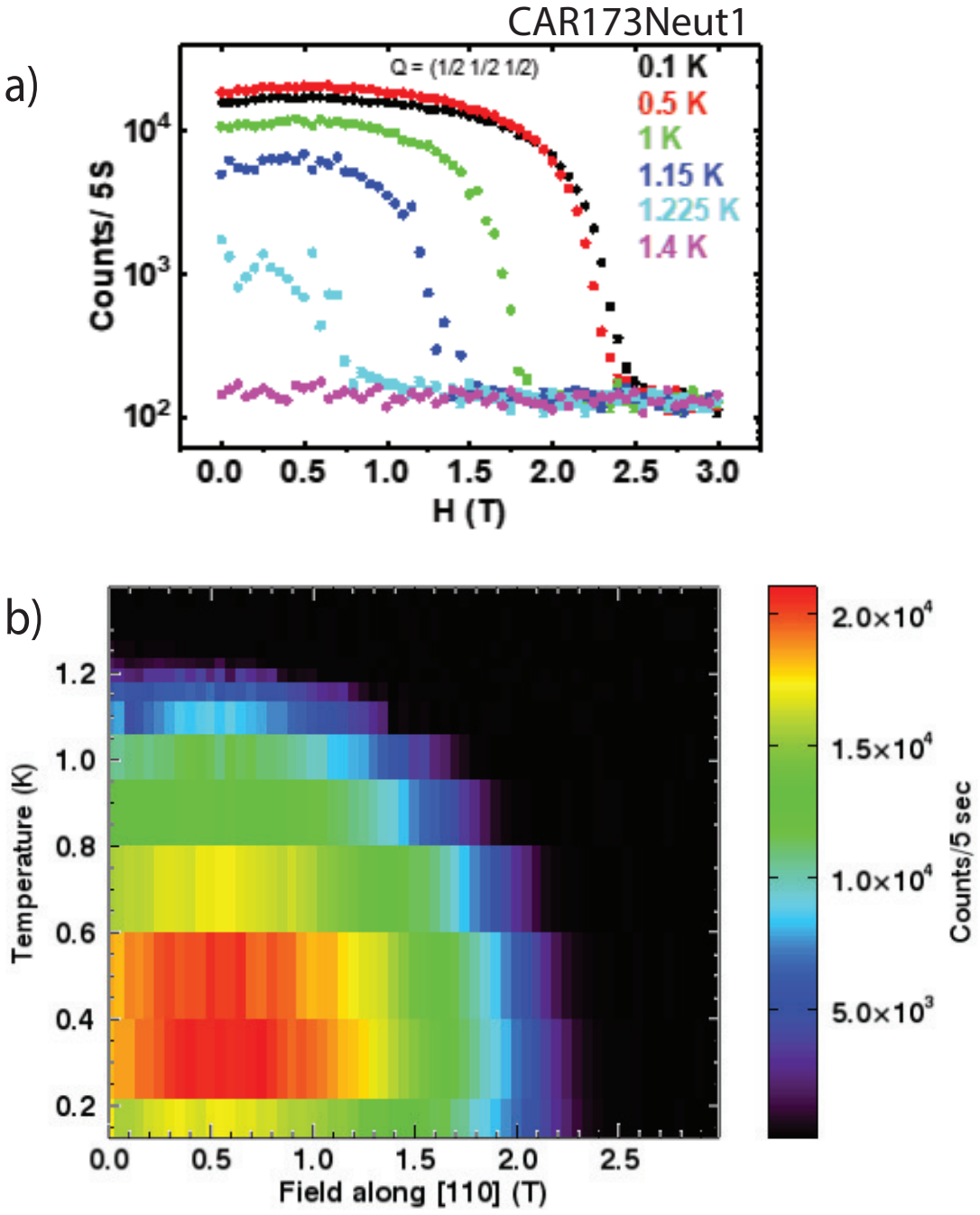

Figure 3.3: Neutron scattering for $Q = (0.5, 0.5, 0.5)$ with field oriented along [110] direction. a) Raw counts at fixed temperature and sweeping field. b) Contour map of counts as a function of field and temperature showing low-temperature and low-field AFM phase.

ceedingly low carrier density of $10^{18} e/cm^3$ we anticipate that the Curie-Weiss law of solids with some AFM perturbations will best represent the material in the low-field regime. [38]

$$M = \chi H \tag{3.1}$$

$$\chi = \frac{1}{3}\frac{N}{V}\frac{\mu_B^2 p^2}{k_B(T - \Theta_C)} \tag{3.2}$$

$$p = g[J(J+1)]^{1/2} \tag{3.3}$$

We measured magnetization as a function of temperature at various fields. This measurement was split into two components, for low field measurement was conducted on well-oriented, large (mass $\approx 50mg$) samples in order to well characterize the CW paramagnetism. (figure 3.4) A second round of measurements were conducted on a much smaller sample (mass $\approx 5mg$) in order to access high fields. (figure 3.5) High field measurements were inaccessible to large-mass samples as the magnetic force would cause the sample to detach from the quartz VSM rod, rendering high field inaccessible.

Low, fixed field temperature-sweep measurements are presented in (figure 3.4). Samples follow a modified Curie-Weiss paramagnetic behavior, linear in $1/T$ with AFM perturbations with Weiss constant $\Theta = -9K$ and effective bohr-magneton

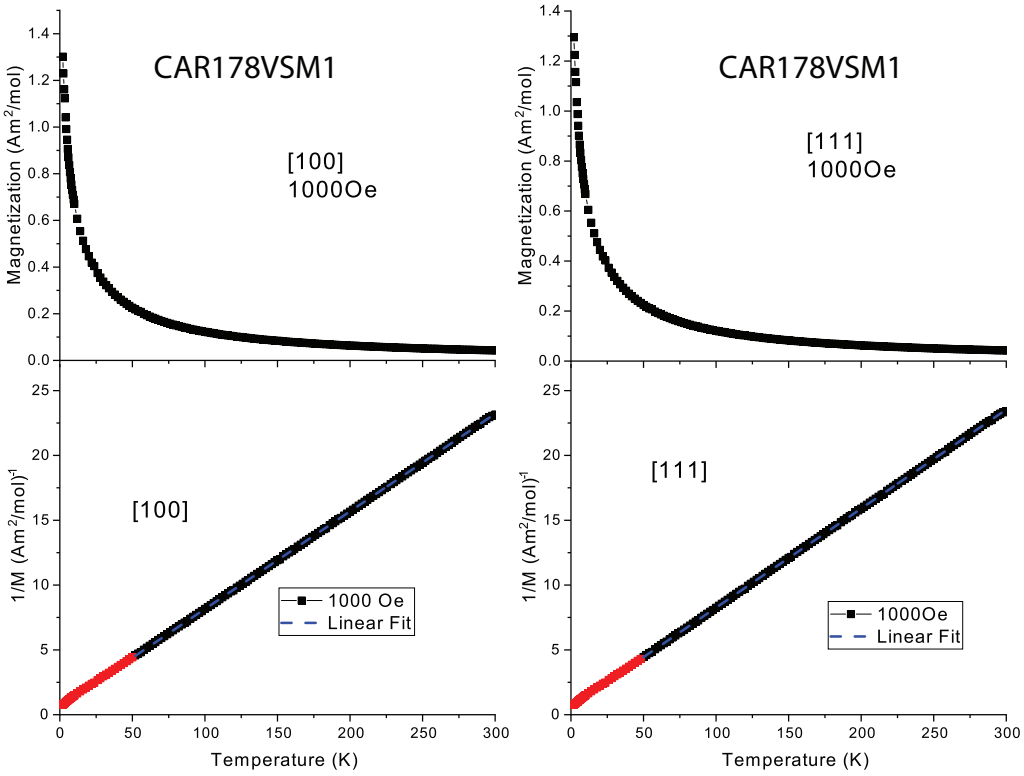

Figure 3.4: Example data set for Curie-Weiss like magnetization with field applied along [100] and [111] directions by a large mass $m \approx 50mg$ sample. Fitting of the Curie-Weiss coefficient above $50K$ finds an effective Bohr-magneton number of $p = 10.3\mu_B$ and a Weiss constant of $\Theta = -9K$ corresponding to AFM-type perturbations. Below $50K$ fits begin to slightly deviate as AFM perturbations begin to dominate the magnetization.

number $p = 10.3$, which is slightly below the value for free $Ho^{3+} p = 10.6$. [38] Fits to a CW paramagnetic model are presented in (figure 5.2) for temperatures above $50K$ and in low-field ($1000Oe$) the $1/T$ dependence is consistent down to low temperatures, though there is some deviation near base temperature. No transition is observed as measurements do not extend below $T_N = 1.25K$ and there is no additional indicator of magnetic order above T_N.

We measured magnetization as a function of field at various temperatures from $2K$ to $100K$. (figure 3.5) Higher temperatures present a situation consistent with the Curie Weiss paramagnetism, with linear magnetization in the $k_B T >> g\mu_B H$ regime. For very low temperatures the behavior begins to deviate from the expected J=8 Curie-Weiss behavior. This behavior is visible up to $10K$ in figure 3.5. For measurements $37K$ and above the linear, low-field regime remains however saturation regime is pushed above 14T. There is some deviation from CW in the saturation regime. This is expected as Curie Weiss formalism cannot be made into a closed analytical form when taking into account AFM perturbations.(figure 3.5) [34]

So long as the temperature scale $k_B T$ exceeds the magnetic energy scale $g\mu_B H$ the behavior is a familiar constant susceptibility associated with isotropic paramagnets. For higher field scales where $g\mu_B H > k_B T$ the magnetization approaches saturation. For Ho this equates to $1.2T$ field per $1K$ increase in temperature. Near saturation HoPtBi begins to deviate from the conventional CW paramagnet law, magnetization begins to tail off before reaching the CW saturation point. This is not unexpected as the same AFM perturbations that cause the Weiss constant shift in paramagnetism are a good candidate to curtail paramagnetic saturation.

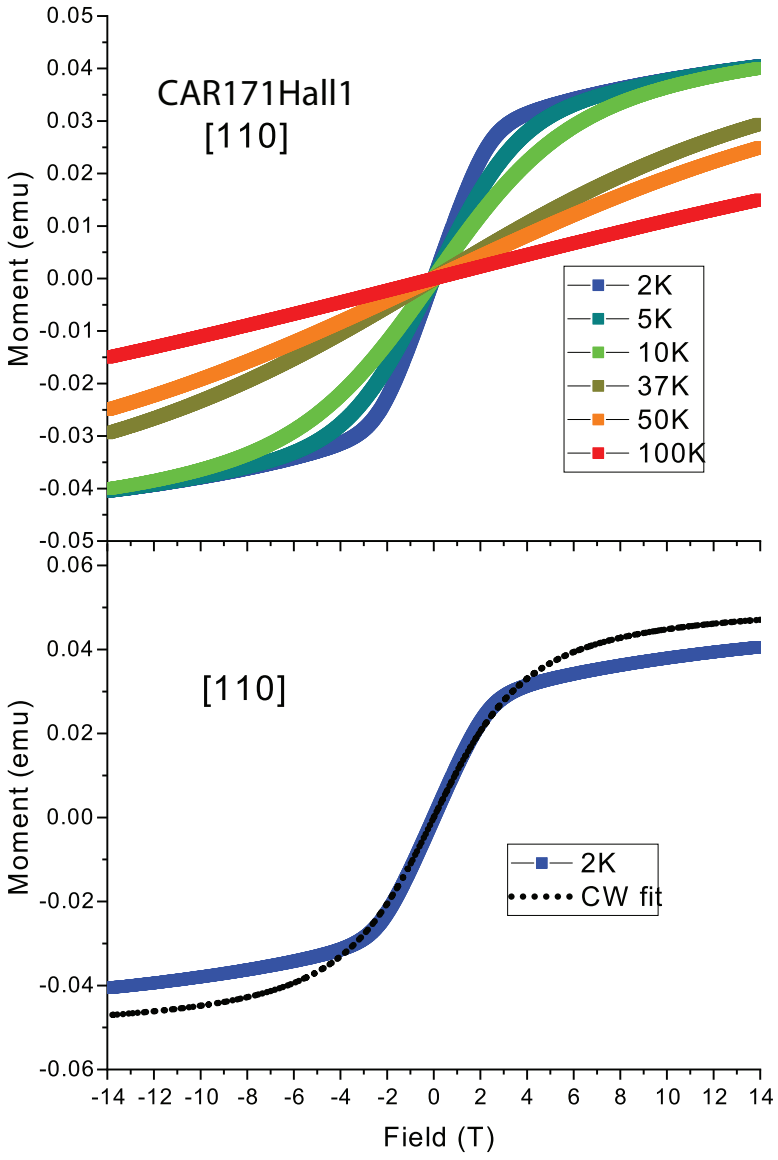

Figure 3.5: a) Field sweep of magnetization for the [110] direction at various temperatures. b) Curie-Weiss paramagnetism fit for sample at 2K, shifted by $\Theta = 9K$. Deviation between CW fit and 2K data increases as field increases and temperature decreases which is indicative of the strong AFM perturbations near the saturated paramagnetic state.

Outside the high-field deviation from paramagnetic saturation, HoPtBi is a textbook example of a paramagnet with no magnetic-field induced transitions, no temperature induced transitions, and which follows the Curie-Weiss behavior with AFM perturbations. It is however surprising how well HoPtBi matches CW paramagnetism up to the field scale of $k_B T = g\mu_B B$, most paramagnets depart from this relationship well before this point is reached, as this corresponds to saturation of the microscopic moments at relatively low field. In HoPtBi the saturation point is approached well below 14T, and even well above this point HoPtBi does not order, which is unusual compared to associated materials however large-J RPdBi carry some promisingly similar candidates [13]

3.3.3 Torque Magnetometry

In order to better understand the anisotropy of the magnetic state torque magnetometry was conducted on HoPtBi in two complementary orientations. These measurements were done by Halyna Hodovanets, to whom I am grateful for both the work and associated discussion of results. A C_4-symmetry sweep was conducted along the $\{001\}$ rotation plane and a C_2 symmetry sweep was conducted along the $\{01\bar{1}\}$ plane. The C_4 sweep maps out asymmetry between the [100] and $[1\bar{1}0]$ orientations, while the C_2 sweep maps [111], [100] and [111], [110] asymmetry.

For both $\{001\}$ and $\{110\}$ sweeps at low applied fields there is a small $Sin(2\theta)$ moment contribution, which is identical even once the sample has been rotated through 45°. The origin of this signal isn't clear and may require further investiga-

tion. At higher fields a strong anisotropic character arises that is centered along the high symmetry orientations.

The {001} field sweep is higher symmetry than the {110} field sweep, however it never crosses the expected easy axis of the expected AFM interactions, [111]. The closest projected direction is [110] which assumes the role of attractor along the manifold of rotation. There is an anomalous $Sin(2\theta)$ which we cannot explain given the cubic symmetries of the material. Absent this $Sin(2\theta)$ the signal at $1T$ appears isotropic indicating that HoPtBi is well within the isotropic paramagnetic state. As field is increased a C_4 signal begins to develop at $6T$, and overwhelms the $Sin(2\theta)$ signal at $8T$. This roughly corresponds to the saturated paramagnetic regime as seen in magnetization. Take special note that the data is normalized by applied field H, so the

The C_4 symmetry signal indicates that the [100] direction is the hard axis and the [110] direction is the easy axis for this rotation. Torque moves continuously through the easy axis, which acts as an attractor, however while moving through the hard axis a sudden 'flip' will occur as torque reorients to match the new closest easy axis. The result is an asymmetric, near-sawtooth waveform that matches our expectations for the C_4 symmetric system with the [110] being the projected easy axis (figure 3.6 dashed line).

The 110 field sweep is slightly more complicated. For $0 - 55°$ and $125 - 180°$ (modulo 180°), the angles between [100] and [111], the same hard-easy axis asymmetry corresponding to a moment pinned in the [111] direction exists. However for $55 - 125°$ (modulo 180°) corresponding to rotation from [111] into the [110]

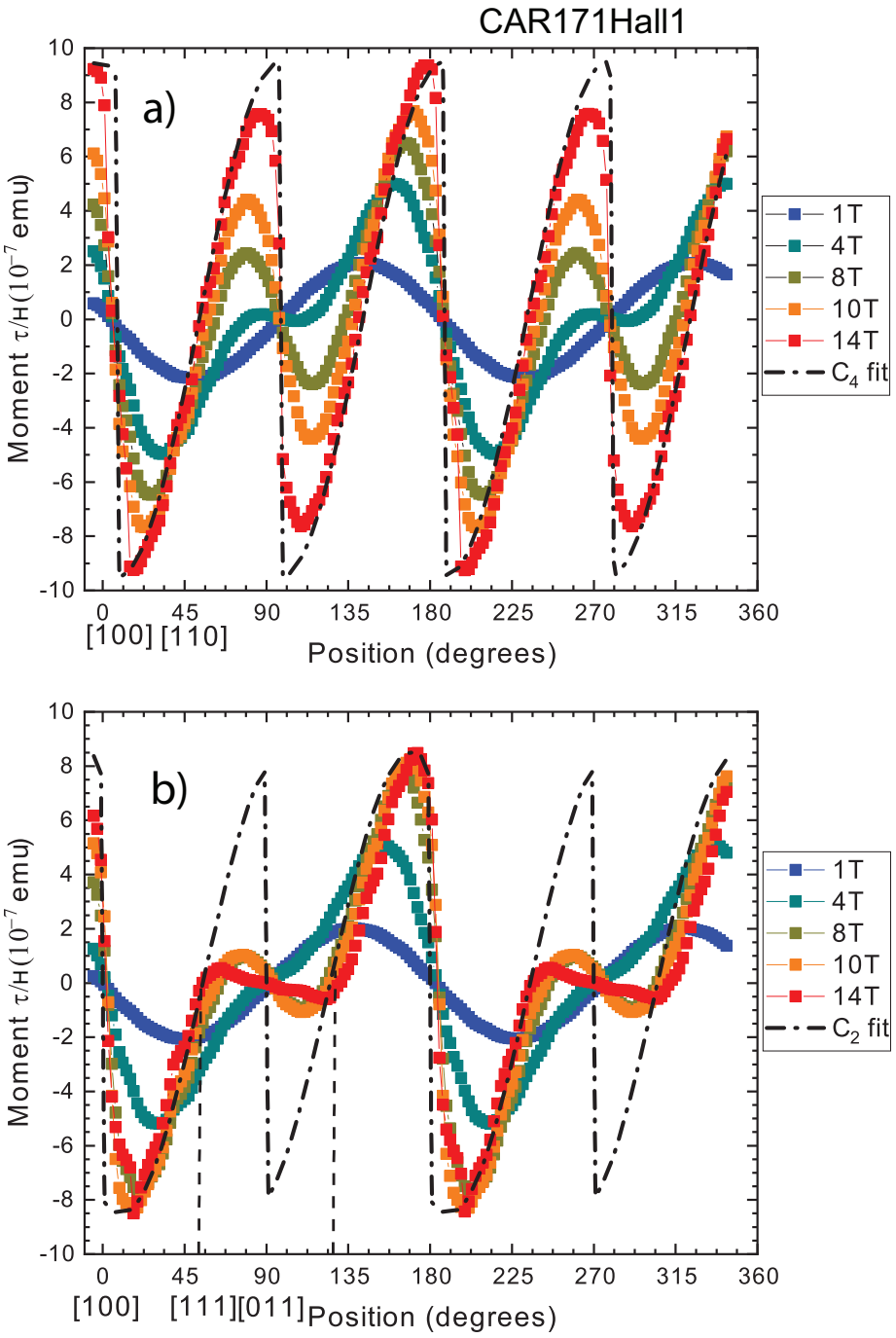

Figure 3.6: Torque divided by field along high symmetry rotations. a) Torque/H for the {001} rotation at various fields. A model for a moment pinned to [111] is presented (dot dashed line). b) Torque/H for the $\{01\bar{1}\}$ rotation at various fields. A model for a moment pinned to [111] is presented (dot dashed line). the [111] and $[\bar{1}11]$ are marked by a dashed line (55° and 125°). Note that the model vastly overpredicts torque between the [111] and [110] orientations.

direction the response is much smaller, indicating that the moment is not as strongly pinned for field rotated into this direction (figure 3.6). It isn't immediately clear why the [100] direction is a harder axis than the [110] direction, and this phenomenon might be worth further study.

3.4 Conclusions

Composition, physical structure, and magnetic ordering were considered for the HoPtBi compound. HoPtBi is found to be a $F\bar{4}3m$ cubic compound as reported when grown according to the self-flux method described in section 3.1.

The magnetic state for HoPtBi is found to be a low-temperature and low-field conventional AFM by neutron diffraction. At higher temperatures and fields the AFM order is suppressed and a paramagnetic regime exists for high-temperatures. At very high fields the compound still appears paramagnetic, however significant magnetic anisotropy begins to develop. This anisotropy isn't associated with any magnetic transitions or apparent ordering, suggesting it is the result of magnetic interactions asserting themselves at the highly-polarized regime outside of conventional Curie-Weiss paramagnetic description. We find that the [100] direction in particular is a hard axis, with significant torque associated with rotation into this direction. The [111] direction is the apparent easy axis as expected given the AFM order at low field, however the [110] direction is a softer magnetic axis than expected, deviating from the torque expected for a moment pinned specifically to the [111] direction.

Chapter 4: Weyl-like Transport in HoPtBi

The Weyl Hamiltonian discussed in section 1.1.2 has numerous ramifications for the electric transport properties for any Weyl semimetals. Unfortunately these identifying properties occupy a measured parameter with a number of other complicating transport effects. This makes experimental transport measurements a complicated affair of deducing and analyzing various contributions in order to make a reasonable statement about whether a particular signature is a result of Weyl Fermiology.

4.1 Chiral Anomaly

The most widespread signature of a Weyl semimetal is the chiral anomaly. The chiral anomaly occurs when a system has two Weyl points of opposite character coalligned with both an electric and magnetic field. In reciprocal space the Weyl point has the character of a magnetic monopole, so the presence of the combined electric and magnetic fields will bias carriers into one pocket and out of the other. The result is a non-symmetric contribution of charges, since this bias is coalligned with $\vec{E}$ in $\vec{k}$ space the result is a spontaneous additional current of spin-textured charges. The primary result of this is the creation of a negative magnetoresistance

if $\vec{B} \parallel \vec{E}$. In the event that $\vec{B} \perp \vec{E}$ there is no contribution from this effect, leading to an additional longitudinal conductivity component.

In addition to the negative magnetoresistance the chiral anomaly has another major ramification. Due to the topologically protected nature of Weyl points in condensed matter systems there must always be a surface state that connects two opposite-chirality Weyl nodes. In the event of chiral anomaly where one of these nodes is biased with a higher chemical potential, this surface state must be at least partially occupied. The result can be directly observed by means of ARPES or Photo Emission Spectroscopy. This measurement has been accomplished for certain materials, [11] [27] however it is beyond the scale of this dissertation to study this in HoPtBi.

Chris Eckberg measured samples I provided for longitudinal MR ρ_{xx} of HoPtBi in a He3 insert option in a custom dewar capable of reaching $18T$. Field and current were aligned along the [001] crystalline axis of a sample shaped into a bar with approximate dimensions of $1000\mu m \times 400\mu m \times 100\mu m$. A small region of positive MR exists below $0.1T$, however at $1.5K$ there is a significant region of negative MR beginning at $0.2T$ and spanning up to $12T$. The negative magnetoresistance effect is largest at $2T$, other features explored in subsequent sections will center around this field at base temperature as well (sections 4.2 and 5.3). As temperature is increased the negative magnetoresistance is both reduced in magnitude and deflected to higher field, disappearing almost entirely around $20K$. For all temperatures up to $10K$ high field MR is approximately linear.

At high fields ($6T$ and above for base temperature) a strong $f = 70T$ Shub-

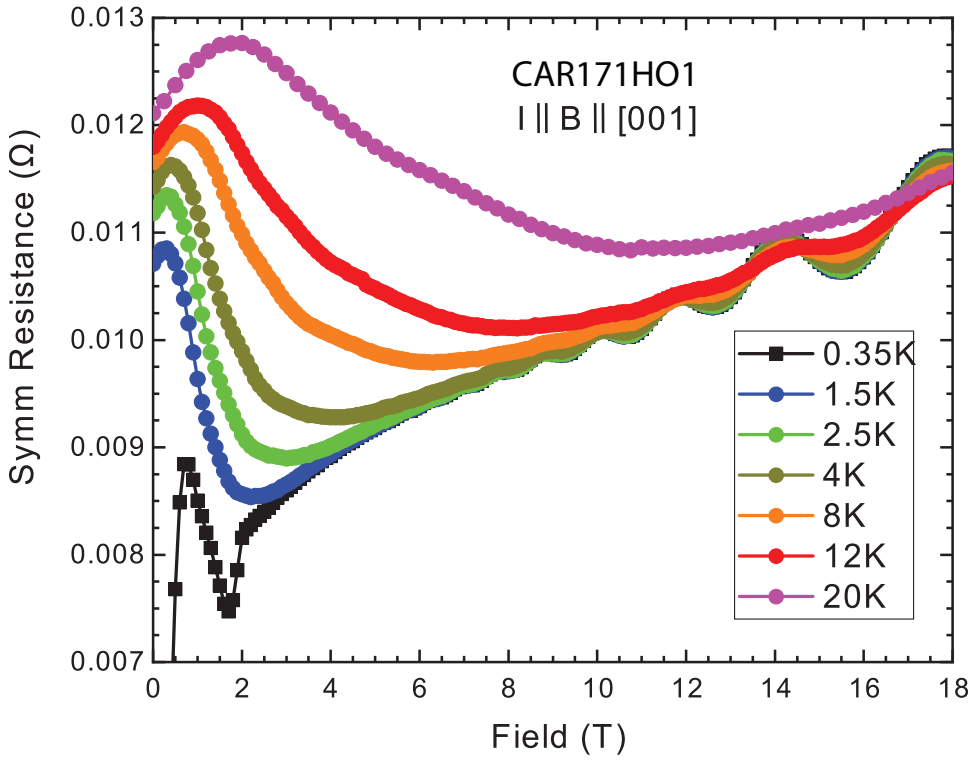

Figure 4.1: Resistance values for a sample measured in a He3 chamber with $\vec{B} \parallel \vec{I} \parallel [001]$. A significant region of negative MR is visible extending up to $12T$. As temperature increases the negative magnetoresistance signal diminishes until it is mostly gone by $20K$. Note that for the lowest temperature $0.35K$ fields below $2T$ correspond to the AFM ordered state, explaining the multiple sharp drops in resistivity.

nikov de Haas signal is visible. Discussion of SdH oscillations will be more deeply considered in section (5.2)

I conducted fixed-field rotation measurements in the 14T PPMS system at various temperatures in order to track the angular dependence of the negative magnetoresistance effect. We find that the negative magnetoresistance is only present in a small angular region around (10°) from $\vec{B} \parallel \vec{I}$. Also visible at $2K$ is a significant, non-$Cos(2\theta)$ like anisotropy. The 'butterfly' form of the anisotropy has distinct peaks near high symmetry directions, such as the [011] direction. As temperature is increased the negative magnetoresistance signal narrows in angular region as well as decreasing in magnitude. At $50K$ the negative magnetoresistance signal is totally gone, as is the apparent 'butterfly' anisotropy that appears aligned with the crystalline symmetries. A significant $Cos(\theta)$-like signal remains that depends on the angle between $\vec{B}$ and $\vec{I}$, indicating that even at $50K$ the angle between $\vec{B}$ and $\vec{E}$ is a significant parameter in this system.

4.2 Anomalous Hall Effect

As overviewed in section 1.1.4, well-formed Weyl semimetals are expected to have an anomalous contribution to the asymmetric Hall Effect. The form of this contribution is unclear, however it has been argued that the contribution can be a semi-quantized form directly corresponding to the distance between Weyl points in reciprocal space. [16] In GdPtBi application of Field results in an increase in the Hall Angle at $2.5T$, which is argued to be an expression of field-stabilized Weyl

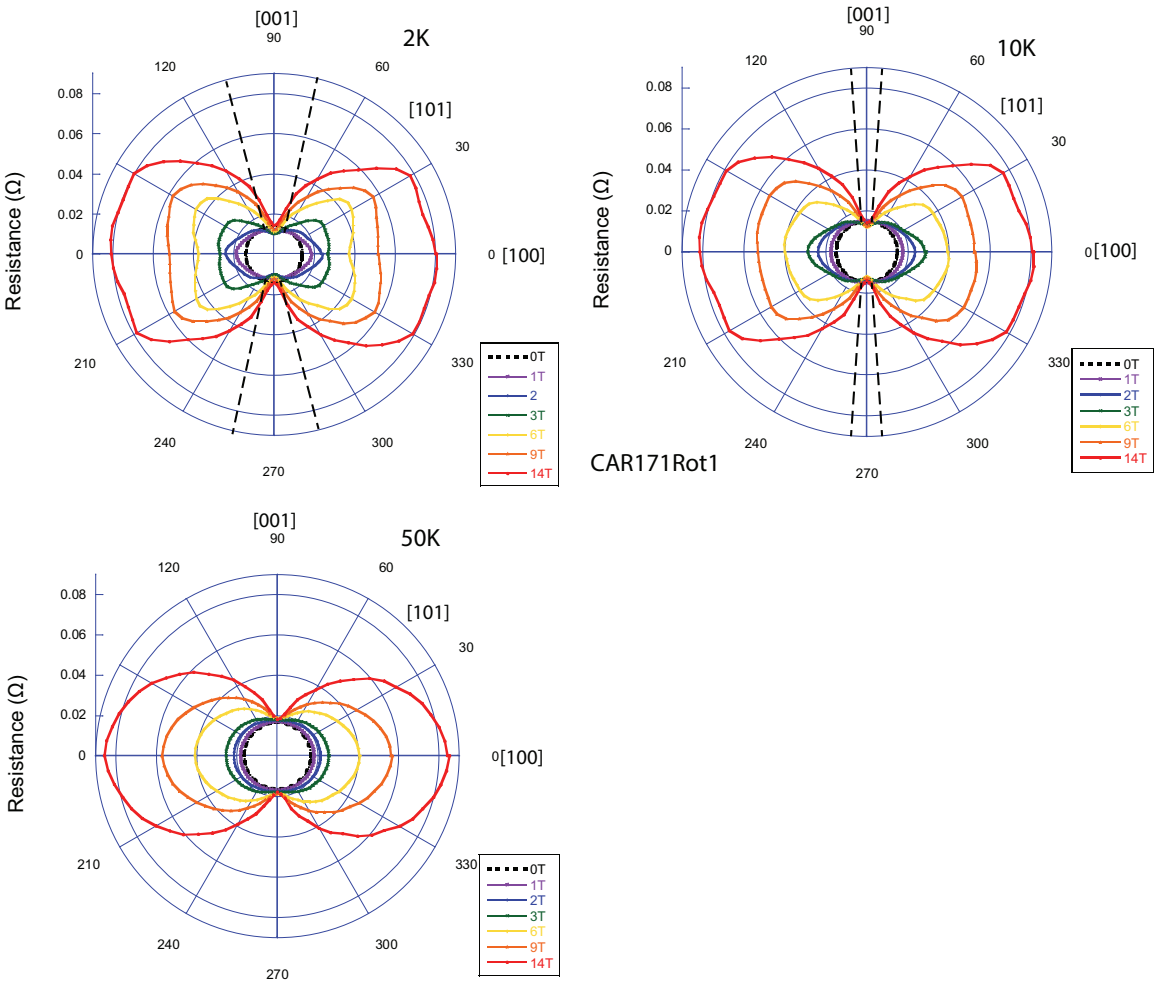

Figure 4.2: Rotation measurements at fixed field for multiple temperatures. At $2K$ a negative MR signal is visible in a roughly 10° window around the [001] direction $\vec{B} \parallel \vec{E}$ (dotted lines are presented as a guide to the eye). Also visible is a 'butterfly shape' character of non-$Cos(2\theta)$ like behavior that is attributed to anisotropic MR character dependent on underlying crystalline symmetry. As temperature is increased to $10K$ the negative magnetoresistance persists, but the window of available angles narrows considerably. By $50K$ the negative magnetoresistance is gone, as well as the butterfly effect leaving only a $Cos(2\theta)$-like dependence on the angle between $\vec{B}$ and $\vec{E}$.

points. [12] As temperature is increased this AHE effect decreases in magnitude until it is effectively gone at roughly $60K$.

We found a similar AHE effect in HoPtBi, however we found the AHE contribution was significantly orientation and temperature dependent in a way not reported for GdPtBi. We break down the results as a function of temperature (at two fixed orientations) and then by a continuous rotation in the following sections.

4.2.1 AHE Temperature Dependence

4.2.1.1 [100] AHE

I collected ρ_{xx} and ρ_{yx} data in the four-wire longitudinal and Hall configurations with $\vec{E}$ applied along the [001] direction. Measurements were done as a function of field up to $7.5T$ and at various fixed temperatures in the $3-50K$ range. These measurements preceded a similar, but more expansive measurement with field oriented along the [111] magnetization easy axis. Both longitudinal and Hall resistivity are presented in figs. 4.3 and 4.7.

Before calculating Hall angle it is instructive to look at the individual resistivities and see how increasing field affects the phenomenology in this orientation up to moderate fields. Longitudinal resistance is presented with vertical adjustment in fig. 4.3. At $2K$ and fields below $1.2T$ a quadratic dependence in field is apparent. At approximately $2T$ there is a downturn in resistance (marked by an arrow, figure 4.3) that separates the low-field quadratic region from a region of linear MR behavior up to high field. As temperature is increased the quadratic low field behavior

is extended to higher field and the downturn region that separates linear high field region is smeared out and increased in field.

Hall resistivity data is presented in 4.3 as well as carrier concentration calculated from ρ_{yx} data in figure 4.5. At $3K$ ρ_{yx} begins linear but has a significant negative deflection at $2T$. At higher fields ρ_{yx} increases again such that a linear extrapolation at high field passes through the origin, suggesting that the negative deflection is a localized decrease in Hall resistivity. Carrier concentration data reflects this deflection as a sharp increase in hole carriers of $\approx 40\%$ centered on $2T$. As temperature was increased the deflection in ρ_{yx} as well as the associated increase in hole concentration get pushed to higher fields. For $50K$ the increase in CC seems to be pushed past $7.5T$ used in this measurement, however the tail end of the increase can be seen in high fields.

Using the longitudinal and Hall resistivity I calculated a composite measurement of Hall angle according to section 2.5.2.3 and results are presented in fig. 4.5. Data collected at $50K$ was scaled and subtracted from other temperatures to produce a measurement of the anomalous Hall angle value, also presented. The results appear qualitatively similar to measurements conducted on GdPtBi, [12] however there are some crucial differences. First of all the peak of the AHA value in HoPtBi is strongly affected by temperature, with increasing temperature causing an increase in peak AHA field value and a moderate decrease in amplitude. In GdPtBi an increase in temperature causes the AHA to diminish in magnitude, however it does not significantly change the peak field value. Additionally the AHA in these measurements is negative instead of the positive AHA in GdPtBi. [12] As we will see in

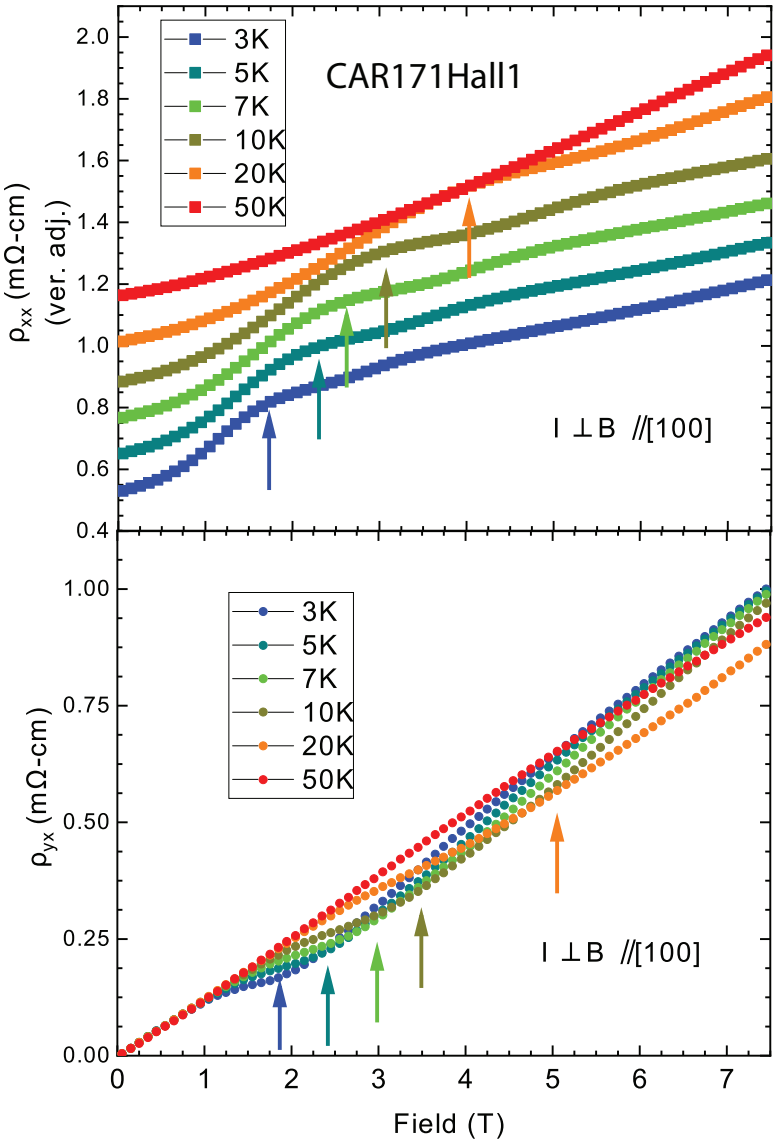

Figure 4.3: Resistivity values as-measured for the $\vec{B} \parallel [100]$ configuration. Longitudinal resistivity is presented as the resistivity tensor value ρ_{xx} and the Hall resistivity is presented as ρ_{yx}. Major features for each measurement are marked by colored arrows. Longitudinal resistance appears to have an additional minor feature at higher field, but this does not clearly map to features in Hall Angle.

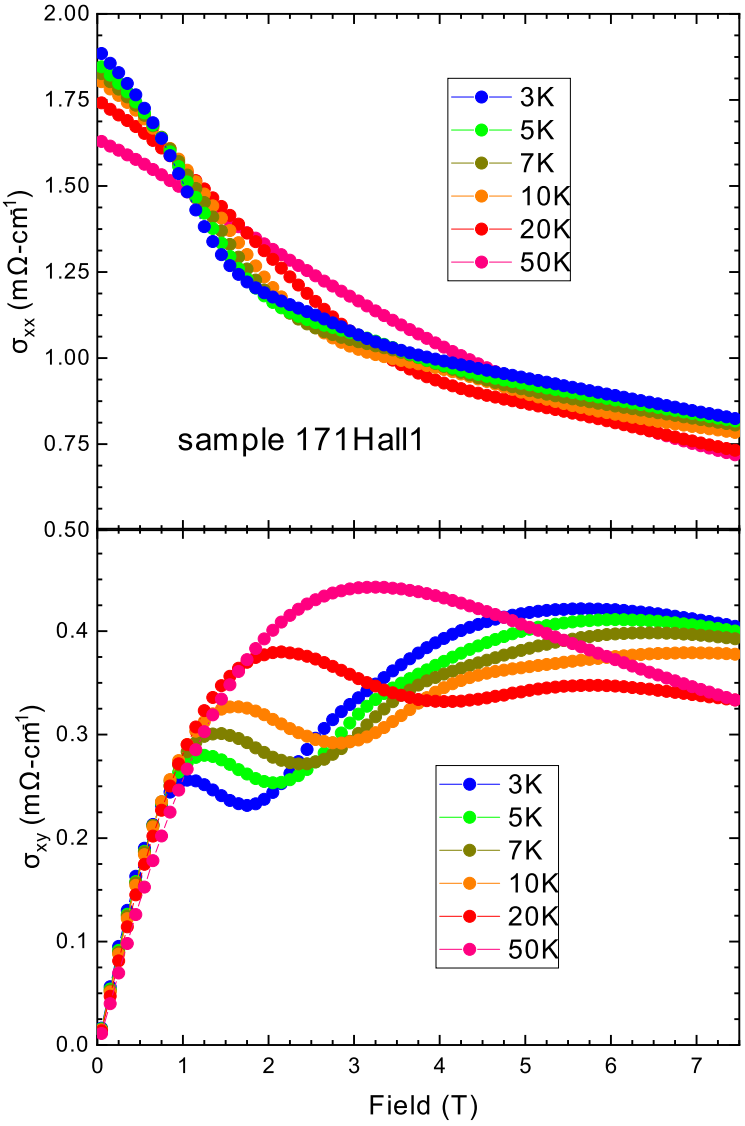

Figure 4.4: Conductivity values as-measured for the $\vec{B} \parallel [100]$ configuration. Longitudinal conductivity is presented as the conductivity tensor value σ_{xx} and the transverse conductivity is presented as σ_{xy}.

a following section this negative AHA value is unique to this specific magnetic field orientation in HoPtBi, a feature which will help motivate measurement of resistive anisotropy covered in ch. 5 of this dissertation.

4.2.1.2 [111] AHE

ρ_{xx} and ρ_{yx} measurements were also conducted for magnetic field along [111] and current along $[1\bar{1}0]$. Measurements were conducted in a similar manner to the [100] oriented measurement, but were conducted on a greater temperature range $(2 - 300K)$ since [111] is the easy magnetic axis of the material.

Longitudinal and Hall resistivity is presented in fig. 4.3. The low-field quadratic region found in the [100] orientation extends to the [111] orientation as well. At base temperature and $2T$ longitudinal MR has a small negative deflection instead of the positive kink visible in the [100] oriented data (marked by a colored arrow). As temperature increases this region is deflected upwards and diffused similar to the positive kink in the previous section. Correspondingly ρ_{yx} has a small region of non-linearity in the $2T$ region (marked by a black bar).

Hall angle was calculated according to section 2.5.2.3. A deviation in Hall angle is readily apparent in data sets up to $60K$. The $60K$ Hall angle data was used as the representative set for the normal state, and AHA results were calculated by subtracting a $60K$ data set scaled according to the $7.5T$ value from each corresponding temperature. Hall angle in this orientation is large and positive, matching the reported behavior for GdPtBi. [12] Once again as temperature is increased from

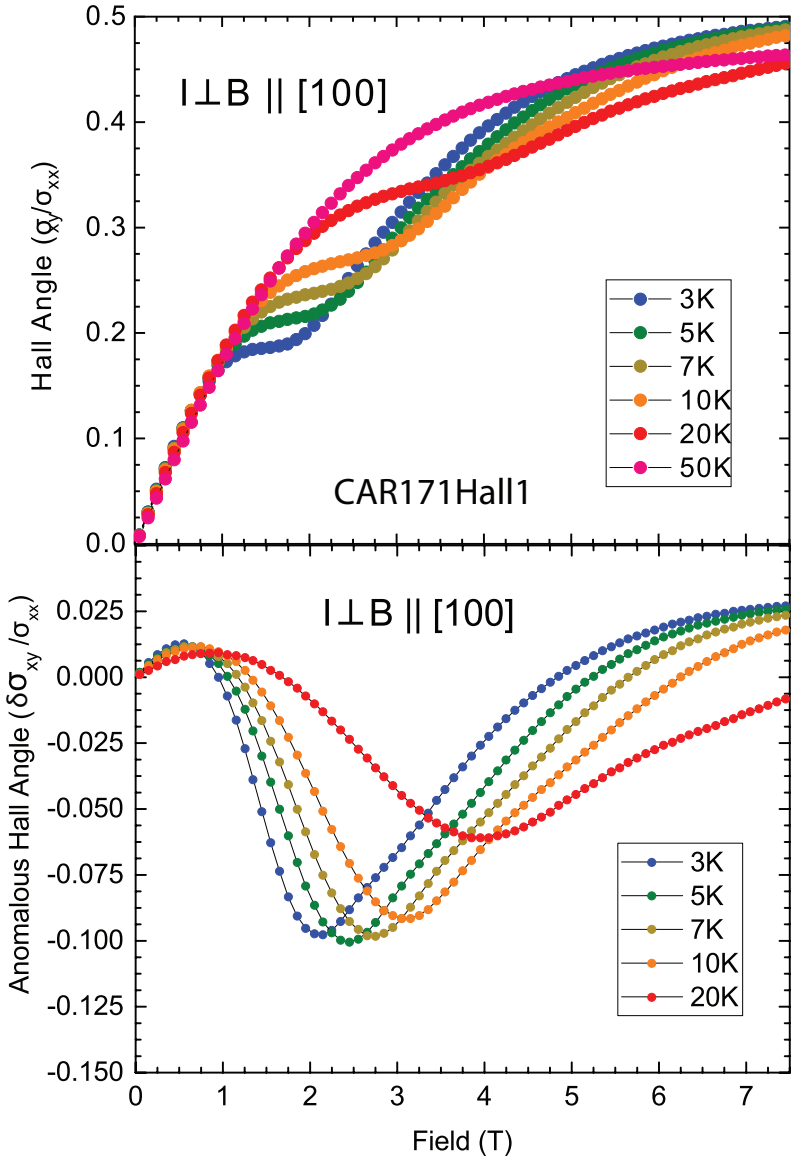

Figure 4.5: Hall Angle evaluated for the [100] orientation. Data was collected across multiple temperatures in the $3-50K$ range and up to $7.5T$ in field sweep. Anomalous Hall Angle is calculated by subtracting $50K$ HA data from lower temperatures, creating a profile of the AHA deflection. AHA magnitude is not significantly decreased by temperature up to $10K$, however the peak AHA value is deflected to higher fields as temperature is increased.

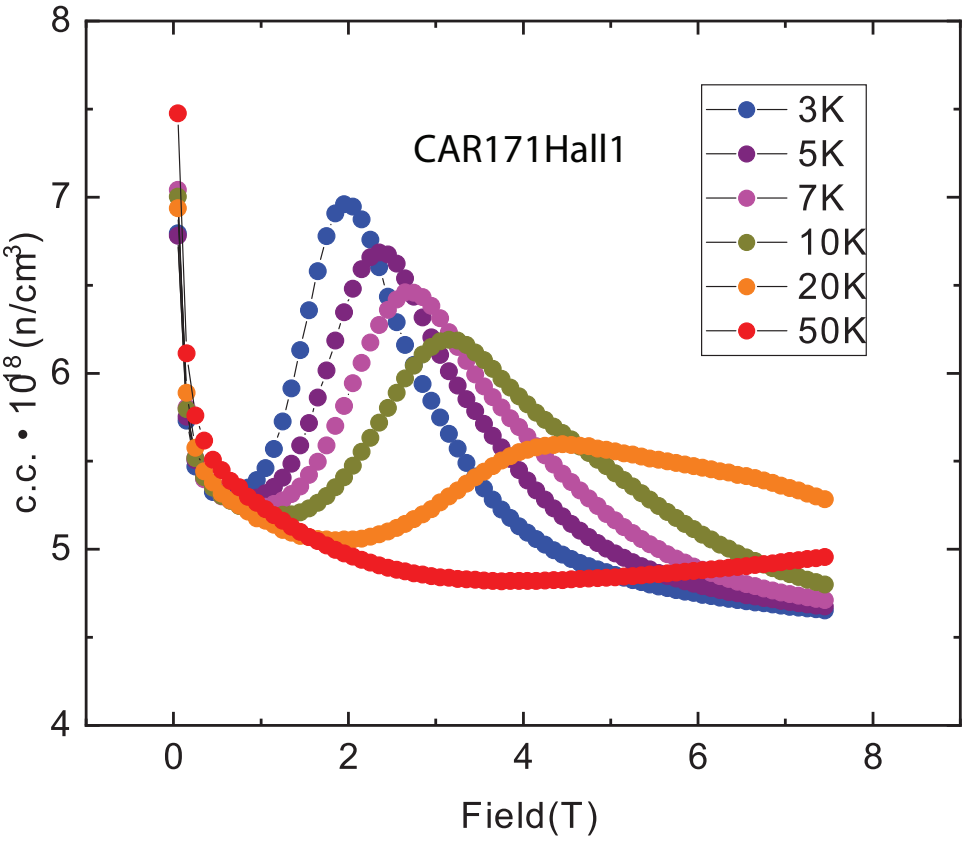

Figure 4.6: Carrier concentration evaluated for fields applied along $\vec{B} \parallel [100]$. Carriers are hole-like and in the roughly $5E18$ regime. The deflection in ρ_{yx} translates to a roughly 40% increase in c.c. at $3K$, a feature which deflects upwards in field as temperature increases, similar to features in ρ_{xx}.

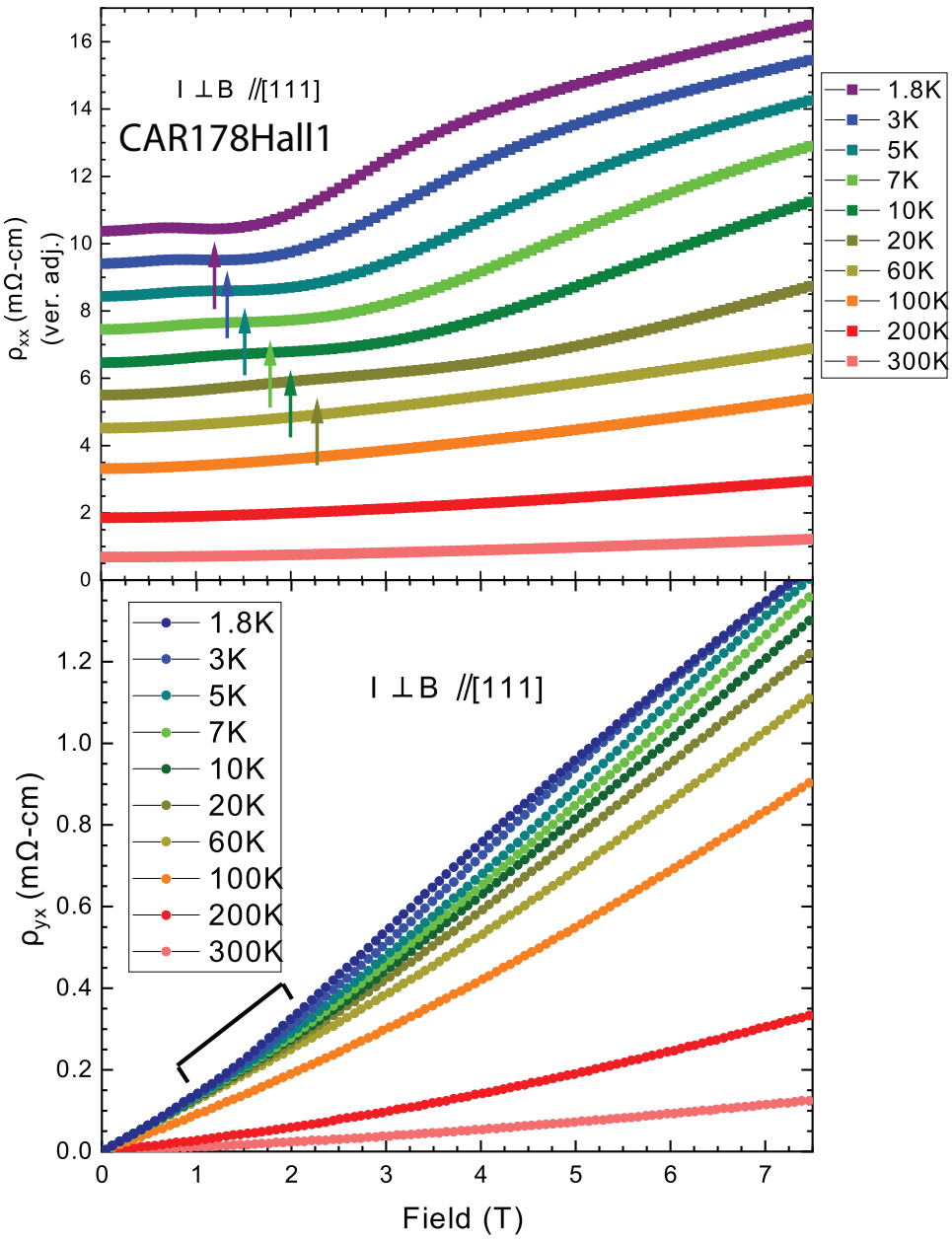

Figure 4.7: Resistivity values as-measured for the $\vec{B} \parallel [111]$ configuration. Longitudinal resistivity is presented as the resistivity tensor value ρ_{xx} and the Hall resistivity is presented as ρ_{yx}. Major features in ρ_{xx} are presented as colored arrows and in ρ_{yx} by a black bar.

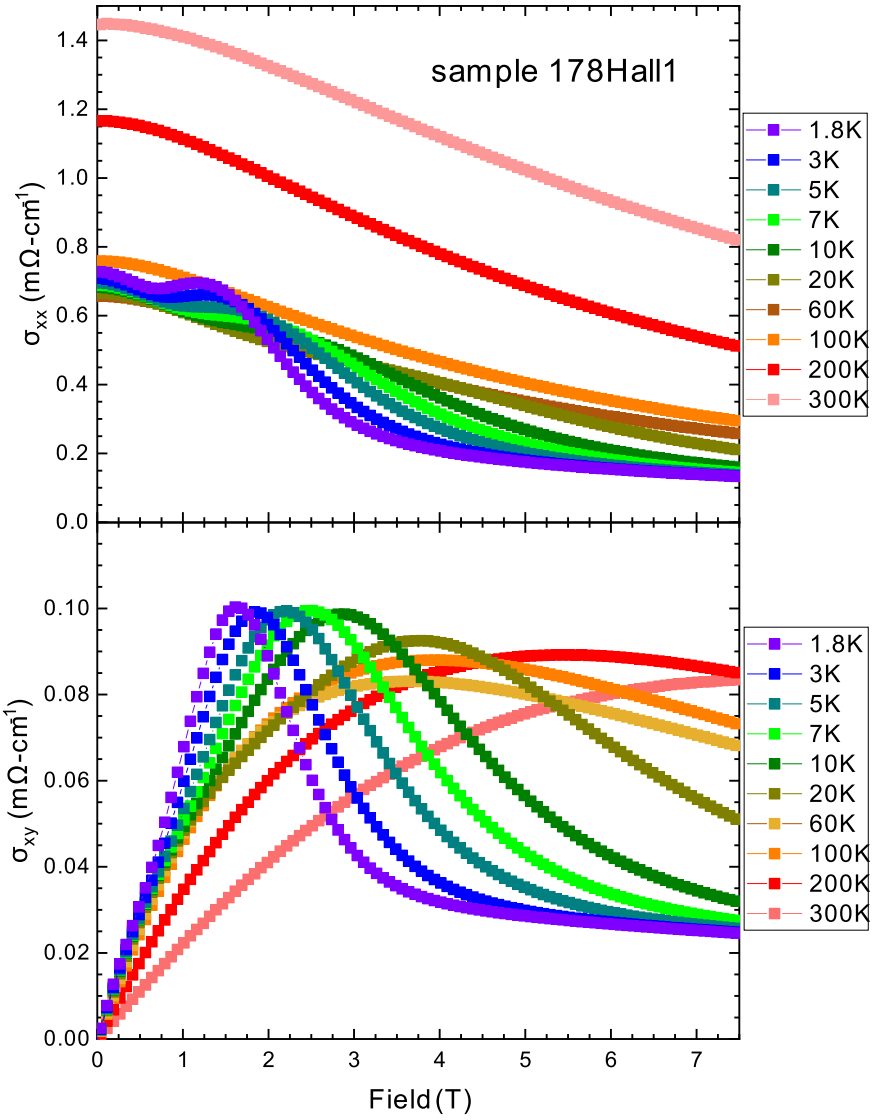

Figure 4.8: Conductivity values as-measured for the $\vec{B} \parallel [111]$ configuration. Longitudinal conductivity is presented as the conductivity tensor value σ_{xx} and the transverse conductivity is presented as σ_{xy}.

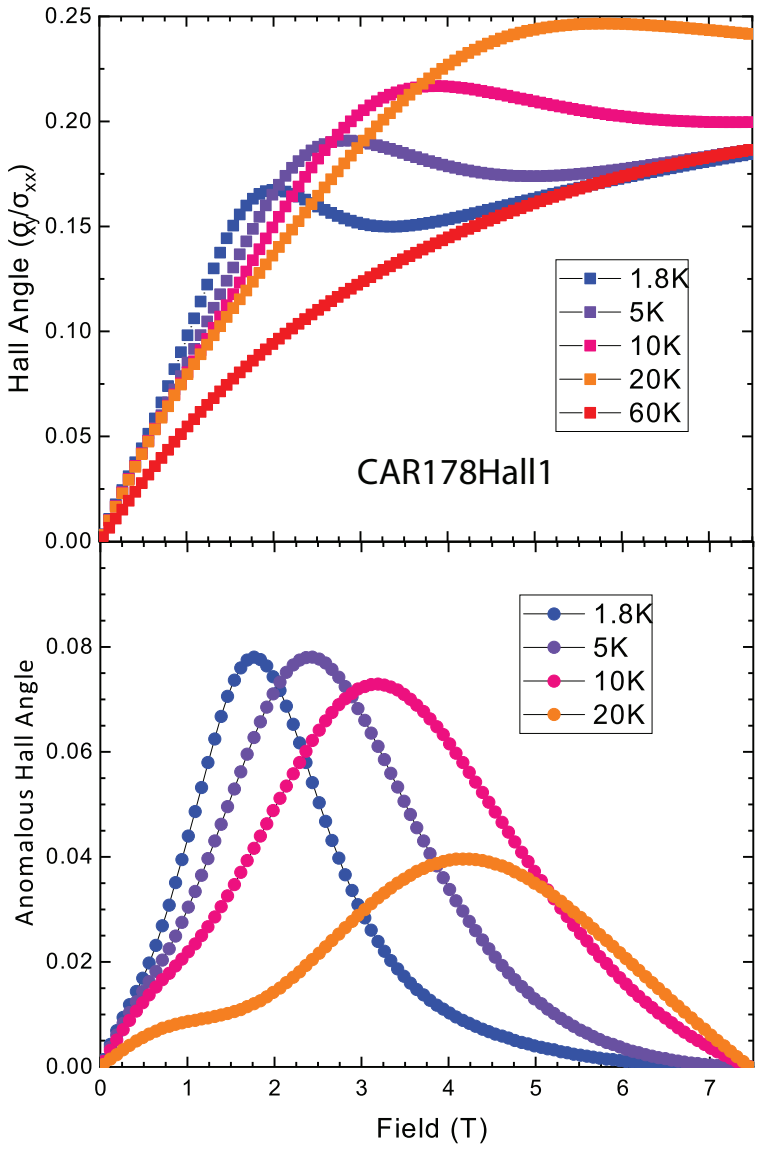

Figure 4.9: Hall Angle evaluated for the [111] orientation. Data was collected across multiple temperatures in the $1.8-60K$ range and up to $7.5T$ in field sweep. Anomalous Hall Angle is calculated by subtracting scaled $60K$ HA data from lower temperatures, creating a profile of the AHA deflection.

$1.8 - 10K$ the peak of the AHA effect is pushed upwards in field, however the magnitude of the AHA effect only begins to diminish at higher temperatures ($20K$). This is similar to the results found in the previous section, such that Hall Angle field onset is dependent on temperature.

4.2.2 AHE Orientation Dependence

Given the discrepancy between [100] and [111] oriented AHE signs we expanded the measurement of Hall Angle to arbitrary angles through measurement of ρ_{xx} and ρ_{yx} as field is rotated in the $\{001\}$ plane. This measurement allowed a continuous mapping of Hall Angle through the high symmetry directions of [100] and [110]. Take note: $\vec{B}$ is necessarily rotated into the plane of the sample leads for this measurement, which is not ideal for this type of measurement. ρ_{yx} was asymmetrized in order to remove any symmetric contribution, however as $\vec{B}$ enters the plane of the sample the asymmetric component we wish to observe will diminish and be overwhelmed by residual symmetric contributions. For this reason only data points through 70° are presented for ρ_{yx} and resulting calculations.

ρ_{xx} data at 2K is presented in figure 4.10. The low-field quadratic region is readily apparent for all orientations indicating the isotropic regime. Above $2T$ MR for different orientations begins to display orientation dependence. Above $\approx 3T$ the orientation dependence flips in character, a detail which will be more closely studied in ch 5 of this dissertation.

ρ_{yx} data is more complicated in this picture. We are interested in the Hall

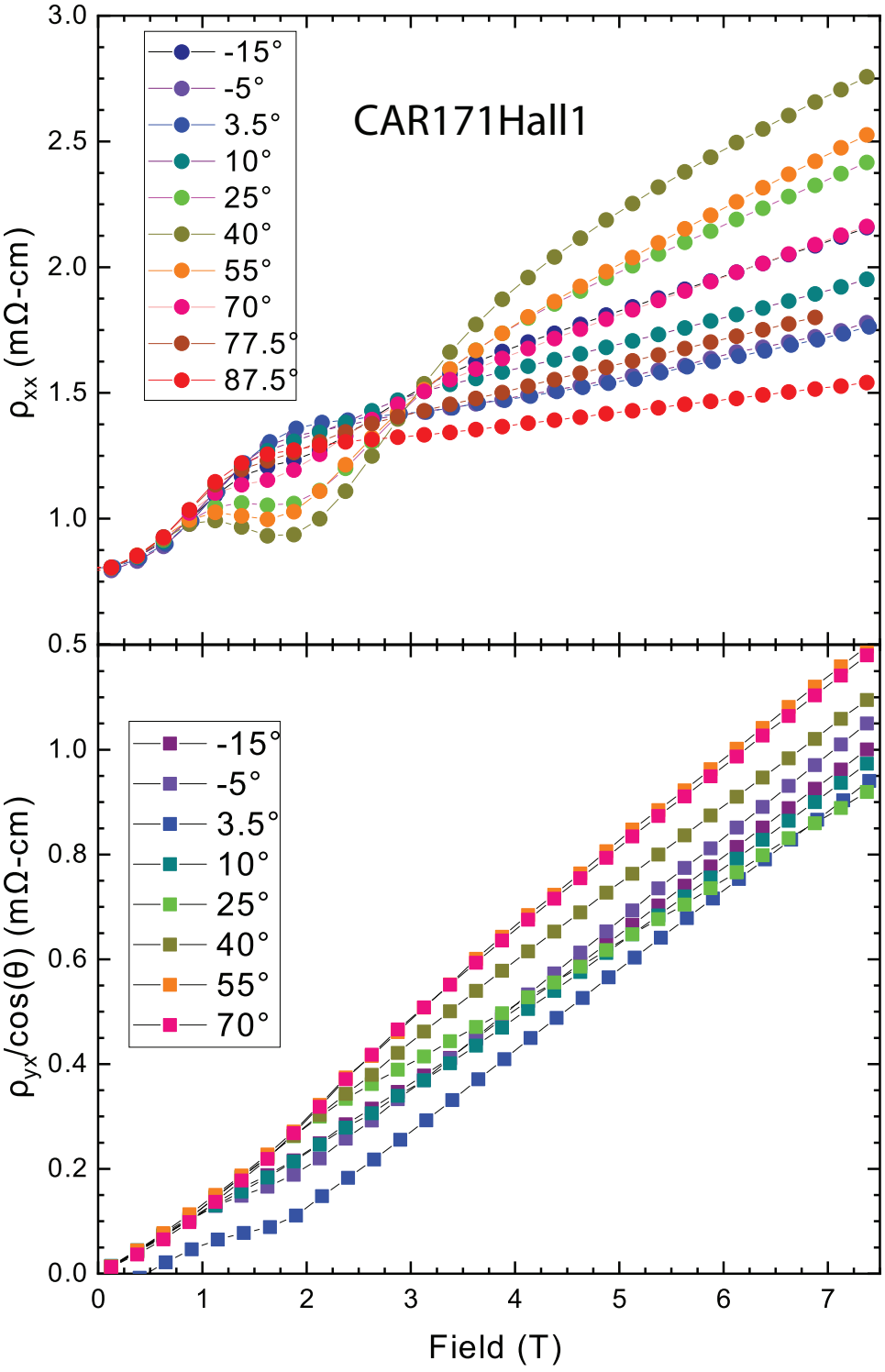

Figure 4.10: Longitudinal and Hall resistivity components as a function of field angle. 0° corresponds to $\vec{B} \parallel [100]$, 90° corresponds to $\vec{B} \parallel [010]$, and 45° corresponds to the intermediate $\vec{B} \parallel [110]$. Anisotropic MR is clearly visible in ρ_{xx}. High angles are omitted from the adjusted ρ_{yx} calculation due to error being significant compared to experimental signal.

response of the system as field is rotated relative to the crystalline axes of the system, however it is practically speaking impossible to reorient the leads between each measurement such that magnetic field is perpendicular to the contacts. For this reason ρ_{yx} will follow a $Cos(\theta)$ dependence. To counteract this we calculated $\rho_{yx}^{eff} = \rho_{yx}/Cos(\theta)$. For $\vec{B} \parallel [100]$ we find the same negative deflection of ρ_{yx}^{eff} we see in the [100] oriented measurement from section 4.1.1. As field is rotated through 45° ρ_{yx}^{eff} gets deflected upwards to reflect behavior similar to the [111] oriented measurement. Higher orientations corresponding to rotation into the [010] direction are omitted as noise dominates the ρ_{yx}^{eff} value.

Hall angle data is presented in figure 4.11. Once again we can see a characteristic change between the [100] and [110] orientations, confirming that the [100] anomalous Hall angle sign difference from section 4.2.1 and furthermore that the change in character is distinct to that high symmetry direction. The AHA sign flips around 12° back to positive through the [110] direction. The AHA sign flip cannot be confirmed at higher angles due to the limitations of rotation into the plane of the Hall measurement.

4.3 Conclusions

In this chapter we discussed a few signatures of a potential Weyl state. We discussed negative longitudinal magnetoresistance, which is a key signature of the chiral anomaly. We also discussed the anomalous Hall effect which is often tied to intrinsic Berry curvature in compounds. The phenomenological dependence on

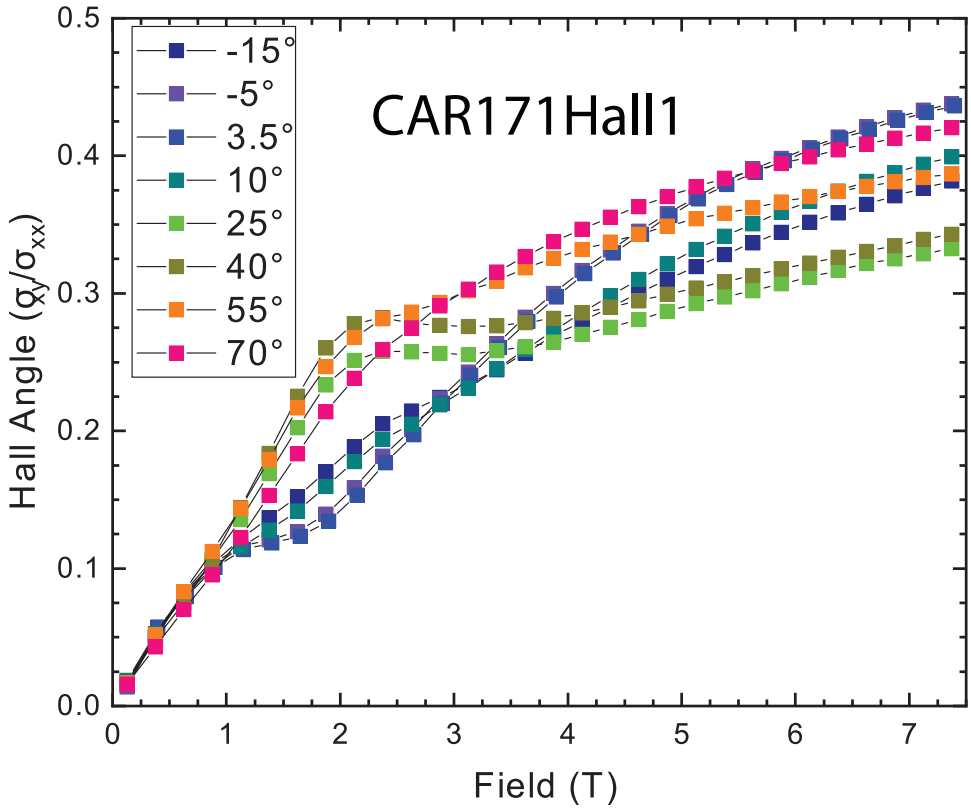

Figure 4.11: Hall Angle as a function of applied field angle. High-angle values (corresponding to $\vec{B} \parallel [010]$) are omitted due to high error sources in calculating ρ_{yx}^{eff}.

applied field orientation and temperature seem to be strong indicators that complex phenomenon might be occuring in HoPtBi's band structure.

Between the negative magnetoresistance signature of chiral anomaly and the anomalous Hall effect, HoPtBi appears to be a compound which begins with very typical semimetallic properties, but which has significant band distortion in the intermediate $2 - 8T$ field range. Furthermore there are several anisotropic magnetoresistance behaviors that became apparent during these measurements. The next chapter will expand on these AMR characteristics, and we will attempt to tie all of these behaviors into a single coherent explanation.

Chapter 5: Anisotropic Magnetoresistance in HoPtBi

5.1 Overview

Magnetoresistance is a complicated phenomenon with numerous causes and phenomenological results. In the simplest case resistance is dependent on the applied magnetic field as a result of deflections of charge carriers in a magnetic field. Magnetoresistance can be further complicated by magnetic ordering and domains, in which carriers passing from one magnetic domain into another deal with increased scattering at the boundary between. The study of anisotropic magnetoresistance (AMR) officially began in 1857 with the study of longitudinal and transverse magnetoresistance in purified Iron and Nickel by Professor William Thomson, later known as Lord Kelvin. [39] Nearly a century later this knowledge would be used to create magnetic reading elements for magnetophons, a precursor to more modern read/write elements. [40]

Magnetoresistance has historically been a crucial technology in miniaturization of computerized memory components. Prior to 1990 the read-write head for spinning disk hard drives was a single unit inductive coil, which had issues spatially resolving magnetic bits encoded in the disk media. The discovery of GMR allowed the creation of extremely sensitive and compact magnetic readers which miniaturized one of the

largest components of computers, paving the way for the realization of the modern home computer. The 2007 Nobel prize in Physics was granted to Albert Fert and Peter Grünberg jointly for their discovery of this mechanism. [41] [42] [43]

Beyond its historical importance in the modern technological age, anisotropic magnetoresistance is also vital for specialized highly accurate magnetic field detectors everywhere from scientific astronomical and geophysical applications as well as microscopic detectors for diagnoses of electrical components and beyond. The creation of AMR components alone constitutes a significant industry, therefore the discovery of an additional mechanism for AMR is worth investigating. [44] In this chapter we discuss AMR in a paramagnetic compound, which previous AMR mechanisms cannot explain. This property is likely driven purely by the electronic state, for which interaction with the magnetic field is mediated by exchange interaction with the RE f-electrons well removed from the Fermi surface.

In this chapter we will discuss the magnetic and Fermi surface properties of HoPtBi and how these relate to a novel anisotropic magnetoresistance (AMR) signal we see in this material. In section 5.2 we will discuss quantum oscillation measurements that probe the shape of the Fermi surface of HoPtBi under field. In section 5.3 we will discuss the AMR signal found in HoPtBi and draw parallels between the magnetic state and crucial aspects of the AMR signal. Section 5.4 is reserved for discussion and conclusions.

5.2 Shubnikov de-Haas Oscillations

Shubnikov de-Haas oscillations are a key tool to probe the Fermi surface of metals and semimetals. Oscillation frequency can be used to map the maximal orbit perpendicular to a given field orientation. One of the assumptions in quantum oscillation frequency analysis is that the Fermi surface is static under applied field and changing field orientation. [45] For most materials this is a valid premise, however in HoPtBi and associated high-J half-Heuslers, DFT calculations as well as investigation of other Fermi surface sensitive observables suggest that this may not be a safe assumption. In particular previous work on GdPtBi suggests that the number and location of Weyl nodes can be tuned by application and orientation of field, suggesting a strong field dependence for the Fermi surfaces of these materials. [12] Nevertheless Shubnikov de-Haas oscillations can still be used to glean insight, provided we keep in mind that the surface may be quite sensitive to field.

Samples of well-aligned HoPtBi were sent to the National High Magnetic Field Lab in Tallahassee, Florida. Samples were oriented such that current was applied along the [100] direction and field could be rotated from perpendicular to current and along the [010] direction (0°) to along the [100] direction, parallel to current (90°). This will be known as the longitudinal configuration. Take note that the 45° orientation corresponds to the [110] high symmetry direction.

Samples were rotated to fixed orientation between $0° - 90°$ and cooled below $700mK$. The magnet was quickly charged to $35T$, then relaxed slowly to $0T$ constituting a down-field sweep measurement. Measurements were taken in alternating

current mode with a four wire longitudinal setup in order to extract resistance data. Frequencies were extracted from resistance data using a combination of Fast Fourier Transform (FFT) and a phenomenological fit function on the second derivative of the raw data. Analysis of low-frequency quantum oscillation data is an involved process that is better reserved for a deep discussion, details and justification for the methods used can be found in Appendix A.

Samples are rotated along the high symmetry [001] axis, with current along the [010] direction and therefore in the plane of rotation. The non-oscillating components of the high-field ρ_{xx} values in this measurement match the phenomenology observed in the 18T measurements, but extended to higher field. ρ_{xx} is linear or sub-linear non-saturating for all observed orientations at sufficiently high fields ($> 20T$). Take note that resistance decreases as field is rotated into the direction of current. The pronounced resistive anisotropy resulting from crystalline orientation is superimposed over this decrease in ρ_{xx} associated with rotation into the longitudinal orientation, as a result the greatest MR direction is along 26° at least up to $35T$. (figure 5.1)

Large oscillations become apparent in all orientations above 15T, taking the second derivative of the data allows oscillations to be isolated down to 10T, giving a $1/B$ range of $.07T^{-1}$. As discussed in Appendix A the small $1/B$ window combined with the roughly exponential growth in oscillatory signal presents a problem for conventional FFT analysis. For this reason in addition to conventional FFT approach to analyzing frequency we used a phenomenological fit approach, the goal of which was to isolate the frequency of the signal from it's envelope function while

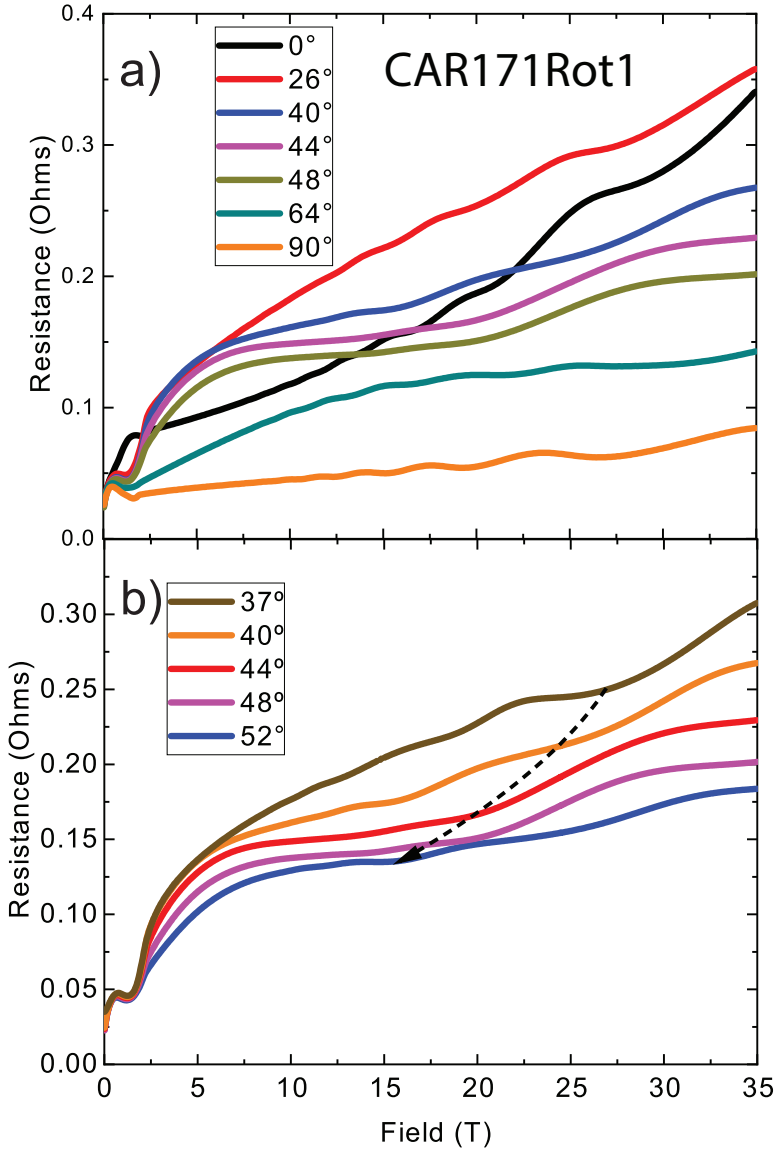

Figure 5.1: Raw resistance data collected at NHMFL in Tallahasee, FL. a) Data collected at chosen orientations representing the breadth of measurements taken from $0°, [100]$ to $90°, [010]$. b) Select data sets closest to $45°, [110]$ showing the evolution of the quantum oscillation behavior nearest to the sensitive [110] orientation. The dotted black arrow shows the change in phase apparent as the sample is rotated a just over 15° through the [110] orientation.

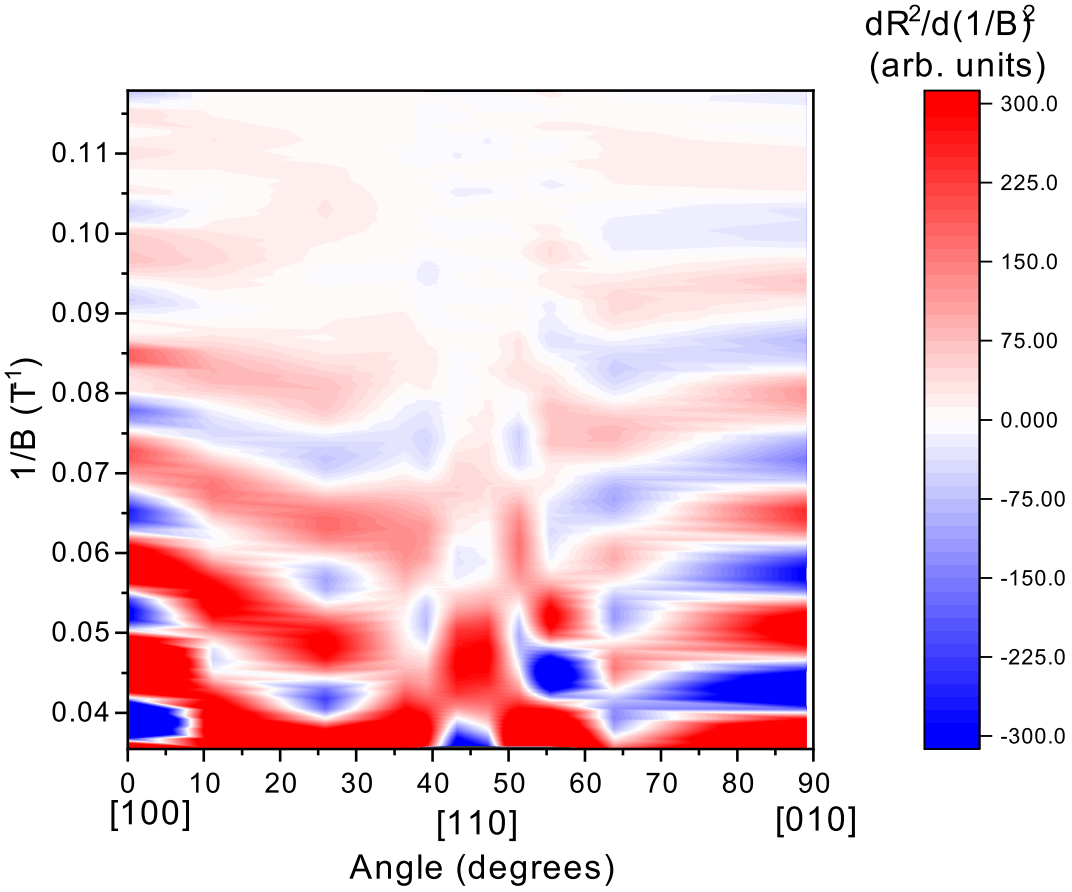

Figure 5.2: 2nd derivative of resistance signal presented as a contour map in T and $1/B$. Phase shift and frequency shift are both clearly visible, particularly near 45° corresponding to the [110] crystalline orientation, indicating a sharp change in Fermi surface cross-section when field is oriented along this direction.

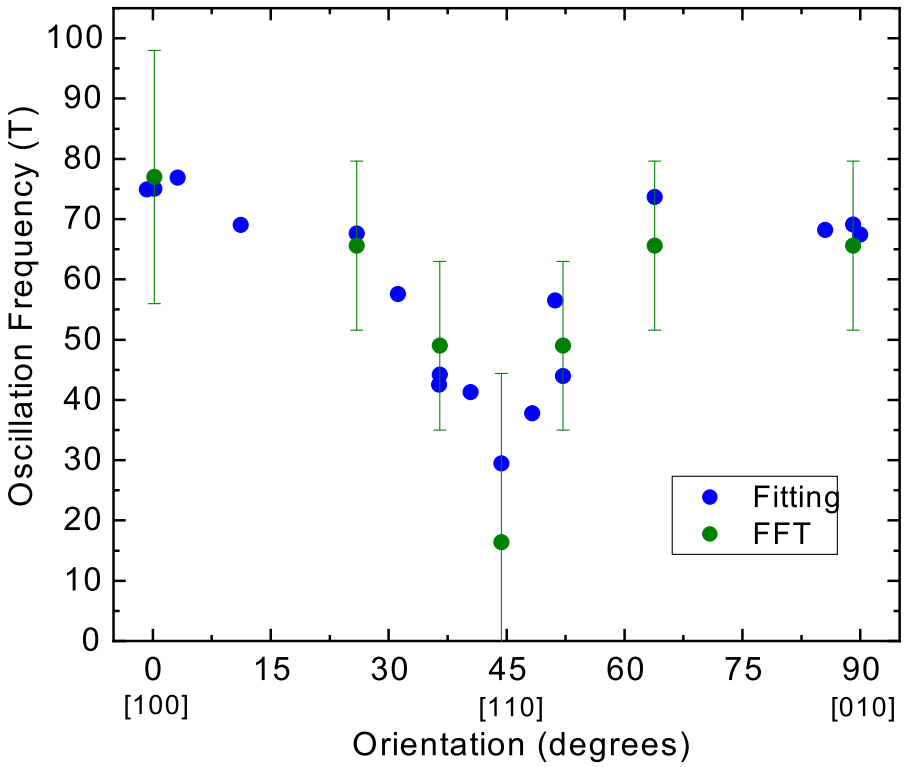

Figure 5.3: Oscillation frequency mapped against orientation. Frequency was determined by both FFT (green) and by a fitting function (blue). Error bars reflect the FWHM of the FFT spectrum. Description of results and justification of fitting functions can be found in Appendix A.

sidestepping the numerous sources of error introduced by FFT on low frequency signals. (Appendix A)

Frequency values for single pocket phenomenological fits as well as FFT and the associated full width half-maximum (FWHM) are presented in figure 5.3. A frequency of roughly 70T is present for orientations within roughly $\pm 30^{\circ}$ of the [100] direction. Close to the [110] orientation the frequency sharply drops to 35T, indicating a much smaller Fermi surface cross-section in the [110] plane.

If the Fermi surface is a static construct as high field is rotated relative to the sample then this presents a difficult picture where the surface is heavily distorted, such that the maximal circumference of the [110] measurement is half that of the [100] measurement. Because the Γ pocket of HoPtBi is small, maintains cubic symmetry, and is located on the Brillouin zone center we can reasonably guess that a minimally distorted pocket would be convex, and cubic/octohedrally symmetric. Were this the case we expect a frequency ratio $f_{[100]}/f_{[110]} \approx 1.2$. A frequency ratio of 2.0 between the [100] and [110] orientations, as well as the non-$Cos(\Theta)$ like change in frequency, is inconsistent with these pictures.(fig. 5.4) This suggests that a static Fermi surface would have to have significant regions of concavity, which is unexpected for a small pocket near a high symmetry point. Alternatively if the Fermi surface is significantly distorted by field then we cannot reasonably expect a static image of the Fermi surface to account for field along different crystalline orientations. In this case the oscillations depict a Fermi surface that changes significantly upon rotation of field, potentially contracting significantly when field is oriented close to the [110] direction.

5.3 Transverse Magnetoresistance

The high-field ($> 10T$) magnetoresistance of HoPtBi exhibits quantum oscillations as described in section 5.2. However, despite the large amplitude of these oscillations we see no corresponding oscillation in magnetization (Ch. 3.3). This is not an unexpected turn of events, the origin for the resistance is by default a

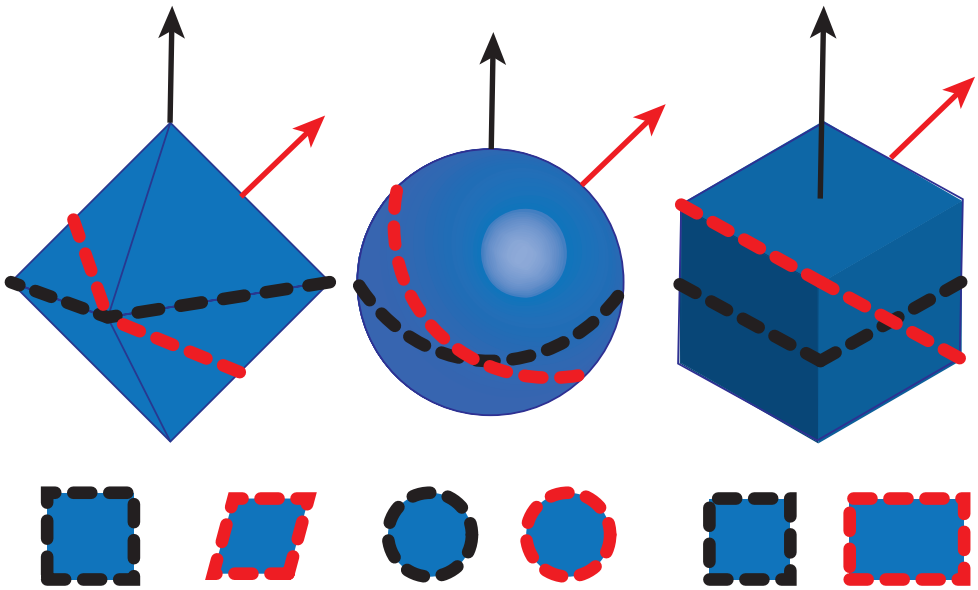

Figure 5.4: Non-concave solids obeying cubic symmetry which would be good initial candidates for a small cubic hole pocket. The cube and octohedron represent dual extremes of the same symmetry, with the spherical pocket being the isotropic case. The cube has the greatest difference in Fermi surface crossection with a $\frac{1+\sqrt{2}}{2} \approx 1.2$ ratio between the [100] and [110] projections, however this is much less than the roughly 2.0 ratio seen in quantum oscillation fitting.

property of the conduction electrons near the Fermi surface, while the origin of magnetism in this system depends on the localized f-electron states which are well removed from the Fermi surface. Therefore behavior in magnetism and conductivity are not necessarily linked. Nonetheless outside the specific case of quantum oscillations, in which conduction states must satisfy an additional Landau quantization rule, it is usually expected that anomalies or transitions in magnetoresistance would correspond to magnetic ordering of some type. In this section we report on a magnetoresistance signal which depends on angle of the applied magnetic field relative to the crystalline axes, with no associated transitions or ordering in magnetization.

Samples were measured in a Dynacool PPMS system. In order to control the relative orientation of the applied magnetic field samples were mounted on a uniaxial rotator. The magnetic field orientation is fixed within the sample chamber, however we can rotate the sample relative to this applied field. By viewing the system in the rest frame of the sample, the applied magnetic field is rotated around an arbitrary chosen axis, while the crystalline symmetries, and the applied current (which is introduced by the static electrical contacts) remain fixed. In cases relevant to this material we will discuss the 'transverse' case (in which $\vec{B} \perp \vec{E}$ for all chosen $\vec{B}$) and the longitudinal case (in which $\vec{B} \parallel \vec{E}$ at 90°) at 0° $\vec{B}$ is oriented perpendicular to the face of the sample bar, and in all cases $\vec{E}$ is along the sample bar.

We measured HoPtBi with field applied transverse to current.(figure 5.5) Current is applied along the [001] direction and field is rotated in the (001) plane, the transverse case. The (001) plane is C_4 symmetric, passing through the [100], and [110] high symmetry points. Different fields were applied and then the sample was

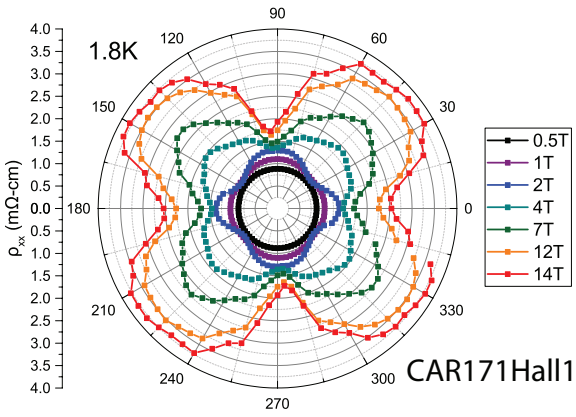

Figure 5.5: Resistance of HoPtBi under transverse resistance at base temperature. Sample values are symmetrized through 180° to remove the Hall component. The isotropy of the low-field signal gives way to C_4 symmetry under increasing field, which matches the projected symmetry of the [100] axis in a cubic system. Under higher field the nature of the MR orientation inverts at least once, such that the MR is enhanced along the [110] orientations, suggesting at least two fields at which the underlying cause for the MR changes character

rotated through 360°. The signal is symmetrized through 180° in order to eliminate any asymmetric component in field. Below $0.5T$ the sample is isotropic in MR for all measured temperatures. At low temperatures ($2K$) $1T$ applied field is enough to begin seeing four-fold symmetric MR signal, with a larger MR signal along the [100] directions of the crystal. At $2K$ an applied field of $4T$ causes this four-fold symmetric MR to flip character, and the greater MR direction becomes aligned along the [110] orientation of the crystal.

These angular cuts suggest an underlying mechanism that is sensitive to the crystalline symmetry of the sample. Besides the magnitude, which is of the order of 50-200%, the orientation dependence of this effect is characteristically dissimilar to the Lorentz-effect that contributes to MR in most metals. [24] [46] Other sources

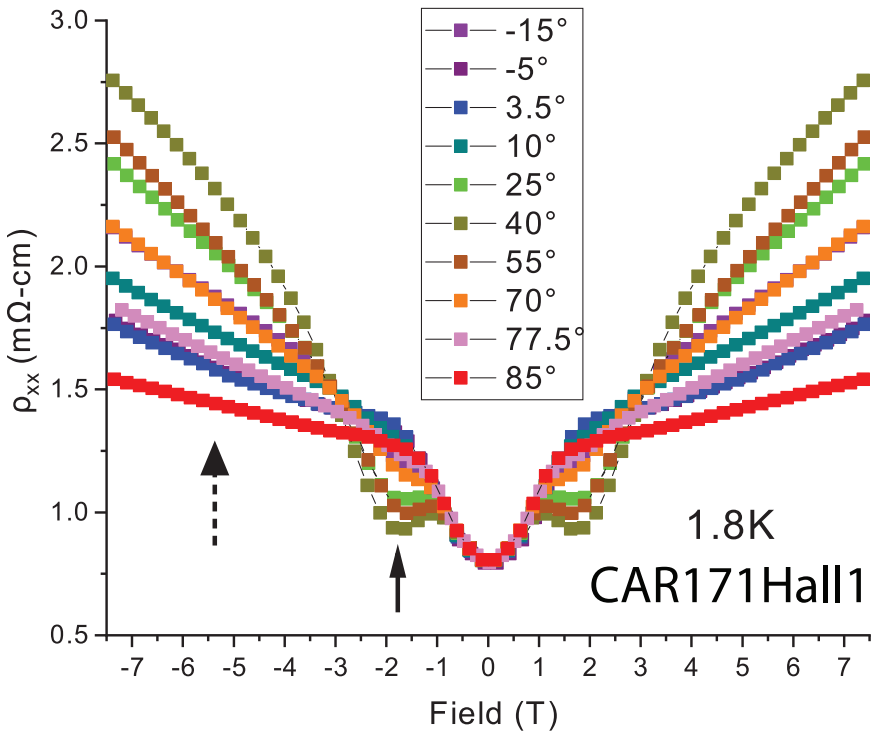

Figure 5.6: Symmetrized field sweep of resistivity as orientation is rotated from 0° through 90°. Regions of different AMR character are clearly visible. The solid arrow indicating AMR2 region where resistivity peaks along $0°, 90°$ and the dash arrow indicating AMR1 region, where resistance peaks along 45°.

of anisotropy that are dependent on just the relative orientation between magnetic field and electric field (such as the Planar Hall Effect, covered in section 1.1.5) are generally expected to follow two-fold symmetry at second order, whereas this effect is fourfold symmetric which matches the symmetry of the $F43m$ projected along its cubic [100] face.

The two regions of different AMR character are enumerated as AMR1, the high-field and low-T region with the largest anisotropy along [110], and AMR2 the lower-field higher temperature with anisotropy along [100]. Below approximately $0.5T$ there is a small region of quadratic magnetoresistive isotropy. In the high-field

AMR1 regime resistance is non-saturating in all directions, a character which carries over to high field measurements as visible in section 5.2. For all orientations high field appears almost linear, and unsaturating.

5.3.1 AMR Temperature Dependence

We extended our study of this anisotropy to higher temperatures in order to understand how this behavior evolves as the thermal energy scale increases. As the thermal distribution of states broadens we expect states further away from the Fermi Energy to contribute more to the behavior of the system. A naive accounting of this might expect that if the states furthest from the Fermi Energy do not contribute to anisotropy then the AMR will decrease in magnitude in temperature, but the field-dependent onset of anisotropy will not change with increased temperature. For reasons we will shortly cover this is not the behavior we observe.

We measured the AMR signal of HoPtBi under rotation at various fields (B=0.5-14T) and temperatures (T=2K,10K,50K). This measurement allowed us to establish the broader relationship between field application and temperature. Due to the large phase space that encompasses trying to measure across the three variables of field orientation, field magnitude and temperature only a few temperatures could be measured.(figure 5.7) Followup measurements more closely establish the relationship between field and temperature, but by avoiding measurements along all but two high symmetry directions. (figure 5.8)

Below $0.5T$ the sample is isotropic in MR for all measured temperatures, de-

spite a fairly large initial applied field. At low temperatures ($10K$) $1T$ applied field is enough to begin seeing four-fold symmetric MR signal, with a larger MR signal along the [100] directions of the crystal. At $2K$ an applied field of $4T$ causes this four-fold symmetric MR to flip character, and the greater MR direction becomes aligned along the [110] orientation of the crystal. Note that between $2K$ and $10K$ the field required to flip from [100] dominant to [110] dominant MR rises above $4T$ and appears closer to $7T$. Higher temperatures appear to push this transition to higher fields. At $50K$ even $14T$, the maximum applied field for the in-house Dynacool system, is insufficient to push the system into the AMR1 state and the [100] remains the predominant AMR direction for any sufficiently large applied field.

Next we measured the temperature-dependent MR of HoPtBi with $\vec{E} \parallel [001]$ and $\vec{B} \parallel [100], [110] \perp \vec{E}$ at various fields. the resistivity was measured in positive and negative fields and symmetrized in order to remove the contribution from the asymmetric Hall Effect. We found a strong MR difference for magnetic field applied along these two independent orientations that matches the overall character of anisotropy found in angular measurements. (figure 5.7, figure 5.8) As field is increased the overall MR of the sample increases, additionally the anisotropy between field applied along the [100] and the [110] directions greatly increases. The anisotropic difference between [100] and [110] directions also flips in sign as temperature increases, a result that broadly captures the difference that we see in the $4T$ data set in figure 5.7.

Closer inspection of figure 5.7 reveals that for sufficiently large fields ($>2T$) there are multiple regions where the largest AMR orientation will change. We

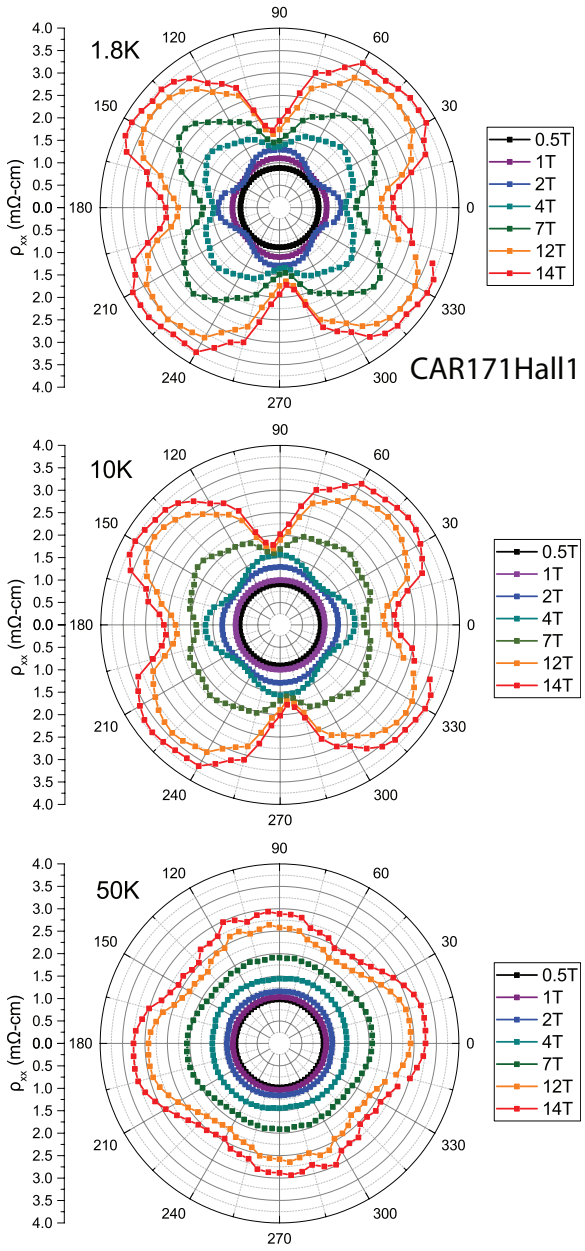

Figure 5.7: Transverse magnetoresistance measurements under rotation at higher temperatures ($10K$, $50K$). AMR1 with AMR enhanced along [110] is pushed to higher fields as temperatures increase, and is inaccessible even at $14T$ in the $50K$ data set. The intermediate field between AMR1 and AMR2 is visible at $4T$ in the $2K$ data set, and is pushed up to $7T$ in $10K$.

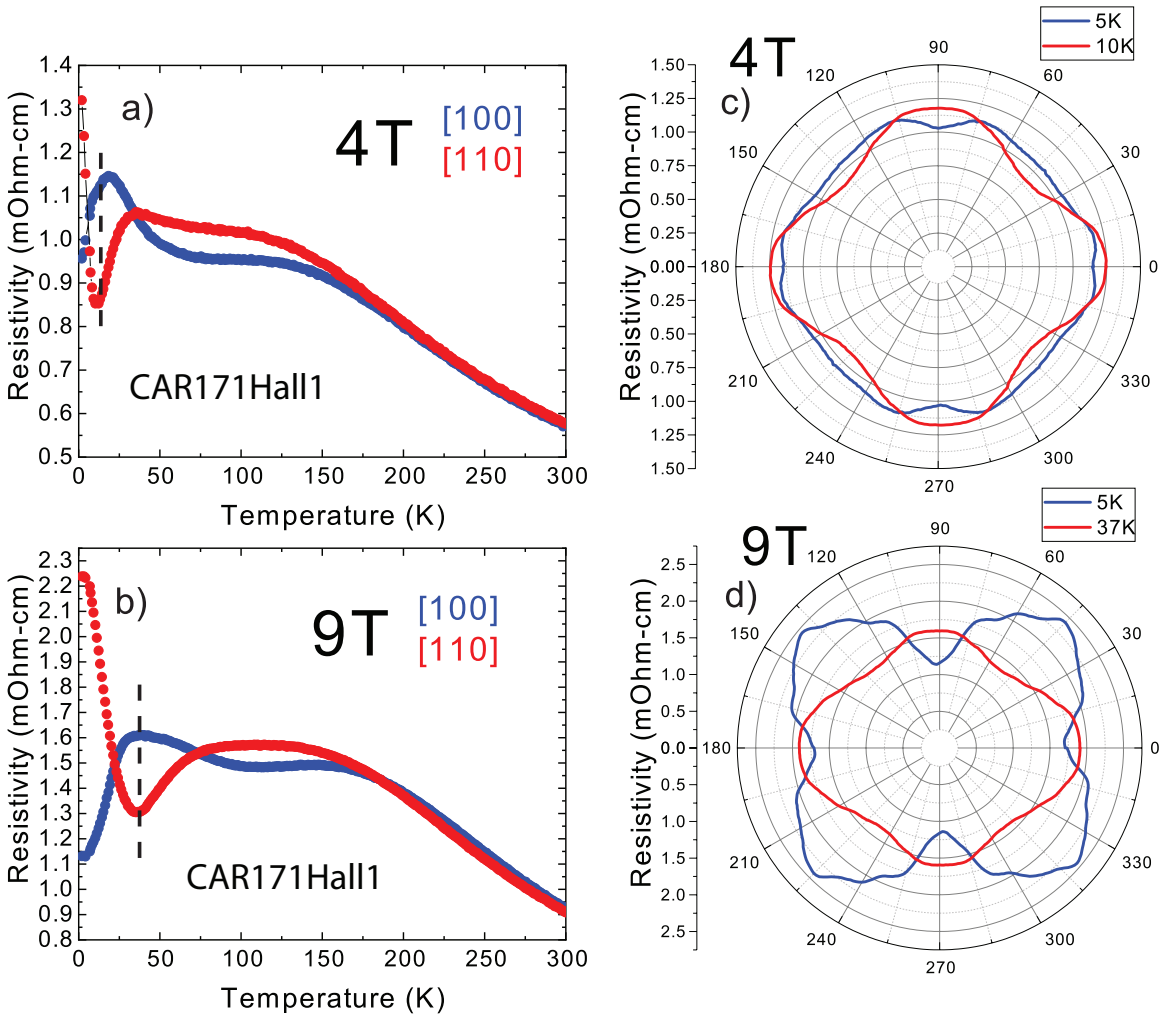

Figure 5.8: a) b) Several example datasets for HoPtBi Magnetoresistance with field oriented along one of two principal transverse axes corresponding to [100] or [110] directions. Data was symmetrized in positive and negative field to remove any anti-symmetric Hall contribution. A clear inversion in character is visible corresponding to a change in larger AMR contribution direction. Dashed line corresponds to chosen temperatures for follow up rotation measurements. c) d) Rotation measurements at fixed field and temperatures associated with maximum inversion of AMR character. Data sets are symmetrized through 180° in order to negate asymmetric contributions. a clear inversion in character is visible confirming temperature sweep measurements.

call these temperatures T_{AMR1} and T_{AMR2} with AMR1 representing the anisotropy present at base temperature (i.e. [110] predominant AMR). Higher fields stabilize both the AMR1 and AMR2 phases, however the AMR1 phase could only be pushed up to 22K at 14T. AMR2 can be stabilized to much higher temperatures, up to 76K confirmed at 9T. Careful inspection of both figure 5.8 can see a potential AMR3 state at low field and high temperature, in which the [110] AMR is once again predominant at higher temperatures, though at a much smaller magnitude. An inspection of T_{AMR3} was not attempted since the crossover to isotropy at room temperature occurs over a broad range, and the region of onset is subject to significant error.

We compared T_{AMR1} and T_{AMR2} with magnetization data (figure 5.9). Both temperatures track closely with fixed values of $M(B,T)$. This suggests that T_{AMR1} and T_{AMR2} correlate with fixed values for the internal field of the sample. This supports the picture that applied magnetic field does not directly influence the AMR of the samples, instead the internal moments are directly related to the AMR behavior, and the applied field is responsible for coercion of the paramagnetic moments.

This creates a complicated picture in which we have successive regimes with greater AMR amplitude that are stabilized by higher fields, but which are destabilized by increasing temperature. (figure 5.9) As briefly mentioned at the beginning of this section, if the band structure was static we might naively expect that the broadening of states near the Fermi level could increase or decrease the relative contribution of various AMR states, however it does not directly explain why increasing field can drive one contribution to overtake another. Furthermore there is no corresponding magnetically ordered phase, or clear resistive transition that

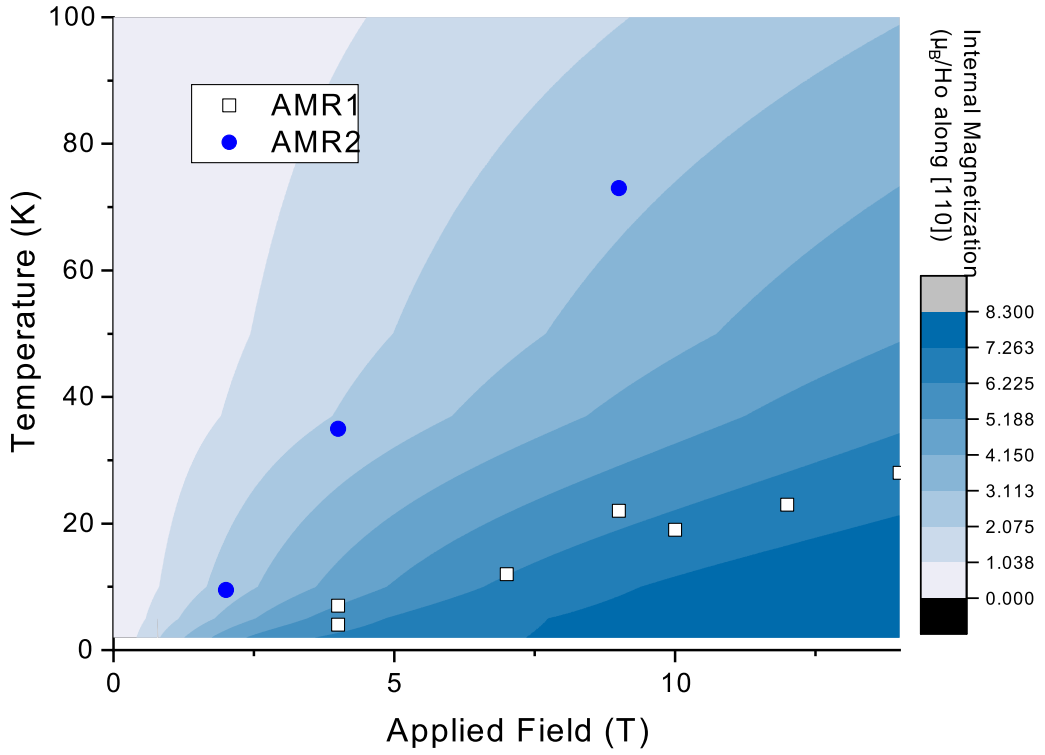

Figure 5.9: Map of transitions from [100] predominant AMR to [110] predominant AMR. Data was collected by temperature sweep in fixed-field and fixed-orientation samples, with samples symmetrized through positive and negative field. Contour map corresponds to Magnetization (ie internal field) collected by VSM measurement along the [110] orientation. Signature AMR transitions correspond roughly to fixed internal field.

accompanies the swap between the various AMR phases and the isotropic state at room temperature.

According to DFT calculations for other heavy-element Heuslers [12] the magnetic ordering of the f-electrons in the REPtBi material are the source of an effective interaction term with the band structure near the Fermi surface. Extending this model to HoPtBi as we increase temperature the paramagnetic moments become increasingly disordered, leading to a smaller internal field and a smaller interaction term. Meanwhile, increasing field will increase the paramagnetically derived internal field, stabilizing this effect. Data for the magnetic moment derived from VSM measurements has been integrated into figure 5.9 as a contour plot to indicate the magnetization of the Ho atoms within the sample, which directly corresponds to the internal moment of the system. It is apparent that the AMR1 and AMR2 correspond to fixed internal moments, suggesting a direct relationship between the onset of these AMR components and the moment alignment or internal field of the Ho atoms. As covered in chapter 1 anisotropic scattering does not appear to be a sufficient cause for anisotropic magnetoresistance of this magnitude (nor would it easily explain the change in AMR direction). Therefore it seems that the internal field's relationship with the Fermi surface is the likely cause for the AMR found in this system.

5.4 Conclusions

Since HoPtBi is a paramagnetic compound we cannot expect sources of magnetoresistance that depend on magnetic order, which rules out GMR (dependent on FM layered materials) [42] [43] [47] [48], CMR (ferrimagnetic half-metals) [49] , TMR (ferromagnetic-insulator layered structures) [50] and other ordering-dependent phenomena. Without these we do not have an explanation for the anisotropic magnetoresistance effects in this material, however given the other exceptional characteristics of this material we may be able to extrapolate a likely cause.

As discussed in sections 5.1, calculations indicate that the magnetic behavior of RPtBi strongly influences the Fermi surface of the material. When the magnetic moments are completely disordered only the $F43m$ symmetry remains. Without magnetic order there is no time reversal symmetry breaking to induce TRS Weyl points, however through application of moderates amount of field we expect Weyl points can be induced. In order to form Weyl pairs from a small Fermi surface significant Fermi surface distortion must occur, and in particular since the formation of these Weyl points is dependent on the orientation of the magnetic field relative to the crystal symmetry the distortion for a 4T field applied along (100) is significantly different than the distortion for 4T applied along (111) or (110).

If this understanding is correct then there is a new explanation for this AMR behavior. The Fermi surface is strongly dependent on the exchange interaction with the f-electrons, and the orientation of these f-electrons is quite malleable in the HoPtBi system with near-saturation readily achievable below 10T. Therefore

we expect that the behavior we describe here is a result of strong Fermi-surface distortions. In other words the magnetoresistance is derived from a purely electronic effect attributable to a field-distorted Fermi surface. This electronic effect, however, is the result of magnetic alignment in the paramagnetic material. The Ho f-electrons readily orient themselves to align with the applied magnetic field, which causes applied-field dependent distortions in the Fermi surface. This is quite distinct from many sources of MR that we often associate with ordered magnetic compounds, in which scattering is the predominant cause for large AMR contributions.

Chapter 6: Discussion and Conclusions

6.1 Conclusions

This dissertation studied the half-Heusler magnetic semiconductor HoPtBi. Structural and EDX measurements were undertaken to confirm structure and composition from samples grown in Bi-flux method. Neutron diffraction and susceptibility measurements found a conventionally ordered AFM compound below $1.25K$ and $2.5T$, and a Curie-Weiss paramagnet with antiferromagnetic correlations outside the ordered state. With moderate field the paramagnetism saturates and we find significant magnetic anisotropy in torque measurements, however with no associated indicators of magnetic ordering or hysteresis this anisotropy is attributed to effects from proximity to paramagnetic saturation.

We studied magnetoresistance in HoPtBi and found a number of rich behaviors. We investigated signatures of the chiral anomaly which are a key characteristic of Weyl semimetals. We also found a localized anomalous Hall angle deflection in transverse MR measurements, which is an intrinsic effect of compounds with Weyl crossings. In addition to characteristics indicative of Weyl behavior we found a novel anisotropic magnetoresistance response in moderate and high fields. This AMR response is unanticipated in unordered magnetic materials, and corresponds

rather readily to fixed internal moments of the system. Collectively HoPtBi is an exciting compound both in the investigation of magnetic Weyl semimetals and this potentially novel AMR state.

6.2 Further Work

This research has been a focused analysis of a single half-Heusler compound. As a result this research has engendered numerous open-ended questions about the source of the behaviors observed in this compound, as well as what other compounds might harbor similar behaviors

6.2.1 AMR in Similar Compounds

One of the striking anomalies in this compound is the presence of a significant magnetoresistive anisotropy without clear indicators of order. Similar compounds should be evaluated in order to discern whether this behavior is unique to HoPtBi, whether it extends to other magnetic half-Heuslers, magnetic Weyl semimetals or beyond.

GdPtBi is the first compound that should be evaluated for transverse AMR components. Numerous studies have already documented the chiral anomaly as well as the planar hall effect in GdPtBi, however we are not aware of any studies which show AMR that is independent of relative orientation between $\vec{B}$ and $\vec{E}$. It is worth noting that in GdPtBi that the Curie-Weiss paramagnetic regime extends up to significant fields, with saturation near $35T$. Since we find a significant AMR

component corresponds to near-polarization of the Ho $4f$ magnetic moments in HoPtBi, it is possible that GdPtBi would only produce a transverse AMR component at fields that are accessible only in specialized high-field equipped laboratories. It is also possible, given the model proposed for GdPtBi in which the Fermi surface distortion is mediated by internal moments, that a potential AMR state in GdPtBi would also have to reach a fixed internal field similar to HoPtBi. Since Gd^{+3} is a $J = 7/2$ state it is possible that GdPtBi would also have to be closer to its saturated PM state before inducing AMR.

The model for AMR proposed in HoPtBi depends on the idea that as a Weyl semimetal it must be close to a Liftshitz transition. This proximity to a Lifshitz transition, as well as the tuning of the Fermi surface through internal magnetic alignment, couple to produce a system in which the Fermi surface can be significantly distorted through application of field. AMR comes into the picture when the distortion has a different character for fields applied along different directions. This is already the proposed model for GdPtBi [12] in which application of field along different directions corresponds to the stabilization of different symmetry Weyl points. If this is the case then AMR might exist in any Weyl system where magnetism can significantly tune the FS. For this reason magnetic Weyl semimetals should be evaluated for AMR in high fields, to see if this behavior extends beyond just the half-Heusler system.

6.2.2 Fermi Surface Analysis

A significant section of this dissertation was devoted to the analysis of Shubnikov de Haas oscillations in HoPtBi. While we began this research expecting a fairly isotropic hole pocket, we found that the Fermi surface is either heavily distorted, giving rise to a significant anisotropy, or that the application of field in different orientations can have a large effect on the shape and size of the Fermi surface. While the Fermi surface can be indirectly probed through SdH analysis the functional dependence of the magnetoresistive response to field means that we cannot meaningfully distinguish between the case of a static, heavily anisotropic pocket and a pocket that is nearly isotropic in zero field but which is heavily distorted under field application.

ARPES measurements have already been conducted on GdPtBi. An ARPES measurement of HoPtBi in zero-field should be sufficient to determine if there is a large anisotropy in the Γ pocket. If insufficient anisotropy is detected then additional high-field confirmations of the Fermi surface will be required.

Chapter A: Fitting of low-frequency Quantum Oscillations

Quantum oscillations are a widespread tool for determining the size and shape of the Fermi surface [33]. In the 3D case and to first order oscillations follow the composite equation

$$\frac{m_c B^{1/2}}{(S'')^{1/2}_{extr}} R_T R_D R_S Cos(2\pi(\frac{F}{B} - \frac{1}{2}) + \gamma) \tag{A.1}$$

with the damping prefactors R_T, R_S, and R_D. These prefactors take the following form

$$R_D = exp(-2\pi^2 k_B T_D/\hbar\omega_c) \tag{A.2}$$

$$R_S = Cos(\frac{\pi}{2} g m_c/m_0) \tag{A.3}$$

$$R_T = \frac{2\pi^2 k_B T/\hbar\omega_c}{Sinh(2\pi^2 k_B T/\hbar\omega_c)} \tag{A.4}$$

with $\omega_c = qB/m_c c$. Note that all of these prefactors are monotonically increasing in field, which will be a crucial justification for our choice of envelope function.

Shubnikov de Haas calculations are often reserved for metals which have large Fermi surfaces and high carrier counts. As a result most SdH analysis is focused on materials with accessible fields and with high oscillation frequencies. HoPtBi presents a difficult situation with an extremely small Fermi surface and low oscillation frequencies, with oscillations in the 35-70T range, we need to be careful about employing the conventional techniques involved in analyzing Quantum Oscillation data.

For high-oscillation frequency data it is often the standard to perform an FFT on either the initial data, or a derivative thereof, in order to extract the oscillation frequency component which corresponds to the Fermi pocket extrema area. This is successful in most cases because high oscillation frequency and a wide FFT window relative to the frequency makes extraction of the frequency component reliable. However this is not, in general, a foolproof method for extracting the frequency component of Quantum Oscillation data.

In order to understand the limitations of FFT it is necessary to understand how exactly an FFT is calculated. The FFT is essentially a change in basis for a periodic function to a series of harmonics the exact details of which can be covered in a number of mathematic and computational textbooks. In the event that the signal repeats exactly in a given window, all frequencies will be a multiple of that window. In practice signals never match the measured window exactly. There are numerous methods for minimizing errors introduced by this mismatch, including the use of

windowing functions which minimize distortions in the signal from mismatches at the edge of a sampled data set, however these tools are intended to error-correct signals that are periodic, which our signal is not.

These techniques are intended to minimize small effects in the edge cases of well behaved data sets, i.e. finite, repeating signals with a well defined frequency that is not drastically mismatched to the window being analyzed. In the case of SdH analysis several of these constraints are fundamentally not well satisfied, and FFT is useful only in so much as these issues are avoided.

For example consider equation A.1. We can decompose this into an oscillatory component:

$$Cos(2\pi(\frac{F}{B} - \frac{1}{2})\gamma) \tag{A.5}$$

and a non-repeating envelope function:

$$\frac{m_c B^{1/2}}{(S'')(1/2)_{extr}} R_T R_D R_S \tag{A.6}$$

The oscillatory component is finite and in the case of a single or multiple frequencies related by a rational multiplicative, repeating. If that were the totality of the signal it would not present an issue for FFT even in the case of an irrational ratio between components, provided the frequency window was sufficiently larger than the frequencies being analyzed.

The envelope function however represents an obvious problem. Since the envelope function is non-periodic (and indeed, exponentially increasing in field) it cannot

be reduced to the harmonic basis. Of course, this does not stop us from trying, and it can be insightful to attempt to do so. In the case of high frequencies such that the signal does not change much over a single wavelength the FFT will successfully interpret the oscillatory component.

In most cases non-periodic functions will contribute a false spectral component mostly to low-lying frequencies, however this is not guaranteed. In conventional SdH analysis on materials with large Fermi surfaces the spurious signal from the envelope function will be dwarfed by the well-localized weight from the high-frequency oscillation component. In the event of an extremely low-frequency signal, such as discussed in section 5.5 of this dissertation, this false contribution cannot be ignored.

While a non-bounded windowing function presents an analytic problem for the issue of Fourier Analysis, there are also separate, practical issues that plague FFTs on low-frequency data. FFT is by necessity evaluated upon a fixed window of data, and ultimately it can only decompose the signal into a series of finite frequencies e^{ingx} where $n \in \mathcal{N}$, the natural numbers and g is some value corresponding to the width of the evaluated FFT window. For high-frequency data, ie very large values of n the difference between two adjacent channels is small, so even if the evaluated frequency is not an exact multiple of g the adjacent frequencies are likely to collect the spectral weight of that function. In the case of low-frequency data that mismatches with the window the nearest frequencies do not approximate the actual function very well, and spectral weight can be dispersed into many channels obscuring results. An example of several of these problems is given in (figure A.2)

There are other issues with FFTs and there are many techniques beyond the

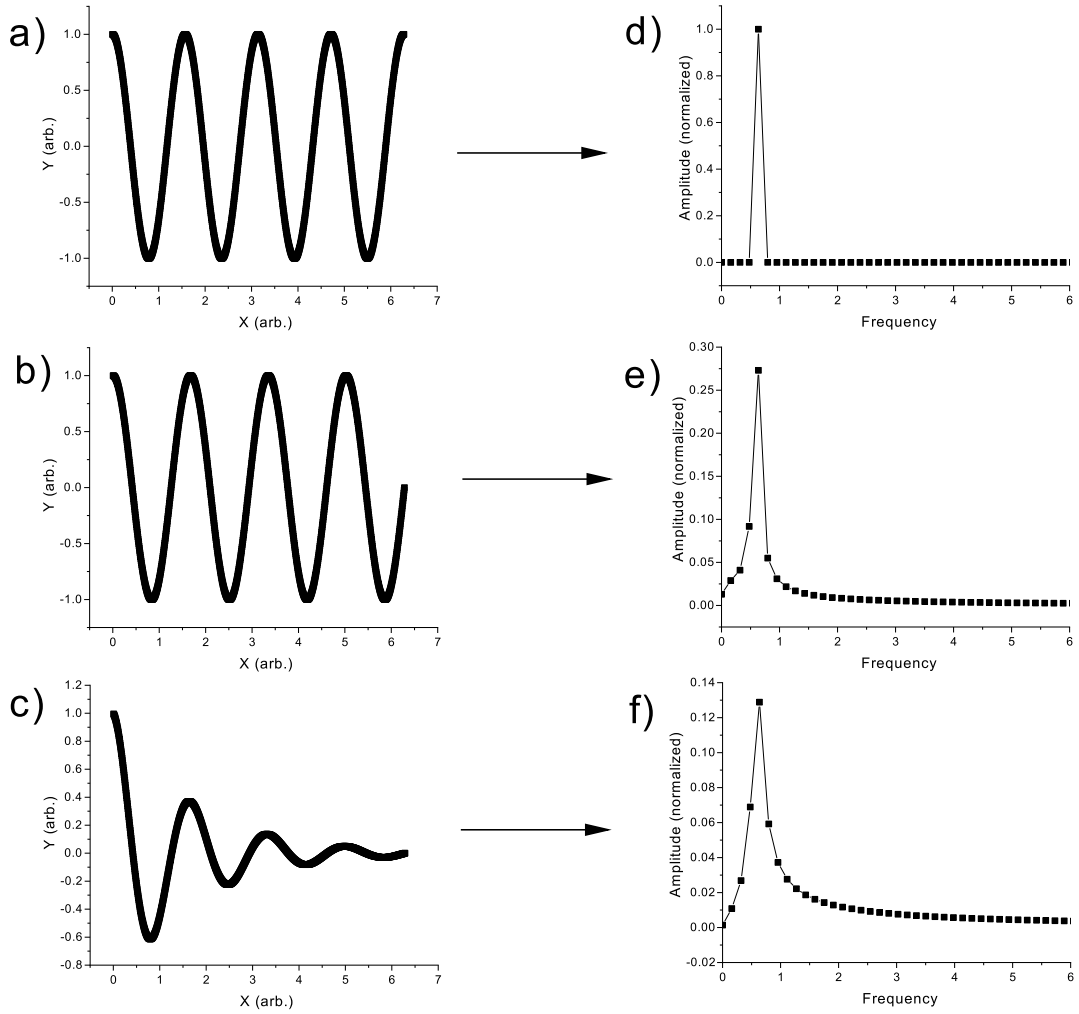

Figure A.1: FFTs evaluated on exact low-frequency data sets (within computational resolution). a)-c) are the initial data sets comprised of 1000 data points each with singular well-defined frequencies while d)-f) are the normalized FFT amplitudes. (take special note of the axes, which are expanded so peak broadening is more easily observed) a),d) a single frequency which exactly matches the sampled window resolves into a single FFT bin. b),e) a single frequency which is mismatched to the sampling window by a quarter wavelength creates a broadened peak in FFT spectra. c),e) a single frequency with an exponentially decaying envelope function resolves into a broadened peak with a long spectral weight tail.

scope of this section for ameliorating these problems. Fortunately FFT is not the only means to discern the frequency component of a signal. Fitting functions are well equipped to handle issues of low frequency and non-trivial envelope signal analysis, provided the fitting function is well justified.

In the case of HoPtBi magnetoresistance data was collected as a function of field $\vec{H}$ at the NHMFL. Data was transformed into a $\frac{1}{H}$ basis and collected into equally spaced bins for purposes of calculation. Individually collected data points are subject to some random noise from measurement apparatus. An error with standard deviation of $\sigma \approx 3\%$ was assumed based on documentation from the lock in amplifier. Data points were roughly evenly spaced in H so with transformation into the $\frac{1}{H}$ basis high field bins collected a greater number of overall data points, and total mean standard deviation σ_{bin} is appropriately smaller for high field measurements.

Once data had been collected in the $1/H$ basis the second derivative was taken twice. This was done in order to emphasize the high-amplitude oscillation components while minimizing the near-linear background. Previous attempts had been made to do a background subtraction on the $\rho(H)$ data, however it was found for low-frequency data an attempt to add a linear or quadratic fit to data with large, incomplete oscillations at high field would have an oversized influence on the fit, leading to anomalous fitting values.

Bumps: Curve Fitting and Uncertainty Analysis software package was used to evaluate the resulting array of evenly spaced data points and associated uncertainties. Bumps is a Markov chain Monte Carlo analytic package with numerous uses. Bumps was designed, and is used in this dissertation, in order to evaluate curve

fitting to a set of data points with associated uncertainty. Bumps also provides useful diagnostic information about the Monte Carlo methods which can be used to evaluate whether a particular fit effectively converges and if there is significant correlation between variables in a chosen fit. Both of these properties are very useful for determining if a fitting equation is underconstrained, which is vital for making an informed decision between single and multiple frequencies in SdH analysis.

Bumps requires choosing a fitting function as well as a window for all parameters. DREAM then blankets the parameter space with randomly chosen variables, each guess is then iteratively evolved to minimize distance from the provided array of data points. Each initial condition evolves into a deterministic local minimum according to the constraints provided by the fitting function. If the fitting function and parameter windows are well chosen then the result should be a single minimum to which each initial set of parameters eventually converges, and further evolution should be highly constrained i.e. a single model should not 'wander' away from a fitting value.

The fitting function chosen for this modeling was:

$$f(x) = A_i e^{-k_i \cdot x} Cos(m_i \cdot x + \phi_i) + \frac{b}{x^3} \tag{A.7}$$

with summation implied for fittings involving multiple frequencies. b/x^3 is the background term corresponding to the linear MR. The exponential term was chosen as a phenomenological choice for the envelope function discussed in chapter 5. The analytical form of this envelope is more complicated however the exponential term

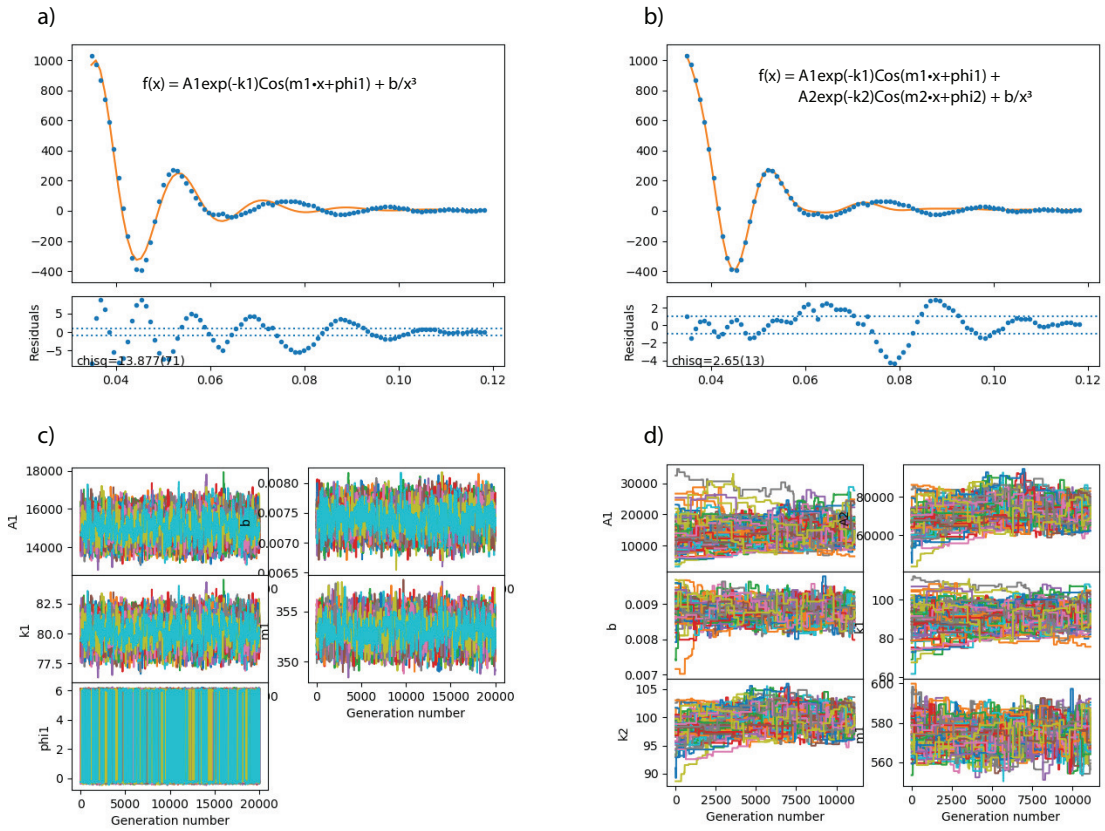

Figure A.2: Two comparative sets of diagnostic data for Bumps fitting software. a) data points, fitting, and variance for a single-frequency fit. b) data points, fitting, and variance for a two-frequency fit. c) Trace of fitting parameter evolution after a large number of steps. Each color represents a different initial condition as it evolves. Variables have all converged on a tight range of values and are highly localized, indicating convergence. d) Trace of fitting parameters for the two-frequency fits after a large number of steps, parameters have a wide range and liable to wander, indicating the fit is not well-converged and is under-constrained.

was the predominant term by at least an order of magnitude. Since the goal of this fitting was to determine the oscillatory frequency and the relationship between potential pockets was uncertain it was determined that an attempt to better characterize the envelope function carried significant uncertainty and minimal potential benefit. Attempts at fitting a more complicated envelope did not significantly affect the frequency value.

An example of data set analysis is presented in fig.A.2. This data set was chosen to reflect a particular anomaly that is apparent in certain orientations near the [110] direction in which the oscillation frequency appears to change slightly between low and high fields. Initially it was believed this may be due to a beating effect of SdH from two bands. Attempts were made to resolve two bands through bumps analysis assuming two independent bands with different frequencies and prefactors. Bumps software package was used to evaluate the convergence and interdependence of variables. It was determined that the two-frequency models did not significantly improve the fitting and introduced significant correlation between fitting parameters, indicating an under-constrained model. This does not rule out the potential for a second frequency, however if it exists it cannot be resolved from this method.

The results of these fits are presented in figure 5.3 as a supplement to FFT analysis. Results were found to correspond closely to FFT results, but allowed a better resolution of frequencies.

Chapter B: Growths

Research always involves many attempts before a single novel success is found. It is easy to publish and document those shining successes and leave the other roads traveled to get there unlit. This appendix is meant to document the numerous growths attempted during my graduate student career in order to help highlight failures and other possible routes forward in pursuit of new results.

Take note: The 'Product' column is necessarily ambiguous. While I attempted to document the products of a growth with some specificity, it isn't entirely possible to describe in depth each growth output here. Note that some growths produced a crystal that wasn't intended (e.g. numerous YPtBi doping attempts produced pure YPtBi) and 'failed' growths may be successful with further tweaks.

Goal Compound	Component Ratio	Growth Method	Product
HoPtBi	1:1:20	Bi flux	SC
HoPtBi	1:1:10	Bi flux	poly
CeSbTe	1:1:1	I2 Vapor Transport	failed
TbPdBi	1:1:10	Bi flux	SC
YPtBi	1:1:20	Bi flux	SC
HoPdBi	1:1:10	Bi flux	SC
ErPtBi	1:1:20	Bi flux	SC
Ce3Pt4Bi3	1:1:20	Bi flux	SC
PrPtBi	1:1:20	Pb flux	SC
LuPtBi	1:1:20	Bi flux	SC
LuPt0.85Au0.15Bi	1:0.85:0.15:20	Bi flux	SC
YPt0.85Bi	1:0.85:20	Bi flux	SC
HoPtBi	1:1:1:20	Pb flux	Domain-twin SC
YPtBi	1:1:1:20	Pb flux	SC
YPt0.85Au0.15	1:0.85:0.15:20	Bi flux	SC
CePtBi	1:1:1:20	Pb flux	SC

Goal Compound	Component Ratio	Growth Method	Product
PrPtBi	1:1:1:20	Pb flux	SC
LaPtBi	1:1:20	Pb flux	La3Pt4Bi3 SC
PrPtBi	1:1:20	Bi flux	Pr3Pt4Bi3 SC
CePtBi	1:1:20	Bi flux	Ce3Pt4Bi3 SC
ErPtBi	1:1:20	Bi flux	SC
TmPtBi	1:1:20	Bi flux	SC
YPt0.5Ni0.5Bi	1:0.5:0.5:20	Bi flux	failed
YPtBi0.85Sb0.15	1:1:(0.85:0.15)*20	Mixed flux	YPtBi SC
YPtBi0.85Sn0.15	1:1:(0.85:0.15)*20	Mixed flux	YPtBi SC
YPtBi0.85Te0.15	1:1:(0.85:0.15)*20	Mixed flux	YPtBi SC
YPtBi0.85Pb0.15	1:1:(0.85:0.15)*20	Mixed flux	YPtBi SC
CeRu4Sn6	1:4:6	Arc Melt	failed
Y0.85Zr0.15PtBi	0.85:0.15:1:20	Bi flux	YPtBi SC
Y0.85Hf0.15PtBi	0.85:0.15:1:20	Bi flux	YPtBi SC
YPt0.85Ag0.15Bi	1:0.85:0.15:20	Bi flux	YPtBi SC
YPt0.90Ag0.10Bi	1:0.90:0.10:20	Bi flux	YPtBi SC

Goal Compound	Component Ratio	Growth Method	Product
YPt0.95Ag0.05Bi	1:0.95:0.05:20	Bi flux	YPtBi SC
CeRu4Sn6	1:4:6	Solid State	failed
CeRu4Sn6	1:4:6:10	Pb flux	poly
YPt0.5Au0.5Bi	1:0.5:0.5:20	Bi flux	failed
YPt0.25Au0.75Bi	1:0.25:0.75:20	Bi flux	failed
YAuBi	1:1:20	Bi flux	failed
YPt0.99Au0.01Bi	1:0.99:0.01:20	Bi flux	YPtBi SC
YPt0.98Au0.02Bi	1:0.98:0.02:20	Bi flux	YPtBi SC
YPt0.97Au0.03Bi	1:0.97:0.03:20	Bi flux	YPtBi SC
Ru2Sn3	2:3	Arc melt	failed
YPt0.99Ir0.01Bi	1:0.99:0.01:20	Bi flux	YPtBi SC
YPt0.98Ir0.02Bi	1:0.98:0.02:20	Bi flux	YPtBi SC
YPt0.95Ir0.05Bi	1:0.95:0.05:20	Bi flux	YPtBi SC
YPt0.90Ir0.10Bi	1:0.90:0.10:20	Bi flux	YPtBi SC
YPt0.85Ir0.15Bi	1:0.85:0.15:20	Bi flux	YPtBi SC
YPt0.90Au0.10Bi	1:0.90:0.10:20	Bi flux	YPtBi SC

Goal Compound	Component Ratio	Growth Method	Product
YPt0.95Au0.05Bi	1:0.95:0.05:20	Bi flux	YPtBi SC
MnP	1:1:20	Sn flux	failed
CoP	1:1:20	Sn flux	SC
RuP	1:1:20	Sn flux	SC
YPtSb	1:1:1:20	Bi flux	SC
YPtSb	1:1:99	Sb flux	PtSb2 SC
Y0.8Ti0.2PtBi	0.8:0.2:1:20	Bi flux	YPtBi SC
YbIr2P2	1:2:2:60	Pb flux	failed
IrP	1:1	Solid State	poly
RuP	1:1	Solid State	poly
YbRu2P2	1:2:2:45	In flux	SC
RuAs	1:1:25	Sn flux	SC
RuP	1:1:25	Sn flux	SC
YbRu2As2	1:2:2	Solid State	poly
YbRuBi	1:1:18	Bi flux	failed
CeRu2As2	1:2:2	Solid State	poly

Goal Compound	Component Ratio	Growth Method	Product
YbRu2As2	1:2:2	Solid State	poly
YbRu2P2	1:2:2:45	Sn flux	failed
YbRu2P2	4:7:7:82	Sn flux	failed
YbRu2P2	1:2:2:15	Sn flux	SC
LaRu2P2	2:5:5:95	In flux	SC
TaAs	1:1:19	In flux	SC
TaAs	1:1	Solid State	binary
YRuSn3	4:3:93	Sn flux	SC
YbRu2P2	3:2:4:51	In flux	SC
YbRu2P2	3:2:4:51	Sn flux	SC
LaRu2P2	1:2:2:40	Sn flux	SC
Yb0.65La0.35Ru2P2	0.65:0.35:2:2	Sn flux	failed
Ca0.88La0.12FeAs1.8Sb0.2	0.8:0.12:1.8:0.2	Solid State	poly
Ca0.3La0.7Ru2P2	0.3:0.7:2:2:60	In flux	failed
Ca0.5La0.5Ru2P2	0.5:0.5:2:2:60	In flux	failed
Ca0.7La0.3Ru2P2	0.7:0.3:2:2:60	In flux	failed

Goal Compound	Component Ratio	Growth Method	Product
CaRu2P2	1:2:2:60	In flux	failed
Yb0.3La0.7Ru2P2	0.3:0.7:2:2:60	In flux	failed
Yb0.5La0.5Ru2P2	0.5:0.5:2:2:60	In flux	failed
Yb0.7La0.3Ru2P2	0.7:0.3:2:2:60	In flux	failed
YbRu2P2	1:2:2:60	In flux	SC
Ca0.88La0.12FeAs1.8Sb0.2	0.88:0.12:1:1.8:0.2	Solid State	poly
YFe2Ge2	1:2:2	Arc Melt	failed
Y0.05La0.95Ru2P2	0.05:0.95:2:2:40	In flux	failed
Y0.1La0.9Ru2P2	0.1:0.9:2:2:40	In flux	failed
Y0.2La0.8Ru2P2	0.2:0.8:2:2:40	In flux	failed
Pr0.025Ca0.975Fe2As2	0.025:0.975:2:2:10	Sn flux	SC
YRu2P2	1:2:2:40	Sn flux	failed
YRu2P2	1:2:2:80	Sn flux	failed
LaRu2P2	1:2:2:40	Sn flux	SC
LaRu2P2	1:2:2:80	Sn flux	SC
Pr0.05Ca0.95Fe2As2	0.05:0.95:2:2:10	Sn flux	SC

Goal Compound	Component Ratio	Growth Method	Product
CeRhIn5	1:1:20	In flux	SC
CeRh0.4Co0.6In5	1:0.4:0.6:20	In flux	SC
CeRh0.5Co0.5In5	1:0.4:0.6:20	In flux	SC
La0.15Ca0.85Fe2As2	0.15:0.85:2:2:20	Sn flux	SC
YFeGa5	1:1:30	Ga flux	SC
ScFeGa5	1:1:30	Ga flux	SC
CaFe2As2	1:2:2:20	Sn flux	SC
CaFe2As2	1:2:2:20	In flux	SC

Bibliography

[1] H. Weyl, *PNAS*, 15 (4), 323 (1929)

[2] O. Vafek, A. Vishwanath, *Annu. Rev. Condense. Matter Phys.*, 5, 83, (2014).

[3] D. Vanderbilt, *Berry Phases in Electronic Structure Theory* (Cambridge University Press, Cambrdige UK, 2018) Ch.5.

[4] C. Kittel, *Introduction to Solid State Physics* (John Wiley Sons, Inc., USA, 2005) Chap.17.

[5] N.P. Armitage, E.J. Mele, and Ashvin Vishwanath, *Rev. Mod. Phys.*, 90, 015001 (2018).

[6] N. Nagaosa *et al.*, *Rev. Mod. Phys.*, 82, 1539 (2010).

[7] S.A. Yang, *SPIN* 06 (02), 1640003 (2016).

[8] Y.S. Eo *et al.*, *P. Natl. Acad. Sci. USA*, 116 (26), 12638 (2019).

[9] P. Syers *et al.*, *Phys. Rev. Lett.*, 114 (9), 096601 (2015).

[10] B.Q. Lv *et al.*, *Phys. Rev. X*, 5 (3), 031013 (2015).

[11] S.Y. Xu *et al.*, *Science*, 349 (6248), 613 (2015).

[12] C. Sekhar *et al.*, *P Natl Acad Sci USA* 115 (37), 9140 (2018).

[13] Y. Nakajima *et al.*, *Sci. Adv.*, 1 (5), e1500242 (2015)

[14] P. Schlottmann, *AIP Advances* 6, 055803 (2016).

[15] M. Imran, and S. Hershfield, *Phys. Rev. B.*, 98 (20), 205139 (2018).

[16] A.A. Burkov, *Phys. Rev. Lett.*, 113, 187202 (2014).

[17] Y. Zhang, and B. Yan, *Phys. Rev. B.*, 97 (4), 041101 (2018).

[18] L.P. Bouckaert, R. Smoluchowsiki, and E. Wigner, *Phys. Rev.* 50 1, 58 (1936).

[19] H.B. Nielsen, M. Ninomiya, *Phys. Lett.*, 130B (6), 389 (1983).

[20] C.L. Zhang *et al.*, *Nat. Commun.*, 7, 10735 (2016).

[21] M. Hirschberger *et al.*, *Nat. Mater.*, 15, 1161 (2016).

[22] J. Xiong *et al.*, *Science*, 350 (6259), 413 (2015).

[23] Y. Li *et al.*, *Front. Phys.* 12 (3), 127205 (2017).

[24] A.B. Pippard, *Magnetoresistance in Metals* (Cambridge University Press, Cambridge, UK, 1989), Chap.1.

[25] N. Kumar *et al.*, *Phys. Rev. B*, 98, 041103 (2018).

[26] S. Xu *et al.*, *Nat. Phys.* 11, 748 (2015).

[27] B.Q. Lv *et al.*, *Phys. Rev. Lett.*, 115, 217601 (2015).

[28] E. Mun, S.L. Bud'ko, and P.C. Canfield, *Phys. Rev. B* 93, 115134 (2016).

[29] C.L. Zhang *et al.*, *Phys. Rev. B*, 95 (8), 085202 (2017).

[30] N.P. Butch *et al.*, *Phys. Rev. B.*, 84, 220504 (2011).

[31] H. Kim *et al.*, *Science Advances* 4 (4), eaao4513 (2016).

[32] R.L. Parker, *Solid State Physics*, 25, 151, (1970).

[33] A.B. Pippard, *Magnetoresistance in Metals* (Cambridge University Press, Cambridge, UK, 1989), Chap.4.

[34] N.W. Ashcroft, andN.D. Mermin, *Solid State Physics* (Thomson Learning Inc., US, 1976), Chap 14.

[35] J. Lynn *et al.*, *J. Res. Nat. Bur. Stand.*, 117, 61 (2012).

[36] P.C. Canfield *et al.*, *Journal of Applied Physics*, 70, 5800 (1991).

[37] E. Mun, S.L. Bud'ko, and P.C. Canfield, *Phys. Rev. B* 93, 115134 (2016).

[38] N.W. Ashcroft, and N.D. Mermin, *Solid State Physics* (Thomson Learning Inc., US, 1976), Chap 31.

[39] W. Thomson, *Proc. R. Soc. Lond.* 8, (1857).

[40] T.R. McGuire, and R.I. Potter, *IEEE T MAGN* 11 (4), 1018 (1975).

[41] The Nobel Prize in Physics 2007.
https://www.nobelprize.org/prizes/physics/2007/summary/

[42] M.N. Baibich *et al.*, *Phys. Rev. Lett.*, 61, 2472 (1988).

[43] G. Binasch *et al.*, *Phys. Rev. B*, 39, 4828 (1989).

[44] S.A. Solin *et al.*, *Science*, 289 (5484), 1530 (2000).

[45] F. Yang *et al.*, *Phys. Rev. B.*, 61 (10), 6631 (2001).

[46] Y. Shapira, R.L. Kautz, *Phys. Rev. B.*, 10 (11), 7481 (1974).

[47] J. Pierre, I. Karla, *Magn. Magn. Mater.*, 217, 74 (2000).

[48] F. Casper, C. Felser, *Solid State Commun.*, 148, 175 (2008).

[49] A.P. Ramirez, *J. Phys.: Condens. Matter*, 9 (39), 8171 (1997).

[50] T. Miyazaki, and N. Tezuka, *J. Magn.*, 151 (3), 403 (1995).